POLITECNICO DI MILANO

Scuola di Ingegneria Industriale e dell'Informazione
Corso di Laurea Magistrale in Ingegneria Biomedica

TESI DI LAUREA MAGISTRALE

TRANSCATHETER AORTIC VALVE REPLACEMENT: MEASURING PHYSIOLOGICAL COMPLIANCE AND VESSEL GEOMETRY USING A VALVULOPLASTY BALLOON CATHETER

Relatore: Elena De Momi

Correlatore: Helge Wurdemann

Tesi di laurea di:

Sara Di Giuseppe matr. 852574

Anno accademico 2016/2017

Ai miei nonni,

Acknowledgements

Desidero innanzitutto ringraziare la mia relatrice, professoressa De Momi, per avermi dato l'opportunità di svolgere il mio progetto di tesi a Londra, per la disponibilità e i validi consigli a sostegno di questo lavoro.

A special thanks goes to my foreign supervisor, Dr. Helge Wurdemann, for having me at the Soft Haptics Lab at UCL with extreme kindness and availability. Furthermore, I am deeply grateful to Andrea Palombi, for guiding me throughout this project with outstanding expertise and sympathy.

Un grazie speciale va alle mie amiche, Giuly, Cotta, Bramba, Annette&MaryV. Grazie per aver condiviso con me gioie, sacrifici e successi. Vorrei ringraziare anche Vale, Fede e Fra, per i 3 anni trascorsi a Cesena, per i momenti passati insieme tra ansie (tante) e soddisfazioni. Come non menzionare anche Enri, Andre e Augusto, che mi hanno sopportato in questi ultimi 2 anni qui a Milano, rendendo il tutto più divertente (si ragazzi, lo ammetto).

Vorrei infine ringraziare la mia famiglia, per avermi ascoltato e spronato ad andare avanti nonostante le difficoltà. Last but not least, un grazie speciale a Canna, per essermi stato vicino negli ultimi 6 anni.

Infine, dedico questa tesi ai miei nonni. A Rosina, che ho ancora la fortuna di avere al mio fianco, e a quelli che non ci sono più, il nonno Benito, la nonna Candy e il nonno Peppo.

Abstract

Aortic stenosis (AS) is a serious valvular heart disease, which affects 2% of people who are over 65 years of age. It is characterised by a narrowing of the aortic valve opening, usually induced by age-related progressive calcifications and, if untreated, it is associated with a 50% rate of death within two years after the appearance of symptoms. Open-heart aortic valve replacement (AVR) is the traditional surgical procedure used to treat AS. However, at least 30% of the patients with severe AS cannot undergo surgery, because of multiple coexisting conditions.

Transcatheter Aortic Valve Replacement (TAVR) has therefore been introduced in 2002 as a minimally invasive alternative to AVR. The positive clinical outcomes have allowed this technique to rapidly develop over the past fifteen years. Nevertheless, TAVR is still affected by some major intra-operative complications, such as neurological events and aortic regurgitation. The main causes of regurgitation are malpositioning or undersizing of the prosthetic device, an elliptic shape of the aortic annulus or an irregular distribution of calcium depositions within the surrounding tissue. In such cases, the expansion of the prosthetic valve might be incomplete or uneven, leading to deformation of the stent (paravalvular leakage) or malcoaptation of the leaflet edges (transvalvular leakage). Therefore, it is crucial for the surgeon to have accurate information about the cross-sectional geometry and the mechanical properties of the aortic annulus, to choose the right prosthesis to be implanted and optimise the results of the procedure.

According to the current recommendations, the size of the annulus is measured, prior to TAVR, either with 2D transesophageal echocardiography (TEE) or transthoracic echocardiography (TTE). However, it has been demonstrated that bidimensional echocardiographic images are not the best option to assess the complex 3D geometry and the elliptic shape of the aortic annulus.

To date, as far as compliance assessment is concerned, direct measurements of vascular stiffness can be performed in vitro or in vivo. While the former has some significant limitations, the latter overcome such weaknesses using imaging techniques.

The aim of this work is to propose a method to infer both mechanical and geometrical properties of rigid and compliant phantom vessels. The herein described approach is based on simultaneously volume and pressure measurements of liquid inside the robotic soft balloon, gathering knowledge on the interaction between rigid/compliant anatomies and valvuloplasty balloon in terms of pressure-volume (P-V) curves.

The first step of this work involves the creation of a numerical model of the BAV balloon catheter from polariscopic images of the real device. The sketch has then been imported into Abaqus/Standard to generate a hexahedral element mesh and finally transferred to MSC. Marc® for further finite element analyses. A variable thickness, attributable to manufacturing techniques, has been considered while approximations have been made to make the part symmetric. The inflatable balloon has been discretised into hexahedral 8-noded elements and it has been approximated with a linear elastic isotropic material. Boundary conditions have been applied to the model and the balloon has been inflated by applying a constantly increasing pressure to the cavity. In order to recreate an initial tri-folded configuration, an additional preliminary simulation has been included as well.

The second step concerns numerical simulations, performed on MSC. Marc® by inflating the previously described numerical model of the balloon catheter inside rigid vessels. Moreover, numerical models of compliant vessels have been created as well, in order to compute their distensibility.

The procedure followed to create rapid-prototyping compliant annuli consists in several steps, which can be summarised as follows: (i) estimation of physiological compliance from literature, (ii) tensile tests of silicone samples, (iii) MSC Marc simulations and (iv) the design and printing of moulds to fabricate phantom vessels. DragonSkin30 has been chosen as compliant annuli manufacturing material and a second order Ogden form has been chosen to approximate its behaviour; associated parameters have been extrapolated by MSC. Marc® from the experimental stress-strain results of uniaxial tensile tests on silicone samples.

Moving towards the experimental counterpart, the third and last step regards the setup of the experimental test rig for data collection. Distensibility and diameter of each vessel are

quantified by simultaneously recording the internal pressure and corresponding inflated volume of a Ø23 mm non-compliant Edwards valvuloplasty balloon. A 10 mL syringe pump is used to inflate the balloon at a constant flow rate. The syringe is moved through a non-captive stepper motor, whose speed can be reduced or increased acting on the time delay between steps within the controller. Due to the high values of pressure that can be reached while inflating the balloon, an absolute PXM4101 strain gauge pressure transducer is employed.

Each test is repeated five times for every vessel, in order to ensure the repeatability and reproducibility of the data.

The balloon is tested on several cylinders with different diameters (18, 19, 20, 21, 22, 23 mm), different shape (circular or elliptical) and different mechanical properties (rigid and compliant). After each motor step, pressure data and inflated volume are acquired, saved and plotted real-time on the graphical user interface.

By comparing experimental and computational results, the numerical model results to be very accurate, despite some little discrepancies that have been discussed in details in Chapter 4. Obtained results indicate that it should be possible to extract meaningful information from P-V data, to univocally identify diameters $\leq$ 21mm. On the other hand, it has been found that a shorter vessel slightly reduces the slope of all the P-V curves during the pressurisation phase. Moreover, it shifts to the right the P-V curves associated with diameters smaller than the non-tensioned diameter of the balloon.

Regarding instead shape variability, since ellipticity and reduction in annular length have a very similar effect on P-V curves, it might be very difficult, or even impossible, to univocally associate a curve to a combination of diameter, length and ellipticity.

Experimental data result to be closely distributed around the mean value. Low values of standard deviation indicate a great repeatability and reproducibility of the procedure.

Knowing cavity pressure and volume variations, distensibility has been numerically computed; these values (0.00124 $mmHg^{-1}$ and 0.00175 $mmHg^{-1}$ for Ø18 mm and Ø19 mm respectively) have been compared to the values extracted through experimental tests, calculated as the local slope of the V-P curves and normalised over the initial volume. Only two sizes (Ø18 mm and Ø19 mm) have been used to evaluate silicone distensibility. Since, the balloon nominal diameter is equal to 20 mm, in order to measure vessel compliance, it

is important to avoid balloon stretching, being therefore able to neglect its material properties during the computation of distensibility.

As far as Ø18 mm phantom vessel is concerned the value retrieved from experimental tests corresponds to 0.00121 $mmHg^{-1}$. The error, computed as the difference between the numerically computed and the experimental value, is therefore equal to 0.00003 $mmHg^{-1}$. According instead to Ø19 mm vessel, the distensibility is equal to 0.00195 $mmHg^{-1}$. The error, in this case, amounts to 0.0002 $mmHg^{-1}$. Standard deviation is always very low, with average values equal to 0.026 $mmHg^{-1}$ and 0.017 $mmHg^{-1}$ respectively, implying both a good reproducibility and repeatability of the measurements.

Finally, an analytical algorithm to automatically retrieve the dimension of the phantom vessel from P-V curves has been introduced and validated with experimental results. This strategy comprises two different approaches: when the vessel is smaller than the non-tensioned diameter of the balloon (20 mm, Region 1), data must be fitted with a parametrical logistic function, considering the value of the "c" parameter. This fitting has been evaluated by means of goodness-of-fit statistics (SSE, R^2 or RMSE) and it provides excellent results. Instead, when the vessel is greater than the non-tensioned diameter of the balloon, the dimension of the annulus can be retrieved by looking at one of the two coordinates of the inflection point.

In conclusion, the balloon catheter is not only able to detect the dimension of the phantom vessel but it is also sensitive to changes in annular length. On the contrary, as far as shape analysis is concerned, the device is not able to distinguish between elliptical and circular vessels if the length is not fixed. Furthermore, the balloon is able to retrieve soft tissue compliance, assuming length and shape constancy.

The clinical relevance of this work is twofold. On the one hand, it presents a cost-effective and accurate method to use a commercially available device to perform a more conservative selection of prosthesis sizes, matching the patient's anatomical dimensions and therefore reducing TAVR complications without including any kind of imaging technique. On the other side, this work lays the foundations for the future development of a new soft-robotic catheter, able to automatically obtain patient-specific implantation sites features by means of a mechatronic and completely stand-alone system.

Sommario

La stenosi valvolare aortica degenerativa è, nella sua forma più grave, una condizione cronica altamente invalidante: ad oggi, questa patologia colpisce circa il 2% dei soggetti sopra i 65 anni e, se trascurata, causa il decesso del 50% dei pazienti entro due anni dalla prima comparsa dei sintomi. Il restringimento della valvola aortica, infatti, ostacola il deflusso del sangue dal ventricolo sinistro all'aorta, provocando dispnea da sforzo, angina pectoris fino a episodi di scompenso cardiaco e morte improvvisa. In pazienti anziani, affetti da stenosi aortica severa e rischio operatorio particolarmente elevato, una valida alternativa al tradizionale intervento chirurgico è rappresentata dall'impianto transcatetere di una protesi valvolare (TAVR).

Questa tecnica mininvasiva, introdotta nel 2002, prevede un'anestesia locale ed è suddivisa in due fasi: valvuloplastica, per aprire la valvola aortica nativa e predisporre il posizionamento della protesi, e l'impianto della protesi valvolare, effettuato per via percutanea attraverso l'introduzione di un catetere munito, alla sua estremità, di un palloncino gonfiabile. Numerosi sono i progressi che si sono susseguiti negli ultimi quindici anni, in termini non solo di perfezionamento tecnico della metodica ma anche di efficacia e sicurezza dei dispositivi impiantabili. Nonostante il successo di questo approccio innovativo, l'insorgere di complicazioni post-operatorie rappresenta un continuo stimolo per studiare i potenziali rischi connessi a queste procedure e identificare i requisiti essenziali per la progettazione di nuovi dispositivi.

In particolare, è bene ricordare che un rigurgito paravalvolare anche lieve incide significativamente sulla mortalità a lungo termine e risulta essere tutt'altro che infrequente, presentandosi approssimativamente nel 40% dei pazienti. Malposizionamento o sottodimensionamento della protesi, ellitticità dell'annulus o un irregolare accumulo di

calcio nel tessuto delle valvole cardiache sono solo alcuni dei meccanismi che sono stati presi in considerazione per spiegare la comparsa di rigurgito dopo la TAVR.

Per questo motivo, è di fondamentale importanza avere informazioni accurate e attendibili sulla morfologia dell'*annulus* e sulle proprietà meccaniche del tessuto, così da poter scegliere la protesi più adatta all'anatomia del paziente migliorando al contempo i risultati di questa tecnica chirurgica.

In base alle norme attualmente in vigore, la valutazione morfologica dell'annulus viene effettuata, prima dell'intervento, mediante ecografia transesofagea bidimensionale (2D-TEE) o ecografia transtoracica bidimensionale (2D-TTE). Ciò nonostante, è stato recentemente dimostrato che tali tecniche di imaging bidimensionale non costituiscono la strategia ottimale per il corretto dimensionamento del sito di impianto, a causa della complessa geometria tridimensionale di quest'ultimo.

Per quel che riguarda invece la valutazione delle proprietà meccaniche del tessuto, ad oggi valutazioni dirette della rigidità del sito di impianto possono essere effettuate in-vitro o in-vivo. Se da un lato le analisi in-vitro presentano limiti significativi, la stima in-vivo, avvalendosi di tecniche di imaging, risulta essere più efficace, sebbene maggiormente invasiva.

Questo lavoro di tesi si pone come obiettivo quello di proporre un metodo affidabile e sicuro per dedurre le proprietà geometriche e meccaniche dell'*annulus*, senza l'utilizzo di tecniche di imaging. L'approccio descritto nei capitoli successivi si basa sull'acquisizione simultanea della pressione e del volume presenti all'interno della cavità del palloncino utilizzato per il posizionamento della valvola, acquisendo quindi informazioni sul contatto tra l'anatomia circostante e il suddetto strumento sotto forma di curve pressione-volume (P-V).

Il modello a Elementi Finiti del palloncino è stato creato partendo da immagini polariscopiche del dispositivo utilizzato nella pratica clinica. Lo sketch è stato quindi importato su Abaqus/Standard, dove è stato discretizzato, e successivamente trasferito su MSC. Marc®. Se da un lato sono state fatte delle approssimazioni per rendere il modello simmetrico, dall'altro esso risulta molto accurato, presentando uno spessore variabile attribuibile ai processi di fabbricazione del dispositivo. Al materiale è stato assegnato un comportamento isotropo elastico lineare, fornendo i valori di modulo di Young e coefficiente

di Poisson forniti dalla letteratura. Nelle simulazioni il palloncino è stato gonfiato applicando una pressione alle pareti della cavità interna; al contempo, condizioni al contorno sono state impostate affinché il modello sia vincolato a spostarsi solo radialmente. Infine, simulazioni aggiuntive che replicassero il processo di sgonfiamento del palloncino sono state introdotte al fine di ricreare la condizione collassata a tre lembi utilizzata nella pratica clinica.

Successivamente sono state svolte simulazioni numeriche su MSC. Marc® con le quali è stato possibile riprodurre il gonfiaggio del palloncino all'interno di vasi rigidi. In aggiunta, è stato creato un modello computazionale di due cilindri complianti, al fine di poterne calcolare la distensibilità. Tale distensibilità, ottenuta mediante simulazioni numeriche, è stata poi confrontata con il corrispettivo valore sperimentale, ricavato come pendenza della curva volume-pressione (V-P) e normalizzato rispetto al volume iniziale. Sono stati testati solamente due diametri (Ø18 mm and Ø19 mm), entrambi minori del diametro del palloncino a pressione atmosferica (Ø20 mm). Questo è stato fatto al fine di poter misurare solo ed esclusivamente le proprietà meccaniche del silicone, trascurando quelle del dispositivo. La procedura che è stata seguita per creare questi modelli complianti, all'interno dei quali testare le proprietà meccaniche del tessuto, è costituita da diversi fasi: (i) stima della complianza fisiologica; (ii) prove a trazione su provini in silicone; (iii) simulazioni in MSC Marc; (iv) produzione degli stampi per il silicone.

Per realizzare questi cilindri è stato scelto il silicone DragonSkin30, approssimato su MSC. Marc® con un modello Ogden del secondo ordine; i parametri ad esso associati sono stati calcolati sulla base dei risultati di una prova a trazione uniassiale sui provini in silicone.

Per quel che concerne la validazione del modello numerico, è stato appositamente sviluppato un setup sperimentale con il quale acquisire in contemporanea variazioni di volume e pressione all'interno di un palloncino Edwards per valvuloplastica, avente un diametro nominale pari a 23 mm. Collegando una siringa ad un motore stepper è stata realizzata una pompa per iniezione con la quale introdurre il fluido all'interno della cavità. Per poter misurare gli elevati valori di pressione raggiunti durante il processo di gonfiaggio, nel sistema è stato inserito anche un sensore di pressione assoluto Omega PXM4101. Ciascun test è stato ripetuto cinque volte, al fine di quantificare la ripetibilità e la riproducibilità delle suddette misure.

Il palloncino è stato testato all'interno di svariati cilindri, aventi diverso diametro (18, 19, 20, 21, 22, 23 mm), forma differente (circolare o ellittica) e diverse proprietà meccaniche (rigidi o complianti). I dati relativi a pressione e volume vengono acquisiti, salvati e mostrati a video sull'interfaccia grafica dopo ciascun *passo* del motore stepper.

Relativamente agli annuli rigidi, confrontando i risultati sperimentali con i valori numerici, si è visto come il modello computazionale realizzato in precedenza sia estremamente accurato, nonostante alcune piccole differenze, discusse in dettaglio nel Capitolo 4. I risultati dimostrano infatti come sia possibile estrarre informazioni precise e affidabili dalle curve pressione-volume per identificare in maniera univoca diametri inferiori a 21 mm. Inoltre, si può osservare dai grafici ottenuti come la pendenza delle curve diminuisca al diminuire della lunghezza dell'annulus. Tale parametro, tuttavia, sembra influire anche sulla posizione delle curve, introducendo un offset orizzontale non trascurabile. Per quel che riguarda invece la variazione di forma, dal momento che ellitticità e lunghezza sembrano avere un effetto molto simile sulle curve ottenute, è lecito pensare che con il dispositivo attualmente in uso sia difficile, se non impossibile, discriminare in maniera univoca curve in cui sia plausibile una variazione di diametro, forma e lunghezza. Infine, i dati sperimentali risultano essere distribuiti intorno alla media, essendo caratterizzati da bassi valori di deviazione standard.

Per quel che concerne invece la valutazione delle proprietà meccaniche del sito di impianto, noto il gradiente pressorio all'interno della cavità e la corrispettiva variazione di volume, la distensibilità ricavata dalle simulazioni numeriche è uguale a 0.00124 $mmHg^{-1}$ mentre il valore corrispondente ai test sperimentali è pari a 0.00121 $mmHg^{-1}$. L'errore risultante, calcolato come differenza tra i due risultati, è perciò pari a 0.00003 $mmHg^{-1}$. Per quel che riguarda invece il cilindro avente un diametro di 19 mm, 0.00175 $mmHg^{-1}$ e 0.00195 $mmHg^{-1}$ sono i valori associati rispettivamente alla complianza numerica e a quella sperimentale. In questo caso l'errore è leggermente maggiore e pari a 0.0002 $mmHg^{-1}$. Anche in questo frangente la deviazione standard dei dati sperimentali è molto bassa, con un valore medio pari a 0.026 $mmHg^{-1}$ e 0.017 $mmHg^{-1}$ nei due casi.

Per concludere, è stato ideato un algoritmo che permetta di ricavare in maniera automatica la dimensione dei siti anatomici, ipotizzandole ignote, e quindi rispecchiando ciò che accade nella realtà clinica. Questa procedura consta di due approcci differenti: i diametri inferiori ai 20 mm (diametro del palloncino a pressione atmosferica) vengono approssimati con

l’integrale parametrico della sigmoide e il diametro del vaso viene ricavato grazie ad una positiva e diretta correlazione tra il parametro “c” di tale funzione e la dimensione dell’annulus. Per quel che riguarda invece diametri maggiori di 20 mm, la posizione del punto di flesso delle curve ad essi associate è un chiaro e diretto indicatore della geometria del sito d’impianto

Il palloncino per valvuloplastica, quindi, non solo permette di dedurre la geometria del sito di impianto, ma consente di valutarne al contempo anche la lunghezza e le proprietà meccaniche. Al contrario, con il dispositivo attualmente in uso è difficile, se non impossibile, stabilire quale sia la forma dell’annulus.

La rilevanza clinica di questo lavoro è duplice. Da un lato esso fornisce un metodo economico ma soprattutto efficace con cui utilizzare un dispositivo disponibile a livello commerciale per una più precisa e consapevole scelta della protesi, adeguando quindi quest’ultima alla specifica anatomia del paziente e riducendo così eventuali effetti collaterali. Dall’altro lato, questo progetto pone le fondamenta per il futuro sviluppo di un catetere robotico che sia in grado di desumere le proprietà geometriche e meccaniche del sito di impianto, avvalendosi di un sistema meccatronico semplice e completamente autonomo.

Table of Contents

List of Figures

List of Tables

Chapter 1

INTRODUCTION

This chapter provides a comprehensive outline of the motivation for this thesis. Transcatheter Aortic Valve Replacement (TAVR) has evolved into standard therapy for elderly patients with aortic valve stenosis, who require surgical valve replacement.

An accurate assessment of the aortic annular dimensions is crucial for the success of TAVR, since the choice of an incorrectly sized prosthesis may result in catastrophic complications. Therefore, a sizing method capable of directly observing the anatomy-device interaction would be highly desirable.

This need underpins the aim of this thesis, which is to develop a soft robotic system capable of measuring physiological parameters such as vessel geometry and soft tissue compliance. This chapter presents the research background and statement as well as the objectives and the structure of the thesis.

1.1 Research Background

Cardiovascular diseases (CVD) continue to be one of the major causes of death and suffering both in developed and developing countries. An estimated 17.7 million people died from CVDs in 2015, representing 31% of all global deaths. Although most cardiovascular diseases can be prevented by addressing behavioural risk factors such as tobacco use, unhealthy diet, obesity or physical inactivity, the total number of inpatient cardiovascular operations and procedures increased by 28% between 2000 and 2010. By 2030, the total global cost of CVDs is expected to rise from approximately US$863 billion in 2010 to US$1.044 billion [1].

Among cardiovascular operations, Transcatheter Aortic Valve Replacement (TAVR) is rapidly emerging as a new minimally invasive procedure for patients with severe aortic stenosis at high surgical risk. The positive clinical outcomes allowed this technique to rapidly develop in the past fifteen years; the number of TAVR procedures worldwide is estimated to grow from 71.000 in 2015 to 289.000 in 2025. Some of the complications that have been faced in the early days have been reduced over time: in high-risk and inoperable patients, there has been a dramatic reduction in 30-day mortality over the course of less than a decade. Nevertheless, TAVR is still affected by some major intra-operative problems such as neurological events, vascular complications and post-interventional aortic regurgitation [2]–[4].
In particular, the latter occurred in 50% to 72.4% of the cases. It has been observed that even mild leaks have a crucial impact on the outcomes of the procedure and they are associated with higher mortalities at 2 years [5], [6].

In order to avoid such complications, it is compulsory for the surgeon to have accurate information on the vessel geometry and its mechanical properties, being able to properly size the prosthesis and to optimise procedure results.
According to the current recommendations, the size of the annulus is measured, prior to TAVR, either with 2D transoesophageal echocardiography (TEE) or transthoracic echocardiography (TTE) [7]. However, they seem to be not the best option to assess the complex geometry of the aortic annulus, having some procedural limitations.

This project has been developed in collaboration with the Department of Mechanical Engineering at University College of London (UCL) and the Medical Robotic Section (MRSLab) of NearLab at Politecnico di Milano (Department of Electronics, Information and Bioengineering).

1.1.1 Transcatheter Aortic Valve Replacement (TAVR)

Heart anatomy and aortic stenosis: a brief overview

The heart is a muscular organ about the size of a closed fist that works as the body's circulatory pump. It takes in deoxygenated blood through the veins and delivers it to the lungs for oxygenation before pumping it into the various arteries, which in turn provide oxygen and nutrients to peripheral tissues by transporting the blood throughout the body. The heart is located in the thoracic cavity, medial to the lungs and posterior to the sternum. As shown in Figure 1.1, on its superior end the base of the heart is attached to the aorta, to the pulmonary arteries, pulmonary veins and to the vena cava. On the other hand, the inferior tip of the heart, known as the apex, rests just superior to the diaphragm. The base of the heart is located along the body's midline, with the apex pointing toward the left side.

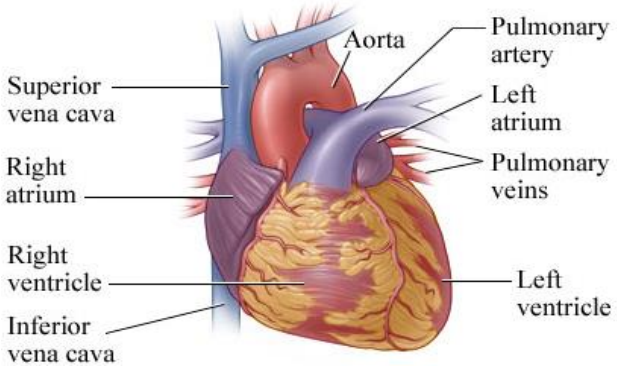

Figure 1.1 The main heart chambers. Right atrium, right ventricle, left atrium and left ventricle are shown. The figure highlights aorta and main pulmonary artery as well

The heart contains four chambers: the right atrium, left atrium, right ventricle and left ventricle. The atria are smaller than the ventricles and they have thinner, less muscular walls. The atria act as receiving chambers for blood, so they are connected to the veins that carry blood to the heart. The ventricles are the larger and stronger pumping chambers: through the arteries, they send blood out of the heart.

The chambers on the right side are smaller and have less myocardium in their wall when compared to the left side of the heart. This difference in size between the two sides of the heart is related to their functions and to the size of the two circulatory loops. The right side maintains pulmonary circulation to the nearby lungs while the left side of the heart pumps blood all the way to the extremities of the body in the systemic circulatory loop.
The four chambers of the heart are continually contracting and relaxing in a sequence known as cardiac cycle. Contraction of a chamber is called *systole* and relaxation is commonly named *diastole*.

To prevent blood from flowing backwards, a system of one-way valves is present. The heart valves can be broken down into two types: atrioventricular and semilunar valves.
The atrioventricular (AV) valves are located in the middle of the heart, between the atria and the ventricles, and they allow blood to flow only from the first to the latter during *ventricular diastole*. The AV valve on the right side of the heart is called *tricuspid valve* while the AV valve on the left side is called *mitral valve*. On the other hand, semilunar valves are located between the ventricles and the arteries, which carry blood away from the heart during the *ventricular systole*. The semilunar valve on the right side is the *pulmonary valve* while the one on the left side is the *aortic valve*. Heart valves incorporate leaflets, which are pushed open to allow blood flow and which then close together to seal and prevent backflow.
Figure 1.2 shows two different phases of the cardiac cycle, depicting two distinct configurations of the above-mentioned heart valves.

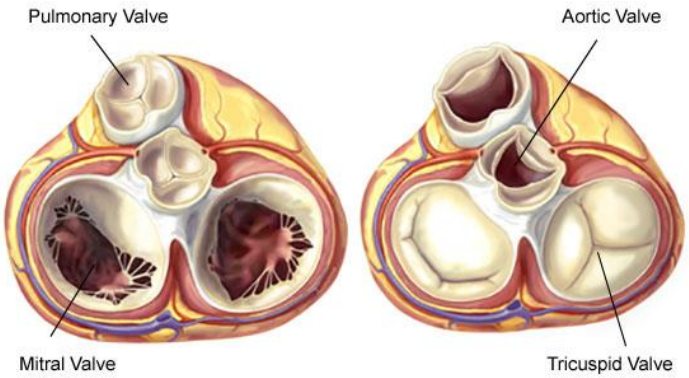

Figure 1.2 Heart valves. Atrioventricular valves are located between the atria and the ventricles while semilunar valves prevent blood from flowing back into the heart. The left side of this figure shows the ventricular diastole, characterized by the opening of the AV valves and the closing of semilunar ones. On the other hand, the ventricular systole is represented on the right-hand side, where semilunar valves are now open and AV ones are instead closed

On the left side of this figure, in fact, ventricular diastole is represented: during this phase, ventricles are relaxing and filling with blood. Atrioventricular valves are open while semilunar valves are closed, to prevent blood from flowing out from the ventricles. On the right side of Figure 1.2, instead, ventricular systole is depicted: blood moves from the ventricles to the pulmonary artery (in the case of the right ventricle) and the aorta (in the case of the left ventricle). During this phase, semilunar valves are open while atrioventricular valves are closed to prevent blood from flowing back into the atria.

The normal circulation of blood through the whole heart can be resumed as in Figure 1.3.

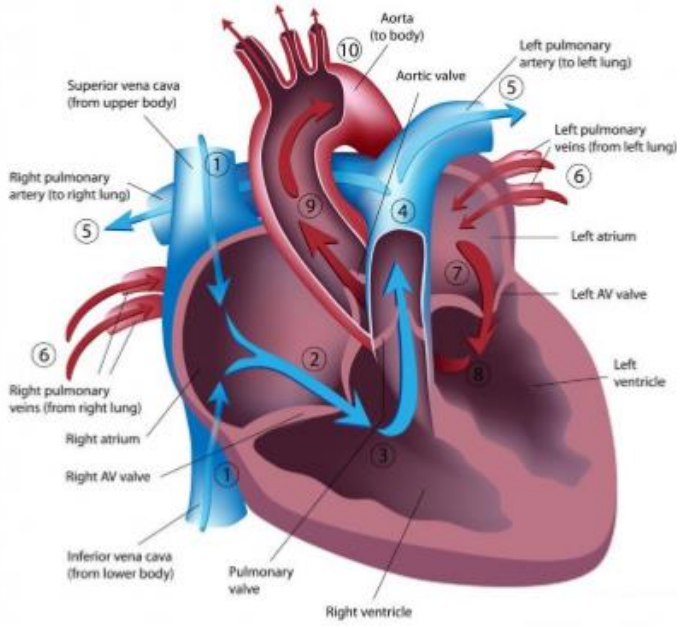

Figure 1.3 Blood flow. (1) Venous blood returns to the heart via the superior and inferior vena cava into the right atrium. Through the tricuspid valve (2), it is pumped into the right ventricle (3) and, via the pulmonary valve, it reaches the pulmonary artery (4), which delivers the blood to the lungs (5). Here the blood takes on oxygen and gives up its carbon dioxide. Later on, passing through the pulmonary veins, it enters the left atrium (6) and arrives at the left ventricle through the mitral valve (7). Finally, during contraction of the left ventricle (8), the oxygen-rich blood is pumped through the aortic valve into the aorta (9) and branching arteries, in order to be delivered to feed the rest of the body (10) before coming back to the right atrium through veins (1).

Deoxygenated blood returning from the body first enters the heart from the superior and inferior vena cava. It enters then the right atrium and it is pumped through the tricuspid valve into the right ventricle. From the right ventricle, the blood is pumped through the pulmonary semilunar valve into the pulmonary trunk. The pulmonary trunk carries blood to the lungs, where it releases carbon dioxide and absorbs oxygen. The blood in the lungs

returns to the heart through the pulmonary veins. From the pulmonary veins, blood enters the heart again in the left atrium.

Regarding instead the systemic circulation, the left atrium contracts to pump blood through the bicuspid (mitral) valve into the left ventricle. The left ventricle pumps blood through the aortic semilunar valve into the aorta. From the aorta, blood enters into systemic circulation throughout the body tissues until it returns to the heart via the vena cava and the cycle repeats.

Whilst an exhaustive anatomic description of the human heart can be found in literature, it is axiomatic that knowledge of the anatomy of the valve is fundamental in understanding the key principles involved in valvar replacement. Thus, the next paragraph focuses on aortic valvar complex and "annulus" definition.

The aortic root is the direct continuation of the left ventricular outflow tract. As shown by the blue arrow in Figure 1.4, it extends from the basal attachment of the aortic valvar leaflets within the left ventricle (green line) to their peripheral attachments at the level of the sinutubular junction (orange line). Its components are the sinuses of Valsalva, the fibrous interleaflet triangles, and the valvar leaflets themselves.

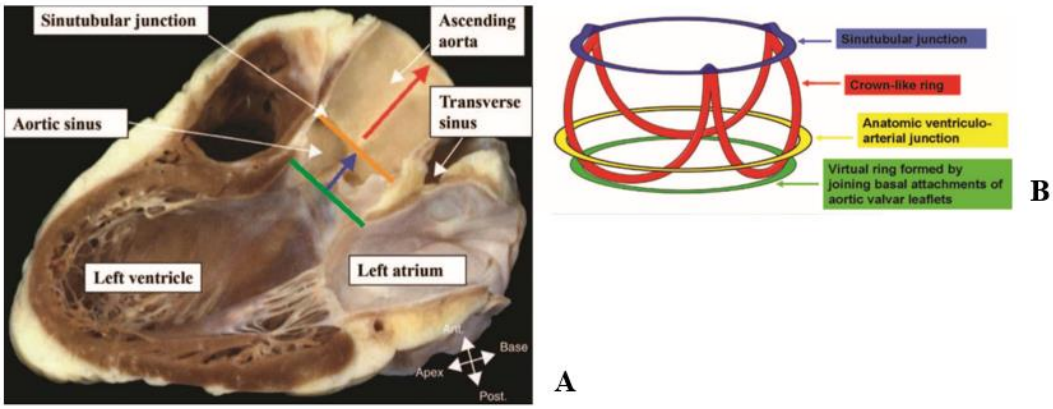

Figure 1.4 (A) A long-axis view of the left ventricle demonstrates the extent of the aortic root; (B) Three-dimensional arrangement of the aortic root, which contains 3 circular "rings," but with the leaflets suspended within the root in crown-like fashion [7].

By definition, an annulus should be no more than a little ring. However, unlike the mitral valve that has a well-defined anatomical annulus, the aortic valve annulus lacks such a distinct geometrical profile [8]. Piazza et al. [9] reported that the aortic root has a 3-dimensional structure in which three main circular rings and a crown-like ring can be recognized. In this respect, the right side of Figure 1.4 shows a three-dimensional arrangement of the aortic root, which contains two circular "rings", but with the leaflets suspended within the root in crown-like fashion.

The base of the crown is a virtual ring, formed by joining the basal attachment points of the leaflets within the left ventricle. The top of the crown is a true ring, the sinutubular junction: it forms the outlet of the aortic root into the ascending aorta. Finally, the semilunar hinges cross a third "true" ring, the anatomic ventriculoarterial junction.

With recent catheter-based aortic valve implantation procedures, the basal ring is the most relevant anatomical structure of the aortic root for proper sizing of aortic valves [10]: its diameter is currently assessed through imaging techniques and, on average, it measures 2.98 ± 0.46 cm [11].

Cardiovascular pathologies can be of different types and they can affect the heart, blood vessels or both. Aortic stenosis (AS) is the most common valvar disorder in Western countries and its prevalence is going to increase dramatically with the ageing of the population. AS is a hemodynamically significant narrowing of the outlet of the left ventricle with multiple potential causes; depending on the level of the obstruction, AS is classified as valvular, sub-valvular, or supra-valvular [5]. Aortic Stenosis is an insidious disease: it has, in fact, a long latency period and it leads to higher myocardial work, as the pumping action of the heart is seriously compromised.

Figure 1.5 focuses on the comparison between normal and stenotic aortic valves. In the first case, the valve is either completely open or tightly closed, allowing the blood to flow from the ventricles to the aorta and preventing it from flowing back into the heart respectively. In the pathological case, instead, the stenosis prevents the valve to open fully and to properly close, reducing or blocking blood flow from the heart or causing aortic regurgitation.

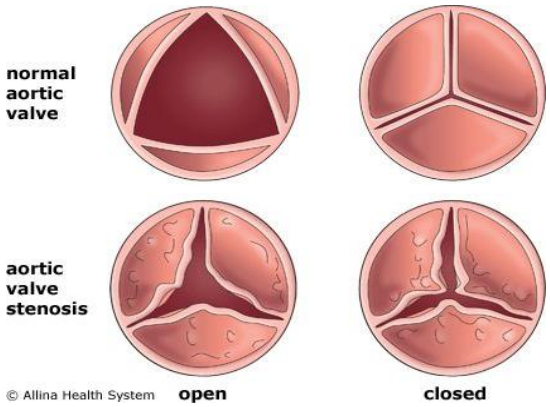

Figure 1.5 Aortic Stenosis: a comparison between normal aortic valve and stenotic one.

This pathology can lead to various degrees of LV hypertrophy, i.e. thickening of the LV wall. Severe AS can cause fainting, shortness of breath, chest pain and eventually heart failure. Moreover, it is followed by a rapid progression after the first appearance of symptoms, resulting in a high rate of death (approximately 50% in the first 2 years after symptoms appear) [12].

According to current clinical guidelines, AS can be classified as mild, moderate or severe. In order to do that, several parameters must be taken into account, considering both flow-dependent and flow-independent measurements.

The following criteria are therefore evaluated: initial aortic-valve area (or aortic-valve area index), mean pressure gradient and maximum aortic velocity. Within a multivariate analysis carried out in 2005, Pellikka et al. [13] confirmed that a peak aortic velocity greater than 4.0 m/s is a strong significant predictor for poor event-free survival without valve replacement at 2 years [14]. Regarding instead the aortic-valve area, healthy patients show a physiological value equal to 3.0-4.0 cm^2. Recent theoretical considerations have demonstrated that this parameter must be reduced to one-fourth of its natural value before significant changes in circulation occur [15].

As a result, while an area exceeding 1 cm^2 should not be defined as critical, smaller values often cause cardiac complications and death. Finally, the criteria proposed by current guidelines include also a mean pressure gradient of more than 40 mmHg.

AS affects 2% of people who are over 65 years of age and it is traditionally treated with open-heart surgery [5]. Surgical replacement of the aortic valve reduces symptoms and improves survival in patients with aortic stenosis and, in the absence of serious coexisting conditions, the procedure is associated with low operative mortality.
However, in clinical practice, at least 30% of patients with severe symptomatic aortic stenosis do not undergo surgery for replacement of the aortic valve, owing to advanced age, left ventricular dysfunction, or the presence of multiple coexisting conditions [2], [4]. For these patients, who are at high surgical risk, a less invasive treatment may be a worthwhile alternative [16].

TAVR: the procedure

Transcatheter Aortic Valve Implantation has become the most effective solution to emerge in the last decade. This procedure is revolutionary in the fact that, for the very first time, it allows the delivery of an artificial valve in the aortic position using a catheter inserted from the peripheral vessels.

In order to achieve optimal results, the procedure requires a multidisciplinary team, including a cardiac surgeon, an interventional cardiologist, and a cardiac anesthesiologist experienced in transoesophageal echocardiography. The procedure is usually performed under mild sedation or local anesthesia.

Furthermore, since the precision of Transcatheter device deployment may be hampered by cardiac motion, a temporary pacing wire (TPW) is positioned in the right ventricle via the jugular or femoral vein. Rapid Ventricular Pacing (RVP) is nowadays an established technique for temporary arrest of LV ejection during TAVR.

Throughout the procedure, echocardiography and fluoroscopy are implemented in order to continuously assess the anatomical requirements for TAVR and to guide the procedure [17].

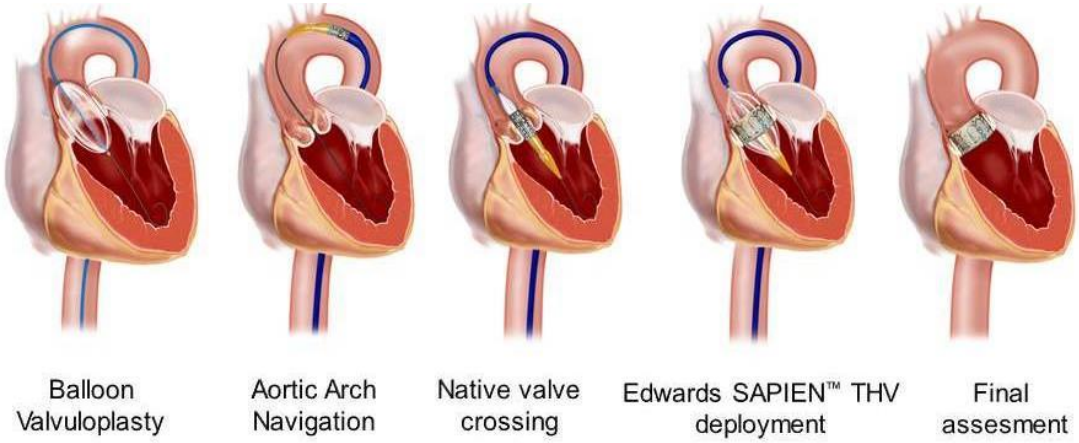

Figure 1.6 TAVR procedure: balloon valvuloplasty and deployment of Edwards SAPIEN valve

As shown in Figure 1.6, a wire is inserted into the femoral artery and is threaded up through the aorta and around the aortic arch. After this, the wire is passed through the stenotic valve and placed into the left ventricle. Once the valve is crossed, the wire is exchanged for a stiff wire with a curved tip to minimise ventricular injury over which the TAVR device is then advanced. The balloon catheter is then inflated (*balloon valvuloplasty*), opening up the stenotic valve and cracking the plaque. The new valve is delivered: either it can be expanded in the Left Ventricular Outflow Tract (LVOT) by inflating a balloon placed inside the valve within the delivery catheter or it can simply recover its expanded configuration once extracted from the catheter, depending on the type of valve used for the procedure. The wire is then removed and the new valve provides a normal flow to the heart.

This minimally invasive technique avoids the risks associated with open-heart surgery, such as the need for general anaesthesia, thoracotomy, cardiac arrest and extracorporeal circulation [18].

Initially described by Andersen in animal models in 1989, its application in humans was pioneered by Cribier in 2002. A number of delivery methods are possible, including transfemoral, transapical, transaortic, and subclavian, although the former two are the most common, accounting for 71% and 19%, respectively [19].

Among the early generation of transcatheter heart valves, two devices have been in widespread use: the self-expandable Medtronic CoreValve (Medtronic Inc) and the balloon-expandable Edwards SAPIEN valve (Edwards Lifesciences) [20].

These devices are shown in Figure 1.7 and a brief description is provided in the following lines.

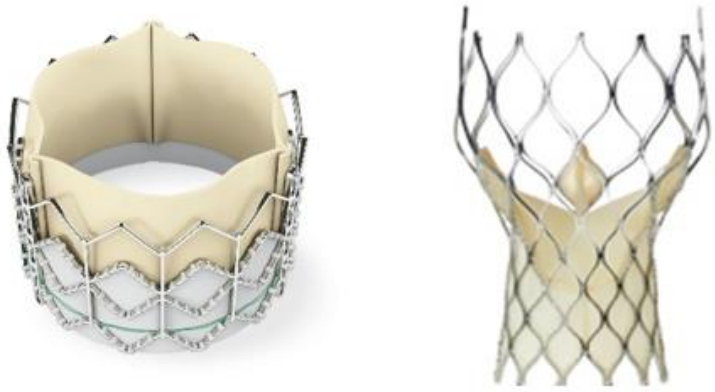

Figure 1.7 The TAVR devices: the balloon-expandable Edwards SAPIEN (left) and the self-expanding Medtronic CoreValve (right)

The Edwards SAPIEN prosthesis, shown on the left side of Figure 1.7, consists of a balloon-expandable valve with a stainless steel frame and it is expanded in the LVOT by inflating a balloon placed inside the valve within the delivery catheter. It comprises a fabric skirt and three flexible leaflets, made of fixed bovine pericardium and sutured on a stainless steel balloon-expandable stent. The valve frame is laser cut from a tube and consists of three equally spaced commissure attachment posts, interconnected by a series of beams arranges in a zigzag pattern. The prosthesis is currently available in four sizes, designated as size 20, 23, 26 and 29, treating an annulus size range of 16 mm to 27 mm diameter [18].

The CoreValve prosthesis, depicted on the right side of Figure 1.7, is a self-expanding valve characterized by a superelastic nickel-titanium alloy (Nitinol) stent, which tends to recover its expanded configuration once extracted from the catheter. It comprises a tubular skirt inflow and three flexible leaflets made of fixed porcine pericardium sutured into a self-expanding stent. The stent consists of sets of diamond-shaped cells of variable pattern along the axis, laser cut from Nitinol tube, formed with a thermos-mechanical treatment and electropolished. A unique feature is that this device is anchored not only within the aortic annulus but also extends superiorly to anchor in the supra-coronary aorta [21].

The CoreValve is available in three sizes, designated as size 26 mm, 29 mm and 31 mm, respectively recommended from aortic annulus diameters in the range of 20-23 mm, 23-27 mm and 26-29 mm.

In Table 1 a brief comparison of prosthesis previously described is provided.

	EDWARDS SAPIEN XT	**MEDTRONIC COREVALVE**
Frame	Cobalt chromium	Nitinol
Leaflets	Bovine pericardial	Porcine pericardial
Expansion	Balloon-expandable	Self-expanding
Balloon valvuloplasty required	Yes	Yes
Retrievable	No	Prior to release
Annular/valvar fixation	Yes	Yes
Manufacturers diameter	20 mm, 23 mm, 26 mm, 29 mm	26 mm, 29 mm, 31 mm
Recommended annulus diameter	18 mm – 25 mm	20 mm – 29 mm
Length	15 mm – 17 mm	53 mm – 55 mm

Table 1 Comparison of the Edwards SAPIEN XT valve and Medtronic CoreValve prostheses [20].

A very important question for the future of TAVR is how indications will be expanding in the coming years. Although this procedure was initially used to treat inoperable patients, it has already become standard for high-risk patients.

Data demonstrate that patients at intermediate risk are increasingly being treated with TAVR worldwide. A report from the TVT Registry demonstrated a median STS risk score of 7% in patients treated with TAVR from November 2011 through March 2013. During the same period, the STS score in the German GARY registry was 5.0 indicative of largely an intermediate-risk profile. Several reports from European centres demonstrate the shift to intermediate-risk patients in clinical practice and reveal low mortality and stroke rates in these patients, comparable with Surgical Aortic Valve Replacement (SAVR). Despite the great success and increasing frequency of TAVR use, the volume of SAVR has so far

remained constant. If the trend towards performing TAVR in intermediate-risk patients continues, the stability of SAVR rates will likely change downward in the near future [22].

1.1.2 TAVR: intra-operative complications

Clinical experience with these valves has confirmed the potential of TAVR, while at the same time highlighted the limitations of a techniques still in development, requiring improvements in the design of devices and implantation techniques [18].
Despite awareness of these risks, the in-hospital mortality is still 5-8%, as recently shown by the large-scale German Aortic valve RegistrY (GARY) [23].

TAVR complications can be generally divided into patient-related risks and device-related risks. While the latter may be reduced by continuously improved bioprosthesis and delivering systems with lower profiles, patient-related risks can only be addressed by a meticulous pre-interventional screening of the procedure and a careful peri- and post-interventional management. Access-related complications, cardiac tamponade, aortic root rupture, coronary obstruction, aortic regurgitation, stroke and renal failure are the most common TAVR intra-operative complications. Among access-related complications, vascular ones still occur in up to 16% of all transfemoral procedures.

Occurring at a rate of 1.1% and 0.2-0.4% of cases, aortic root rupture and coronary obstruction are generally considered rare complications. On the other hand, aortic regurgitation (AR) after TAVR has been identified as an important prognostic determinant that can be classified into transvalvular and paravalvular forms. Transvalvular AR is rare and is caused by leaflet dysfunction due to crimping or during implantation, particularly following overdilatation or uneven expansion of the prosthesis. In contrast, paravalvular AR is commonly encountered in cases where there is an eccentric shape or severely calcified annular ‘landing zone’ and undersizing, situations that promote incomplete or uneven device expansion. Another important cause of paravalvular leakage is malpositioning of the device in an axial or transverse orientation.

According to recent studies [17], the incidence of renal failure ranges from 12% to 21%. Although in the majority of the cases it is a reversible condition, it may worsen the 1-year

survival [24]. It is suggested that TAVR increases the likelihood of kidney injury. Nevertheless, this assumption could be possibly biased by the fact that most of the patients who undergo TAVR suffer from advanced peripheral vascular diseases.

Finally, Cerebrovascular Stroke (CVS) is regarded as one of the most severe complications after TAVR and it is associated with a poor prognosis. Patients with CVS are reported to have an increased risk of all-cause (42.3% vs 5.1%, $p<0.001$) and cardiovascular 30-day mortality (38.4% vs 4.6%, $p<0.001$) compared to patients without CVS. Recent data portend an incidence of 1.8% for in-hospital events and around 3% within 30 days [4].

1.1.3 Research Statement

To avoid the previously described complications, accurate annulus measurements and selection of appropriate prosthesis size are critical. Erroneous measurements can lead to serious or even fatal consequences during implantation such as valve embolization, severe paravalvular leaks or annular rupture.

To date, no gold standard for the exact measurement, prior to TAVR, of the aortic annulus diameter and compliance exists. Annulus measurements are usually performed during Transthoracic Echocardiography (TTE) or Transesophageal Echocardiography (TEE). Recently, it has been suggested that also Multislice Computed Tomography (MSCT) could provide detailed information on the shape and length of the aortic annulus.
However, being the aortic annulus a 3-dimensional structure much more complex than a simple circular ring, it has been demonstrated that bi-dimensional echocardiographic images are not the best option to assess the complex 3D geometry and the elliptic shape of the aortic annulus. Moreover, even MDCT has some procedural limitations.

Hence, the need for a simple, user-friendly, fast, cost-effective, and, most importantly, accurate modality for the assessment of the aortic annulus exists.
Once validated, this methodology could be of paramount importance to scientists developing patient-specific prosthetic heart valves, optimising the results of TAVR procedure and reducing related complications.

1.2 Aim and Objectives

The aim of this thesis is to use a commercially available balloon catheter to measure physiological parameters such as vessel geometry and soft tissue compliance. The research challenge is to develop a soft robotic device capable of accurately controlling the volume of fluid injected in the cavity and the intra-balloon pressure without the aid of imaging techniques. To achieve this aim, three main objectives have been identified:

1. Generate a numerical model of a valvuloplasty balloon catheter that can simulate, prior to experimental tests, the real behaviour of the TAVR device inside the vessel. The geometry of the model should replicate the real device as precisely as possible while material properties will be taken from literature.
   Numerical simulations have a twofold aim: on the one hand, they will be used to infer the feasibility of the herein suggested strategy while, on the other hand, they will be applied to filter the set of experimental tests, in order to both neglect non-significant analysis and to enhance meaningful comparisons.

2. Create an experimental setup interfacing a commercially available 23 mm Edwards Balloon Catheter 9350BC23. In particular, the system should be able to measure the changing over time of volume injected into the cavity and intra-balloon pressure, displaying them in terms of pressure-volume (P-V) curves. Experimental tests will validate numerical simulations verifying that a commercially available device can really improve TAVI procedure and results.

3. Compare the numerical data against experimental data and analyse the influence of changes in shape, size and annular length on both numerical and experimental P-V curves. Moreover, compute from these data the value of soft tissue compliance and create an automatic algorithm to directly retrieve from them an unknown annulus diameter.

1.3 Thesis structure

This thesis contains five chapters, which explain the steps taken to achieve the aim in Section 1.2.
In line with the objectives, a detailed structure of the thesis is shown in Figure 1.8.

Chapter 1 ("Introduction") presents the research motivation of this thesis, the research aim, objectives and the thesis structure. Moreover, the context in which the thesis is carried out, the clinical problem and the TAVR procedure are illustrated.

Chapter 2 ("Measuring soft tissue compliance and vessel geometry – State of the Art") classifies currently available methods to estimate geometrical and mechanical properties of the vessel into shape measurements (Section 2.1) and compliance measurements (Section 2.2). The literature on compliance and shape measurements is reviewed, considering both imaging techniques and alternative ones. These techniques are then compared according to measurement accuracy, clinical relevance and current availability. This review reveals that the standard imaging approach is not the most appropriate to estimate physiological properties of the annulus.

Reflecting the structure of the previous chapter, **Chapter 3 ("Material and Methods")** explains, within its three main sections, the numerical and experimental procedures followed to achieve the objectives outlined in Section 1.2. The first part (Section 3.1) presents a numerical model of the balloon catheter, retrieved from polariscopic images of the real device. The second part (Section 3.2) presents instead numerical simulations of the balloon inflation inside rigid vessels, performed using MSC. Marc® (Section 3.2.1). Moreover, starting from the deformation of the annular perimeter presented in [25], numerical models of compliant vessels have been created as well, in order to compute their distensibility (Section 3.2.2). Moving towards the experimental counterpart, Section 3.3 presents the hardware components (Section 3.3.1) and the experimental protocol (Section 3.3.2) used to validate computational results, both in terms of vessel geometry and soft tissue distensibility analysis. A Graphical User Interface (GUI) and a flowchart explaining how the algorithm has been created using the Java-Programming have been introduced as well (Section 3.3.3).

Finally, the experimental procedure followed to design and realise rapid-prototyping rigid and compliant vessels is explained (Section 3.3.4).

Chapter 4 ("Data Collection, Results and Discussion") is focused on data collection and validation of the herein described innovative approach. In Section 4.1, given the values of volume and pressure in real-time, the effect of parameters such as shape, size and annular length on both numerical (Section 4.1.1) and experimental (Section 4.1.2) P-V curves will be analysed. Two compliant cylinders made of Dragon Skin 30 will be evaluated as well, in order to assess their distensibility (Section 4.2), both numerically (Section 4.2.1) and experimentally (Section 4.2.2). Validation outcomes are discussed, demonstrating that the applied procedure is effective and of clinical relevance. Finally, in line with the previously listed objectives, an analytical method to automatically retrieve an unknown annulus diameter from P-V curves is introduced (Section 4.3).

Chapter 5 ("Conclusion and Suggestions for future work") is the final chapter of this thesis and summarises the research findings. Future work resulting from the limitations of this new experimental approach is here suggested and discussed.

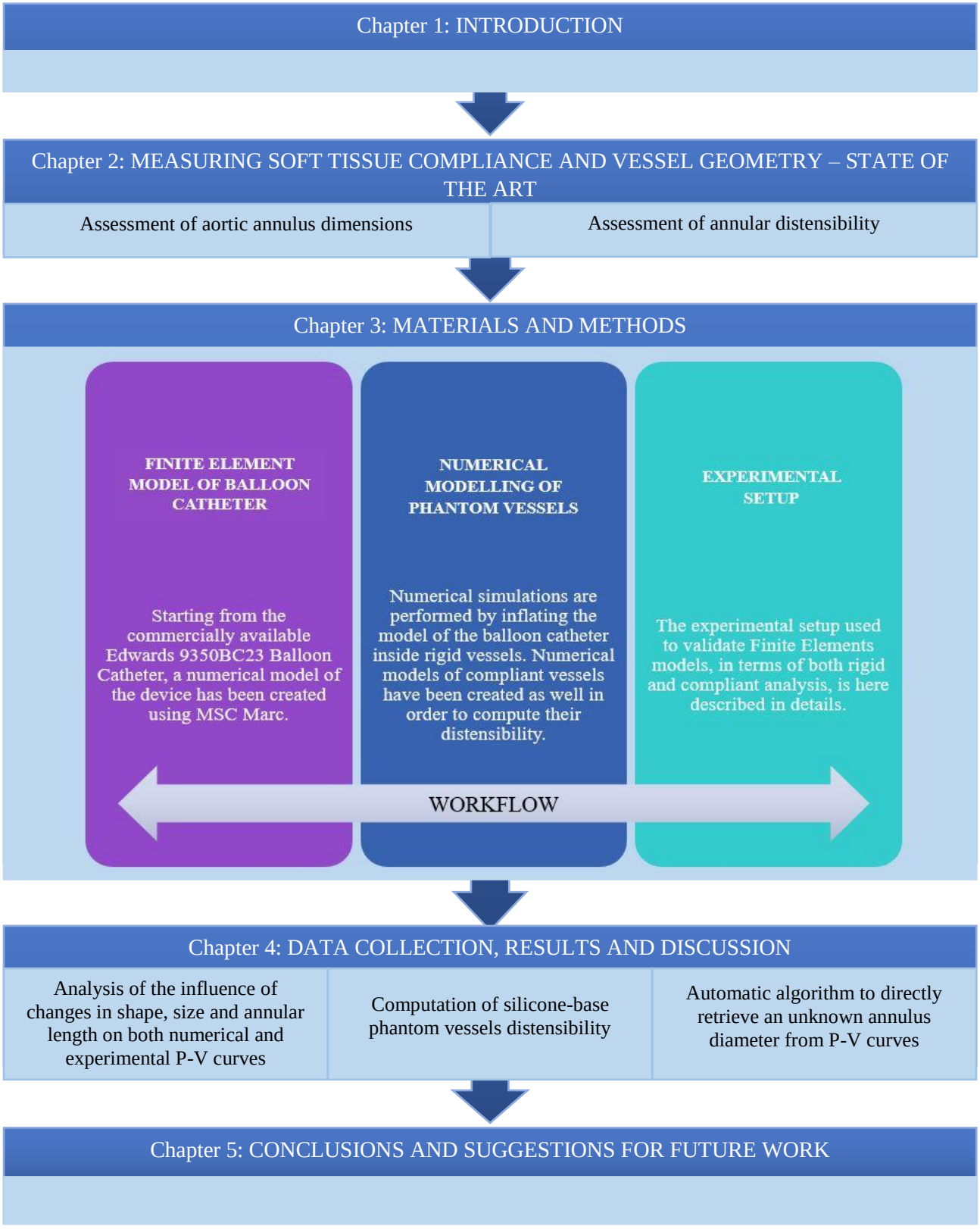

Figure 1.8 Outline of this thesis

Chapter 2

MEASURING VESSEL COMPLIANCE AND GEOMETRY – STATE OF THE ART

Precise delivery of the valve prosthesis is mandatory for successful TAVR. A stent-valve prosthesis that is placed too deep in the LV can restrict anterior mitral leaflet opening. A prosthesis that is delivered excessively antegrade toward the aortic sinuses of Valsalva can either obstruct the coronary ostia or embolize distally into the aorta.

According to current recommendations, the choice of prosthesis size is based on imaging techniques, whose results seem, however, to be dependent on operator experience. Moreover, recent researches have shown a frequent underestimation of annular dimensional measurements.

Consequently, alternative methods have been developed to overcome such limitations. The aim of the present chapter is to provide a literature review on currently available methodologies to estimate the diameter of the annulus and its mechanical properties.

2.1 Assessment of aortic annulus dimensions

2.1.1 Non-Invasive imaging tools for aortic annular sizing

In TAVR, "sizing" can be defined as the choice of the prosthesis within a range of available sizes to ensure that it is best accommodated into the native aortic root [26]. This sizing is dependent on the observation of anatomy-device interaction and represents one of the most important predictors of a successful procedure. To date, three imaging techniques have been predominantly used to perform sizing before TAVR: transthoracic echocardiography (TTE), transoesophageal echocardiography (TEE) and multidetector computed tomography (MDCT).

Transthoracic Echocardiography (TTE)

Aortic valve area (AVA) is indirectly obtained by Doppler TTE, using the continuity equation (Eq. 1) based on Newton's second law of thermodynamics, involving the conservation of mass. This principle states that the volumetric flow rate through the cardiovascular system is constant, assuming that the blood is incompressible and the conduit is inelastic [27].

$$AVA = A_{LVOT}\frac{VTI_{LVOT}}{VTI_{AO}} \qquad \text{Eq. 1}$$

Based on this principle, the aortic valve cross-sectional area is derived assuming that the stroke volume (SV) across the narrowed aortic valve orifice is equal to the SV across left ventricular outflow tract (LVOT). SV is the product of the cross-sectional area (A) and the velocity time integral (VTI) of the flow. The area at the level of the ventricular outflow tract (A_{LVOT}) is calculated from the measured LVOT diameter (by assuming a circular shape) obtained from a parasternal long axis view: this parameter is retrieved manually within 0.5-1.0 cm of the valve orifice to obtain a laminar flow curve without spectral dispersion. LVOT velocity is measured from an apical view using a pulsed wave Doppler sample volume positioned just on the left ventricular side of the aortic valve, by manually tracing the envelope of the LVOT outflow, as shown in Figure 2.1(D).

Continuous wave Doppler across the valve, presented in Figure 2.1(C), is used to determine the maximum aortic velocity: even in this case, as clear from the figure, the envelope of the flow is retrieved manually. Colour flow Doppler, depicted in Figure 2.1(B), can be used as well to determine whether or not there is a reverse blood flow from aortic valve to left ventricle cavity.

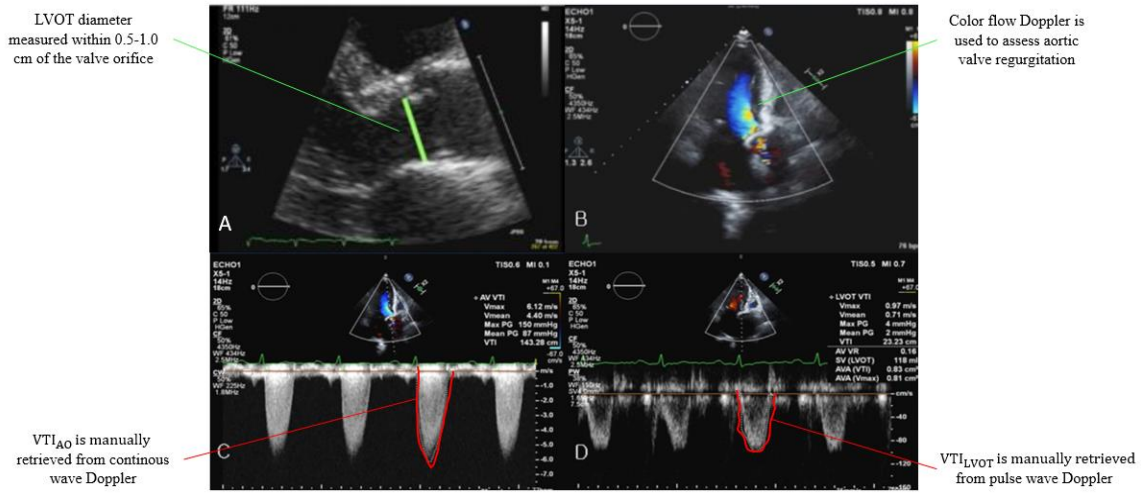

Figure 2.1 Transthoracic echocardiography: in order to compute the aortic valve cross-sectional area, the Left Ventricular Outflow Tract diameter (A), the Velocity Time Integral of the flow at the level of the aortic orifice (C) and of the LVOT (D) are manually extracted from TTE Doppler images. Moreover, Color flow Doppler can be useful for a visual assessment of the aortic regurgitation (B). Transthoracic echocardiogram reveals severe aortic valve stenosis (AS), with peak velocity through the aortic valve equal to 6.12 m/sec and a mean pressure gradient equal to 87.0 mmHg. The aortic valve area, calculated by continuity equation, is 0.81 cm^2

Echocardiography is widely available, free of ionizing radiation and contrast administration and is routinely used for diagnostic purposes, thus representing the gold standard for prosthesis size selection in TAVR. However, it shows some significant limitations. The clinical measurement variability for continuity-equation valve area depends, in fact, on the variability in each of the three measurements, including both the variability in acquiring the data and variability in measuring the recorded data [28]. AS jet and LVOT velocity measurements have a very low intra- and inter-observer variability (3–4%) both for data recording and measurement in an experienced laboratory. However, the measurement variability for LVOT diameter ranges from 5% to 8% [28]. As previously said, one of the main assumptions in the retrieval of AVA is that the LVOT shape is circular and its area can be calculated as πr^2, where $r = \frac{D}{2}$ (r radius, D diameter in the parasternal long-axis view).

This is not strictly true, since the outflow tract is in fact elliptic in cross-section and the parasternal long-axis view shows neither the largest nor the smallest ellipse diameter. Furthermore, the true outflow tract diameter is often underestimated if a tangential long-axis cut of the outflow tract is recorded, leading to underestimation of the diameter, radius, and ultimately aortic valve are.

When LVOT diameter is squared for calculation of AVA, it becomes the greatest potential source of error in the continuity equation. Finally, in atrial fibrillation, different heart cycle lengths and different preceding heart cycles make it difficult to find equivalent heart cycles for the acquisition of velocity-time integrals in the outflow tract and across the stenotic valve.

Transoesophageal Echocardiography (TEE)

Although transthoracic echocardiography (TTE) remains the cornerstone of diagnostic cardiac ultrasound, transoesophageal echocardiography (TEE) is a valuable complementary tool. In transoesophageal echocardiography, a specialized probe containing an ultrasound transducer at its tip is passed into the patient's oesophagus. As shown in Figure 2.2 (C), LVOT diameter is measured during TEE examination from the midesophageal long-axis window, by measuring the distance between the hinge point of the right leaflet and the edge of the sinus at the side of the commisures between the left and the non-coronary cusp. The esophageal view is considered suitable for measurement of LVOT diameter when the LVOT, the aortic valve, and the proximal ascending aorta are aligned, as depicted in Figure 2.2(A).

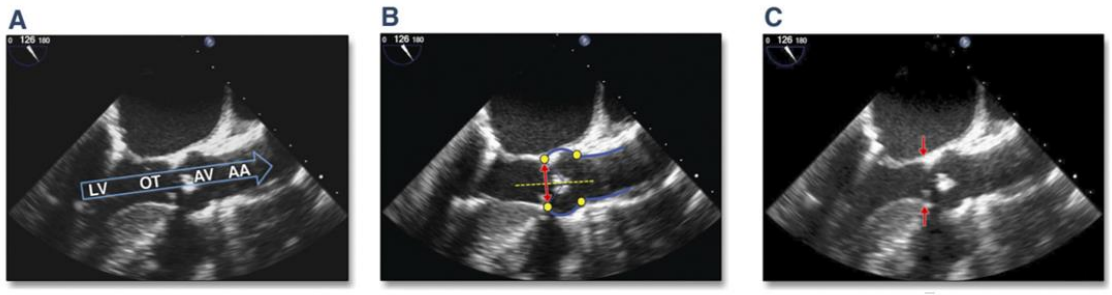

Figure 2.2 Aortic Annular View With Transoesophageal Echocardiography. Midesophageal long-axis zoomed-up view ("3-chamber view") during the early systolic phase of the cardiac cycle (A). The left ventricular chamber (LV), the outflow tract (OT), the aortic valve (AV), and the ascending aorta (AA) are aligned. An orthogonal plane is considered as a reference (B, dotted yellow line). The four edges of the aortic sinus (yellow points) are the landmarks: the sinotubular junction defines the upper reference plane, and the insertion point of the aortic valve leaflets on the outflow tract defines the lower reference plane. The aortic valve annulus is measured as the distance between the hinge point of the right cusp and the edge of the sinus at the side of the commissures between the left and non-coronary cusps, including calcifications (red line with arrowheads) (C). [26]

An orthogonal plane is considered as a reference (Figure 2.2 (B), dotted yellow line) and the four edges of the aortic sinus, depicted as yellow points in the above-mentioned figure, are the landmarks.

The advantage of TEE over TTE is usually clearer images, especially of structures that are difficult to view through the chest wall. The explanation for this is that the heart rests directly upon the oesophagus leaving only millimetres that the ultrasound beam has to travel. This reduces the attenuation, and therefore the weakening, of the ultrasound signal, generating a stronger return signal, ultimately enhancing image and Doppler quality. Comparatively, transthoracic ultrasound must first traverse skin, fat, ribs and lungs before reflecting off the heart and back to the probe before an image can be created. All these structures, along with the increased distance the beam must travel, weaken the ultrasound signal thus degrading the image and Doppler quality. TEE has generally a very high sensitivity. Moreover, according to recent researches, 2D-TEE shows a smaller inter-observer variability compared to 2D-TTE.

On the other hand, TEE may be uncomfortable for the patient, who may require sedation or general anaesthesia. Furthermore, there are some risks associated with the procedure such as oesophageal perforation or adverse reactions to the medication.

The guidelines of the American Society of Echocardiography [29] and the consensus document on TAVR [30] recommend TEE before TAVR if there are issues regarding aortic root anatomy, aortic valve annular diameter, or the number of cusps. With TEE, the size of the aortic valve annulus at the level of basal attachment or hinge points of the aortic valve cusps dictates the size of the prosthesis.

Multidetector Computed Tomography (MDCT)

After gaining more experience with TAVR and preoperative imaging, it became obvious that echocardiography might be misleading due to its limitation of two-dimensional imaging only, leading to underestimation of the annular diameter [25], [31]. Several studies have compared aortic annulus measures by MDCT with those derived from echocardiography and they have consistently shown that MDCT yielded larger diameters and possesses a higher reproducibility compared to these modalities.

Precisely, a diameter underestimation of 1–1.7mm is reported between echocardiography and MDCT/surgical measurements, which results in a different choice for a TAVR valve size in up to 44% of the cases [32].

Moreover, in patients with an oval-shaped annulus, three-dimensional (3D) imaging provides additional information as well as spatial relationships that cannot be appreciated using 2D TEE/TTE alone [33].

MDCT systems with at least 64 detectors and a spatial resolution of 0.5 mm to 0.6 mm are recommended [26]. For evaluation of the aortic root and ascending aorta, the best results are obtained with ECG gating [34]. Cardiac pulsation and motion of the aortic root frequently make accurate measurements impossible otherwise. Measurements obtained without gating may overestimate aortic diameter and lead to inappropriate referral for surgery. Whether a prospective or retrospective technique is used, gating improves accuracy and reproducibility of measurements. Moreover, image reconstruction is performed at the desired phase of the cardiac cycle (e.g., a systolic 30% to 40% phase for valve area and annular assessment). Using the retrospectively ECG-gated helical acquisition, CT data can be acquired throughout the entire cardiac cycle, enabling 4D image reconstructions for evaluation of valvular function, albeit at the expense of a higher radiation dose [21]. In contrast to transoesophageal echocardiographic measurements, MDCT imaging does not report any significant differences with respect to diameters acquired during the systolic or diastolic phase.

Although CT is a robust 3D measuring tool, it is not without limitations. The temporal resolution of cardiac CT, particularly on single-source platforms, can result in suboptimal image quality at higher heart rates. Moreover, severe valve calcification may obscure annulus assessment [35]. Finally, MDCT requires an added procedure, user interpretation of the images and exposes the patient to high doses of x-ray and contrast dye. The risk of contrast nephropathy is very high in patients with renal morbidity, which is quite common in elderly people affected by AS [36].

3D transoesophageal echocardiography (3D-TEE)

Even if in the last years 3D-TEE has become increasingly available, still this technique is not routinely accessible in every hospital [33]. Besides, up to date, it has mainly been used for intra-procedural guidance instead of sizing [37].

Recent studies confirm that 3D-TEE based TAVR screening could be feasible for prosthesis sizing, having found a non-negligible difference in aortic annulus measures assessed with 3D-TEE compared to 2D-TEE with a clear trend towards larger measures with 3D-TEE. Moreover, this difference seems to impact prosthesis size selection in a considerable amount of patients (26%) [38].

Figure 2.3 shows a visual comparison between a healthy aortic valve and a stenotic one: the latter, shown in the bottom part, depicts, in fact, large calcifications within the implantation site, causing leaflets immobility and restricted valve orifice.

Figure 2.3 3D-TEE image of aortic valve: Two favourable cases for direct TAVR implantation (A, B) and two unfavourable examples (C, D) with large calcification, sigmoid leaflets immobility with significant thickness and restricted or eccentric valve orifice (C, D)

The additional use of 3D-TEE for prosthesis size selection offers several advantages over 2D-TEE use alone.

First, with minimal extra effort (i.e., with the same probe), important additional information can be obtained in the same examination. Second, 3D-TEE data can be evaluated offline by an experienced TAVR physician: this issue may be of logistic importance as the number of TAVR procedures is expected to rise. Images can, in fact, be created by an echocardiographer not familiar with TAVR and later be evaluated by a TAVR specialist. Thirdly, the use of multiple plane reconstruction assures ideal angulations of the best plane for the assessment of the largest aortic annulus diameter possible, potentially of benefit in order to avoid paravalvular leakage by selecting larger prostheses. 3D TEE-derived annular measurements are comparable to that obtained on MDCT, with a 9.6–12.89% underestimation of cross-sectional area.

These are the main reasons why 3D transoesophageal echocardiography (3D-TEE), which offers precision comparable to MDCT and improved safety, is going to be proposed as the first image modality of choice to preoperatively assess the annular dimensions.

2.1.2 Intra-Operative alternative techniques

The previously described imaging methods are not standardized and may yield different results depending on the view obtained of the annulus, with the annulus elliptic shape contributing to the uncertainty. Although valve-sizing using 3D computed tomographic (CT) imaging has been observed to result in less aortic regurgitation, this technique is expensive and requires independent patient preparation/assessment prior to the implantation or valvuloplasty procedure and it also poses the risk of exposure to harmful radiation.
In addition, alterations to the valve annulus following a balloon valvuloplasty procedure can make it difficult to correctly size the annulus, even with current imaging techniques. For example, it is expected that a valve's annulus dimensions are altered after a balloon valvuloplasty procedure, intended to open up the diseased native valve.
Thus, given the clinical need for an alternative option for TAVR sizing that is cost-effective, alternative techniques have been suggested in the last few years.

Intraoperative sizing

During conventional aortic valve replacement (AVR), the annulus can be sized directly after decalcification of the valve and the choice of prosthesis type and size is based on these direct intraoperative measurements. After transverse opening of the aorta, the native calcified aortic leaflets, including the calcified parts of the aortic annulus, are excised and the decalcified aortic annulus is then sized using metric sizers. The circular sizers are passed through the decalcified aortic annulus. If the sizer passed through easily, the next larger sizer is used. The definitive size is based on the sizer that barely passed through. In the case of an oval-shaped annulus, the decalcified annulus adapted to the circular shape of the sizer while the sizer is passed through the annulus [31].

Calibrated balloon aortic valvuloplasty (BAV)

During rapid pacing, balloon valvuloplasty performed simultaneously with contrast injection at the level of the ascending aorta can provide an indirect confirmation of adequate sizing through several signs. Figure 2.4 shows a valvuloplasty balloon inserted within the aortic valve: arrows of different colours are used to indicate possible indirect signs of proper measurements, such as the lack of balloon movement within the aortic valve (yellow line) or the waist of the balloon at the level of the annulus (red arrows). Besides, also the absence of calcified leaflets splayed against coronary ostia (green arrow) or the lack of regurgitation of the residual contrast medium between the maximally inflated balloon and hinge points of the valve (blue line) provide an indication regarding procedure results.

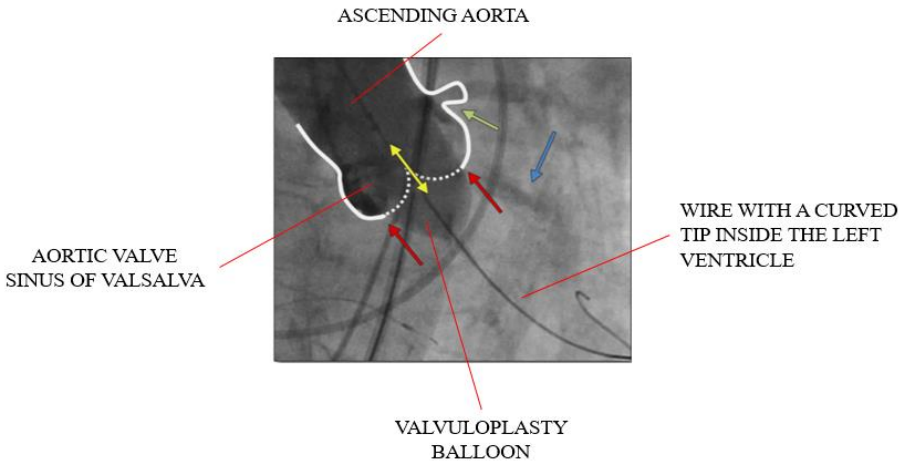

Figure 2.4 Indirect signs of proper measurements: the lack of movement of the balloon within the aortic valve (yellow line with arrowhead), the possible waste of the balloon at the level of the annulus (red arrows), the residual contrast medium regurgitation between the maximally inflated balloon and the hinge points of the valve (blue arrow), and the calcified leaflets splayed against coronary ostia (green arrow) [26].

On this latter principle is based the simple approach presented by Alain Cribier, the interventional cardiologist who performed the first ever TAVR. This methodology relies on angiographic images and a BAV balloon catheter: in this case, in fact, the size of the annulus is retrieved by inflating the balloon until the diameter that stops the flow of the contrast agent across the aortic valve is reached. The main drawbacks are given by the fact that a visual and therefore subjective interpretation is required: entity of aortic regurgitation is retrieved on aortography at full balloon inflation. Furthermore, multiple balloons are needed to perform the procedure and balloon sizes are based on manufacturer *ex-vivo* pressure compliance charts [32].

In [39], a very intuitive preoperative calibration for a BAV balloon catheter is described as well. The BAV catheter is connected via 4-way stopclock to an inflator device for pressure measurements and a 30 cc inflation syringe. The volume in the inflation syringe is adjusted so that 2 atms of intra-balloon pressure are generated at maximum inflation. The balloon is then deflated, inserted retrograde through the aortic valve, and used for BAV during rapid right ventricular pacing. At full inflation, the intra-balloon pressure is recorded. If the intra-balloon pressure did not exceed 2 atms, there is no force exerted by the aortic annulus on the balloon, and, hence, the annulus is larger than the balloon. If, on the contrary, the intra-balloon pressure exceeded 2 atms, the annulus size has been reached.
A schematic of BAV annulus sizing is shown in Figure 2.5.

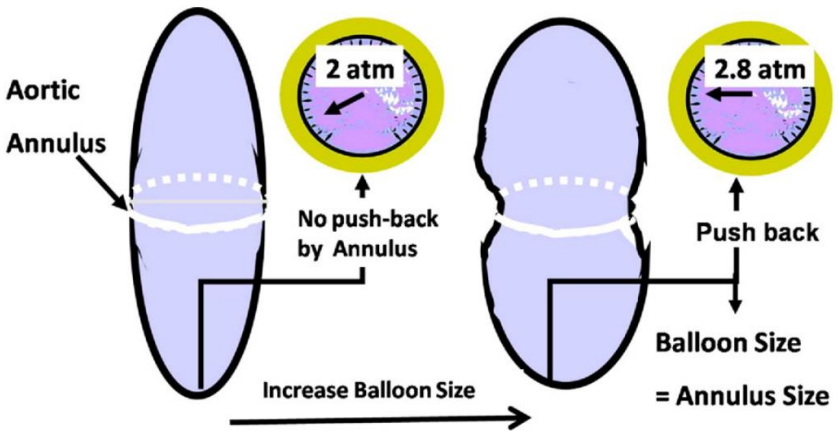

Figure 2.5 Schematic of Aortic Annulus Sizing by BAV Catheter. After the preparation on a sterile table, the balloon aortic valvuloplasty (BAV) catheter is inflated across the aortic valve. If no additional intra-balloon pressure is generated, the balloon is too small and the procedure should be repeated with a larger size. Once additional pressure is generated, the balloon annulus size has been reached [38]

A similar technique has been proposed in [7] as well. Both the solutions allow estimating the annular dimensions through intra-balloon pressure measurements and, for their simplicity, result to be very attractive. Moreover, the measurements can be made with existing devices, the data can be acquired safely during routine BAV and the selection of THV is simple (use the smallest THV greater than the balloon annulus size). As reported by Babaliaros et al. [38], the annulus measured by BAV was 1 mm larger than that found on TEE, with discrepancies up to 3.5 mm. In 26% of the cases (7 out of 27) a different size prosthesis size was selected as a result of the aforementioned procedure, with TEE annulus size considered “borderline”.

However, the precision of this procedure is highly limited by the fact that every step, from the control of the balloon inflation to the interpretation of the feedback, is manually carried out by the operator.

Aortic sizing valvuloplasty conductance balloon (SVCB)

Recently, a more sophisticated catheter that uses conductance measurements to track the diameter of the balloon in real-time, has been developed [26].

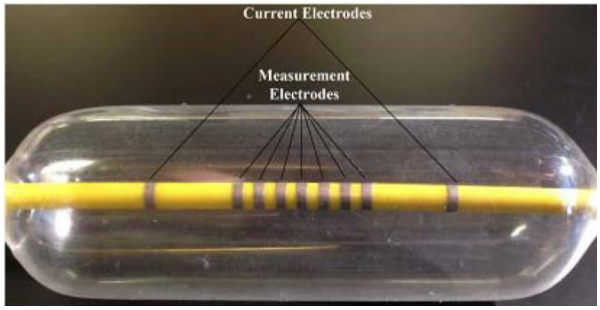

Figure 2.6 Balloon catheter with fluoroscopic markers. The balloon shows the outer electrodes used for the injection of the constant electric current and the middle electrodes, used for the measurement of the balloon size through voltage measurements [32] .

The outer electrodes shown in Figure 2.6 and placed inside either ends of the balloon serve as standard fluoroscopic edge markers in addition to serving as excitation sensors for the balloon sizing measurements. By applying a small amount of alternating electrical current (136 μA, 1–10kHz) through the outer two electrodes, it is possible to estimate the outer cross-sectional area (CSA) based on conductance measurements made by adjacent pairs of the middle electrodes. Cross-sectional area and diameter are retrieved from Ohm's law:

$$A = \frac{IL}{V\sigma}, \qquad D = \sqrt{\frac{4IL}{\pi V\sigma}} \qquad \text{Eq. 2}$$

where I represents the current, L indicates the distance between electrodes, V is the measured voltage and σ stands for conductivity. Even if this solution guarantees a more direct and accurate estimate of the annular cross-sectional area, showing an accuracy of -0.11 ± 0.26 mm if compared to the true diameter for phantom measurements, the inflation is still manually controlled. Furthermore, the system cannot provide any information regarding the mechanical properties of the tissue.

A comparison of the above-described procedures is made in Table 2. The table classifies different techniques by means of their capability of estimating annulus dimension and annulus ellipticity. Moreover, procedure invasiveness and current availability are reported as well.

Currently available procedures to estimate soft tissue compliance are described and compared in the next chapter.

	Annular dimension	Annular ellipticity	Invasiveness	Commercial availability
Transthoracic Echocardiography (TTE)	Possible underestimation due to bi-dimensional assessment	Not Detected	Non-Invasive	Yes
Transoesophageal Echocardiography (TEE)	Possible underestimation due to bi-dimensional assessment	Not Detected	Invasive	Yes
Multidetector Computed Tomography (MDCT)	Possible underestimation in case of severe calcification	Detected	Risk of contrast nephropathy	Yes
3D transoesophageal echocardiography (3D-TEE)	Accurate estimation (9.6–12.89% underestimation of AVA if compared to MDCT)	Detected	Invasive	Not yet
Intraoperative Sizing	Accurate estimation (Gold Standard)	Detected	Invasive	Yes
Balloon Valvuloplasty [7], [25]	Possible mistakes since the entire procedure is manually carried out by the operator	Not Detected	Non-Invasive	No
Valvuloplasty Conductance Balloon [32]	Possible mistakes since the entire procedure is manually carried out by the operator	Not Detected	Non-Invasive	No

Table 2 Comparison of different techniques currently available to estimate vessel geometry

2.2 Assessment of annular distensibility

Once the diameter is determined, the interventional cardiologist has to decide which valve to select from a relatively limited number of options. It would then be desirable to know the degree to which the annulus distends under pressure. If the annulus results to be suitably distensible, the interventional cardiologist would be in a better position to select a larger valve size in order to reduce paravalvular leakage, while at the same time being better able to assess the risk of annular rupture given this added knowledge of distensibility [40]. Besides, the proven efficacy of TAVR in high-risk patients is leading to the expansion of its indications toward lower-risk and younger patients, whose vessels are expected to be more compliant and distensible if compared to elder people. These are the main reasons why it is important to know the mechanical properties of the tissue besides its geometrical configuration.

By definition, the compliance (C) of a hollow body is the ability to distend and increase the volume of the cavity for any given applied trans-mural pressure. This important mechanical parameter is expressed by the following formula:

$$C = \frac{\Delta V}{\Delta P}\left[\frac{mL}{mmHg}\right] \qquad \text{Eq. 3}$$

where ΔV represents the internal volume variation due to an increase of internal pressure ΔP. If the Pressure-Volume (P-V) relationship is not linear, C is calculated as the local slope of the P-V curve. Because it is often useful to have material properties, which are independent of the particular geometry, normalizing the compliance over the initial volume brings to the definition of distensibility (D).

The latter is obtained through Eq. 4:

$$D = \frac{\Delta V}{V_0 \Delta P}[mmHg^{-1}] \qquad \text{Eq. 4}$$

Consequently, physiological vessel compliance is defined as the change in vessel volume (or cross-sectional area) that occurs during the cardiac cycle, divided by the corresponding change in blood pressure (40 mmHg).

To date, direct measurements of vascular stiffness can be performed in vitro or in vivo. In both cases, the aim is to quantify variation of arterial diameter and to correlate it with the associated pressure acting on the arterial wall, by means of Pressure-Diameter curves.

2.2.1 Mechanical Testing of biological tissue

In vitro assessments are mainly referred to mechanical testing of animal or human biological samples. They allow the measurements of both inner and outer diameter, as well as other parameters influencing the mechanical response, leading to a complex interpretation of the material structure and behaviour. However, factors such as the pre-tensional state, the presence of tissue surrounding the vessel, the active action of cells and muscular fibres, the dynamic effect of the pulsatile flow cannot be taken into account, as well as the high variability of properties inter and intraspecies. Focusing on assessing in vitro arterial wall tissue properties, an interesting study described a method to obtain the annular distensibility of the AV on explanted pig hearts [40].

2.2.2 Non-Invasive imaging techniques to measure soft tissue distensibility

To overcome the limitations of in vitro test and assess patient-specific material properties, in vivo non-invasive techniques are appealing. In this case, either internal or external diameter is measured by imaging techniques. Wall thickness is instead either assumed or ignored, while pressure is acquired simultaneously during catheterisation or with a sphygmomanometer at the upper arm during physiological conditions.

Regarding imaging techniques, previous attempts have been made to assess annular distensibility using magnetic resonance imaging [41] or CT [42]. However, it has been suggested [43] that imaging alone may thus need to be enhanced to elicit the mechanical response of the native tissue to the stress of the valve deployment, which unfortunately cannot always be preoperatively predicted [18]. Hamdan et al. [42] measured aortic annulus shape and dimension variation over the cardiac cycle on 256-slice CT images, with the aim to obtain a parameter to easily size the annulus prior to TAVR. In addition, a value of the elastic modulus was calculated as tensile stress over circumferential strain, by assuming the aortic annulus as an Elastic Annular Element. However, the author underlines the limitation of this technique in assessing arterial properties during overloading, such as in the presence of a valved-stent device being released and implanted.

Likewise, CT ECG-synchronised images were considered by De Heer et al. [44]. who analysed dynamic changes of AV annulus elliptical shape during the cardiac cycle.

Sophisticated algorithms have been developed to extract accurate information from CT images as well. Schlicht et al. [45] worked on the validation of a new method to measure in vivo elastic properties of the arterial wall. The elastic modulus of a PDMS aortic model inserted into a pulsatile mock loop was calculated by means of CT data and the results were validated against the mechanical properties of the material, obtained with mechanical testing. Finally, another iterative numerical method has been recently developed to determine in vivo the elastic properties of human aortic samples from 4D ultrasound data. This offers a non-invasive solution suitable for the detection of patient-specific material properties, which has been numerically verified but not yet validated against bench data. Furthermore, it still requires a high computational cost.

2.3 Summary

This chapter presented a literature review regarding experimental techniques that are currently in use to measure geometrical properties of the aortic annulus and its physiological compliance. Prior to TAVR, annulus size can be estimated using either imaging techniques or intra-balloon pressure measurements. Additionally, a more sophisticated catheter that uses conductance measurements to track the diameter of the balloon in real-time has been introduced. On the other hand, in-vitro or in-vivo measurements provide compliance measurements. While the former has some significant limitations, not taking into account factors such as the pre-tensional state of the annulus or the dynamic effect of the pulsatile flow, the latter overcome such weaknesses using imaging techniques.

Among the above-mentioned procedures, intra-balloon pressure measurements have been chosen as a starting point to develop the herein described soft robotic balloon catheter.

Chapter 3

MATERIALS AND METHODS

This Chapter explains, within its three main sections, the numerical and experimental procedures followed to solve a twofold problem: to determine the aortic annulus geometry and to retrieve its distensibility using a commercially available balloon catheter.

The first section describes in details the Finite Element model of the balloon catheter, in terms of geometry, mesh, boundary conditions, loadcases and job analysis.

Subsequently, the second section of this chapter focuses on numerical simulations, performed on MSC. Marc® by inflating the previously described numerical model of the balloon catheter inside rigid vessels. Moreover, numerical models of compliant vessels have been created as well, in order to compute their distensibility.

Moving towards the experimental counterpart, the third and last section of this Chapter provides a comprehensive overview on both the experimental setup and the experimental protocol used to validate computational results, in terms of vessel geometry and soft tissue distensibility analysis. Furthermore, a Graphical User Interface (GUI) and a flowchart explaining how the algorithm has been created using the Java-Programming have been introduced as well. Finally, the experimental procedure followed to design and realise rapid-prototyping rigid and compliant vessels is explained in details.

3.1 Finite Element Model of the Valvuloplasty Balloon Catheter

The herein described Finite Element Model of the Valvuloplasty Balloon Catheter has been realised from the real commercially available Edwards BAV Balloon Catheter 9350BC23. This is why, before reporting the detailed description of the numerical model, a general overview of the real device is provided.

Balloons are cardiovascular devices adopted in several minimally invasive procedures, such as sizing [39], aortic expansion [46], angioplasty [47], stent or percutaneous valves [48] expansion and valvuloplasty [49]. Balloons are generally characterised by the following parameters: nominal and burst pressure, nominal diameter (i.e. the diameter at which the nominal pressure is reached), and balloon length, typically referred as the length of the cylindrical region.

Within this project, a non-compliant high-pressure Ø23 mm Edwards BAV Balloon Catheter 9350BC23 has been used, whose main specifications are listed in Table 3.

Balloon	Dimensions	Nominal Diameter	Nominal Volume	Nominal Pressure	Burst Pressure
Edwards 9350BC20	20x40x75 mm	23 mm	16 mL	4 atm	6 atm

Table 3 Balloon specifications: dimensions, nominal diameter, nominal volume, nominal pressure and burst pressure are indicated

During valvuloplasty, the balloon dilates the existing calcified valve and it expands to deploy the new one. As a result, the balloon must be tear-resistant and must have high burst pressures, with nominal pressures typically ranging from 4 to 8 atm and rated burst pressures in the range of 6–20 atm [50]. Furthermore, the balloon must have very thin walls, typically in the order of 0.1 mm. Catheters, in fact, are typically inserted through a narrow-gauge introducer (e.g., 5 or 6 Fr) into the femoral artery, and the balloons are placed in a constricted passage within the stenosis. Under these circumstances, thanks to its small thickness, by applying a negative pressure the balloon is able to fold over and down in order to provide the type of low profile that is desirable for insertion through a guiding catheter and especially through the narrowed artery that is to be dilated.

Figure 3.1 (a) displays a CT-based reconstruction of balloon tri-folded configuration; the effect of this folding is still visible on unfolded balloon on the left (b), as shown by the presence of several creases on its surface.

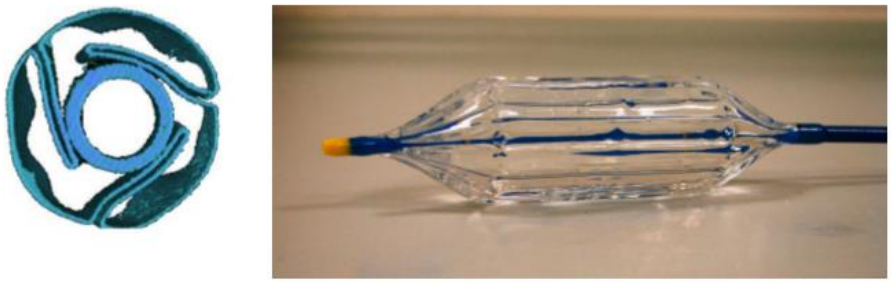

Figure 3.1 Micro-CT based reconstruction of the tri-folded configuration (a), and Edwards valvuloplasty balloon (b): the folded configuration is clearly visible [50]

On the other hand, small wall thickness means lower balloon strength; a high strength dilatation balloon, which is therefore capable of withstanding increased inflation pressure, is safer to use since the chances of the balloon bursting during the procedure are minimized. The stresses in a standard balloon can be computed as follows, where Eq. 5 defines the hoop or radial stress and Eq. 6 describes the axial or longitudinal stress.

$$\sigma_r = \frac{pd}{2t} \qquad \text{Eq. 5}$$

$$\sigma_i = \frac{pd}{4t} \qquad \text{Eq. 6}$$

p indicates the balloon burst pressure (i.e. the average pressure required to rupture a balloon, generally determined at 37° C); d represents the balloon diameter while t stands for balloon thickness (assumed to be constant). Fortunately, the radial stress is generally twice the longitudinal stress; therefore, when a balloon fails, normally it splits along its length rather than circumferentially. Clinically speaking, that is desirable, since a circumferential balloon failure can cause complications in many medical procedures.

Another important feature of balloons is distensibility, which is also referred to as percent of radial expansion.

It is typically determined by comparing the nominal or rated diameter of the balloon with the diameter at some arbitrarily selected higher pressure (e.g., 10 bars) according to Eq. 7:

$$D = \left[\frac{D_{10}}{D_0} - 1\right] * 100\% \qquad \text{Eq. 7}$$

where D indicates the balloon distensibility, D_{10} represents the balloon diameter at 10 bars and D_0 is the nominal balloon diameter (typically achieved when the balloon is inflated between 4 bars to about 8 bars). For example, balloons made of polyethylene terephthalate have a low distensibility.

For the purpose of this specific project, a maximum pressure equal to 4.5 atm has been selected in order to minimise the balloon distensibility. Under this assumption, the intra-balloon pressure can be considered as the pressure applied to the internal walls of the vessel, neglecting completely the material properties of the balloon. As a result, compliance values measured as volume variation over intra-balloon pressure difference are exclusively associated to the tissue and not to the balloon.

Finally, to prevent damage to vessel walls caused by over-inflation, balloons must have reliable diameters at nominal pressure. For the same reason, they must also be non-compliant or semi-compliant, so that they will not inflate significantly beyond their respective designated dilation diameters, thereby minimizing possible over-inflation errors.

The increase in size past the nominal pressure is therefore limited and approximately equal to 5–10% from nominal to rated burst pressure.

Each device consists of a flexible shaft and a balloon, as shown in Figure 3.2.

At the proximal end of the catheter, there is a standard Y-connector for balloon inflation and the guidewire lumen. The balloon itself is made of a thin transparent polymer, and a bendable catheter with radiopaque markers indicating the working length of the balloon is positioned along its longitudinal axis.

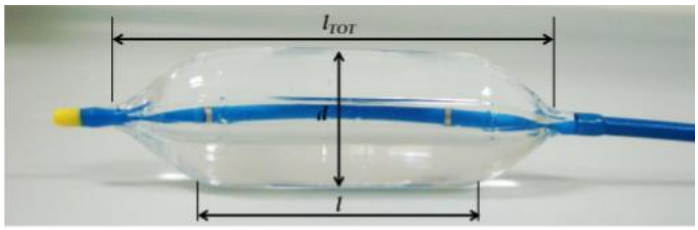

Figure 3.2 The main dimensions of balloons, i.e. diameter d, total length l_{TOT} and length of the cylindrical portion, l.

Currently available materials are polyethylene terephthalate (PET), Nylon (Nylon 6 or Nylon 12), polytetrafluoroethylene (PTFE) and polyurethane (PU). These non-compliant materials exhibit in fact high tensile strength with relatively low elongation and maintain their designed size and shape even under high pressure. The conclusions presented in the following chapters, attained on Edwards 23 mm, could be extended to Edwards balloons of different sizes, under the assumption that they are made of the same material and produced with the same manufacturing technique.

Moving now towards Finite Elements Analysis, numerical simulations and computational model of the valvuloplasty balloon catheter have been developed using MSC. Marc® by the MSC Software Corporation (Santa Ana, California). Amongst the list of the capabilities of MSC. Marc®, the most important, for the purpose of this investigation, is that it is inherently a nonlinear FEA program, able to support all problems involving not only material nonlinearities but also geometric nonlinearities (large displacements and deformations) and boundary nonlinearities.

The analysis is divided into multiple steps, such as balloon geometry, material properties, mesh, boundary conditions and loadcases. The modeling procedures and parameters used to model each of these steps in MSC. Marc® will be discussed in this section.

a. Balloon Geometry and Contact Bodies

The Edwards BAV Balloon Catheter 9350BC23 model has been reconstructed from polariscopic images by using computer-aided design software (version 2017; SolidWorks, Concord, Mass). The first step in this process has been to put the BAV balloon catheter behind the polaroid plate of the polariscope, with a ruler alongside it. Following this, the picture shown in Figure 3.3 (A) has been taken and successively uploaded on Solidworks.

The image has been scaled using the ruler as a reference. By tracing contours of the underlying image (B), the sketch presented in Figure 3.3 (C) has been realised.

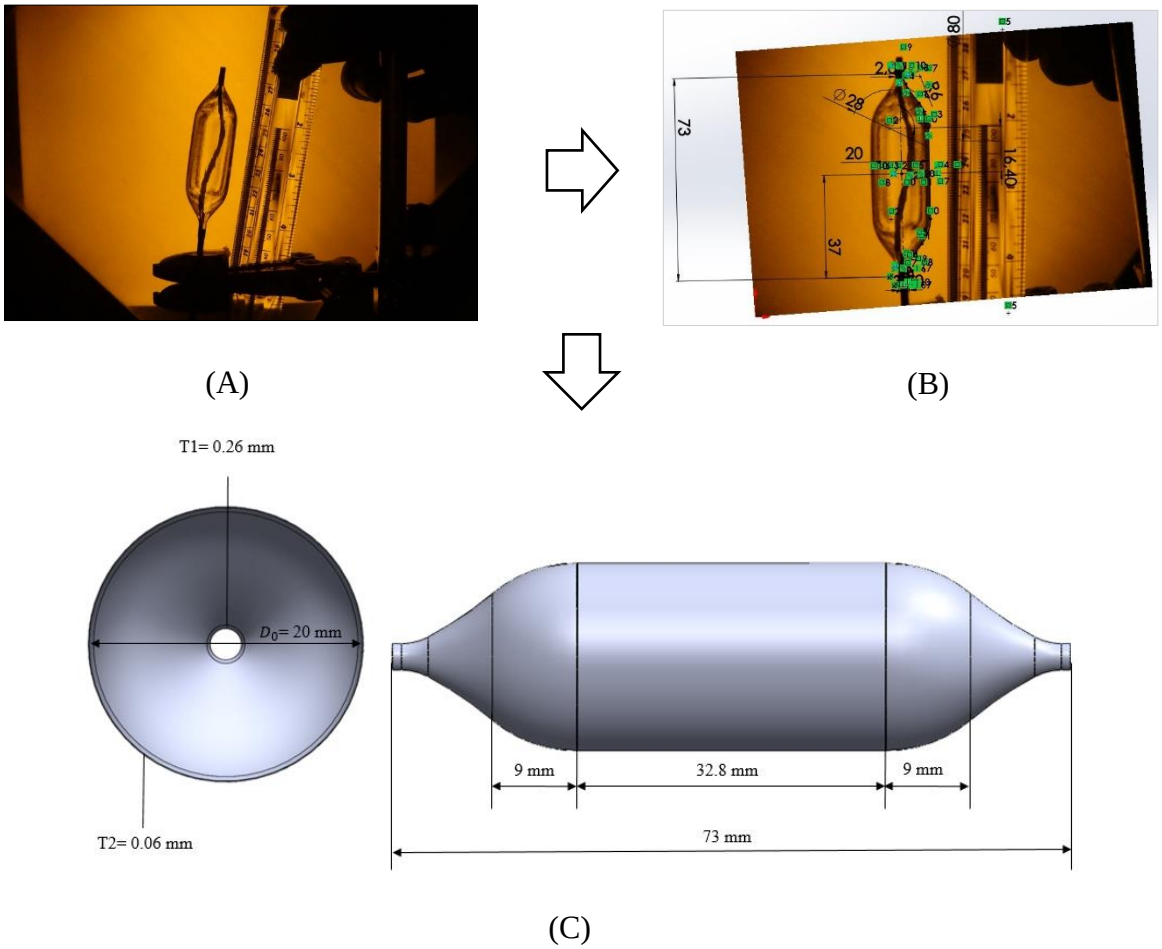

Figure 3.3 Balloon reconstruction from polariscopic images: (A) picture of the BAV balloon catheter and the ruler behind polaroid plate; (B) Solidworks sketch has been created by tracing contours of the underlying image (B); (C) BAV Balloon catheter sketch on Solidworks: T1=extremities thickness; T2=cylindrical thickness; D_0 = balloon nominal diameter

The use of a polariscope allows to clearly see and outline the contours of a transparent device such as the balloon catheter, increasing therefore the accuracy of the above-mentioned procedure. The sketch has then been imported into Abaqus/Standard (Simulia, Inc., Providence, RI, USA) to generate a hexahedral element mesh and finally transferred to MSC. Marc® for further finite element analyses.

While approximations have been made to make the part symmetric, the real variable thickness has been considered along the longitudinal axis. According to data found in literature, extremities and cylindrical part have been modeled with a thickness of 0.26 mm and 0.06 mm respectively.

This thickness variability is attributed to manufacturing techniques. In the balloon-forming process, in fact, a parison is placed into a mold. The parison is stretched while pressurized internally with clean, dry nitrogen and under a controlled elevated temperature from surrounding heating elements. This process promotes balloon formation. Then, a secondary stretch at lower pressures (i.e. typically one-third or less of the forming pressure) is often used after the main balloon body is formed in order to create thinner cones and neck wall thicknesses.

The balloon has angular geometric symmetry and therefore only one-third of its circumference, covering 120°, has been modeled. In addition, this inflatable device has axial symmetry, so that the model has been further reduced by half (i.e. longitudinal length of 25 mm instead of 50 mm).
Under these assumptions, only one-sixth of the balloon has been represented, as shown in Figure 3.4.

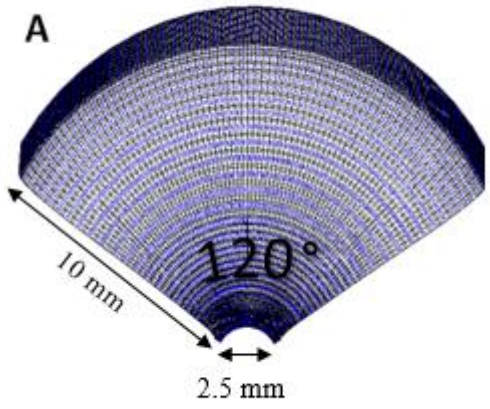

Figure 3.4 Balloon Geometry. The balloon is considered symmetric: under this assumption, only one-sixth of the balloon has been represented. The model presents in fact a cylindrical part whose longitudinal length is equal to one half of the overall length and it represents only one-third of its cross-sectional area. This figure has been taken from MSC Marc.

In this case, the overall model consists of multiple bodies and one of its main aims is to simulate their mutual interaction; therefore, they must be all defined as contact bodies on MSC. Marc®.

Contact bodies can be classified as meshed deformable, meshed rigid or geometric.

The balloon has been defined as meshed and deformable while the inner tube, which represents the catheter, is instead geometric and rigid. The contact between the individual bodies in the model (rigid body-to-deformable body, deformable-to-other deformable body) is detected automatically in MSC. Marc® and the surface properties associated with it are appropriately defined in the contact definition processor of the program.

The balloon diameter at atmospheric pressure has been set equal to 20 mm while 2.5 mm is the diameter of the inner tube. A cylindrical coordinates system has been used and the model has been meshed and 'wrapped' into a cylindrical shape. The origin of this system lies on the anterior surface of the balloon.

b. Model Meshing and Material

The finite element mesh subdivides the geometry into elements, upon which nodes are found. The nodes, which are really just point locations in space, are generally located at the element corners. While for a two-dimensional (2D) analysis the elements are essentially 2D, for a 3D solid evaluation elements must have a physical thickness in all three dimensions. MSC. Marc® employs a wide variety of different element classes.

In three-dimensional (3D) finite element analysis, two types of element shapes are commonly utilised for mesh generation: tetrahedral and hexahedral. Hexahedral elements are generally preferred over tetrahedral elements because of their superior performance in terms of convergence rate and accuracy of the solution. A mesh with hexahedral elements requires, in fact, a lower number of elements and it is easier to visualise and edit. On the other hand, linear tetrahedral elements are very stiff and exhibit the phenomena of volumetric and shear locking [51]. Moreover, the choice of this element type (over higher order elements) has been informed by recommendation from the MSC. Marc® literature, which indicates it as the most suitable for problems of this nature.

As a result, the inflatable balloon has been discretised into 13824 hexahedral 8-noded elements. This mesh seems to be a good trade-off between accuracy and efficiency: the more elements used in the model, in fact, the closer the results get to the actual behaviour.

Required material properties vary with the type of solution. A linear static analysis, for example, requires an elastic modulus, Poisson's ratio and perhaps a density for each material. As claimed by S. Tzamtzis et al. [18], a Young Modulus equal to 600 MPa and a Poisson's ratio of 0.45 have been chosen. In contrast, hyperelastic materials are described through a strain-energy density function. There are several models proposed in the literature such as Neo-Hookean, Mooney-Rivlin, Ogden, Yeoh, Arruda-Boyce models, which are all available on MSC. Marc®. These models have been used to describe the behaviour of silicone compliant vessels, whose manufacturing process is going to be discussed in Section 3.2.2.

The 3D internal cavity of the balloon has been defined using the 3456 element faces that constitute the inner surface. The internal volume of the balloon is assumed to be made of several elements having fluid properties; the bulk modulus has been set equal to 2150 MPa with a Reference Density of 1e-009.

c. Boundary Conditions

The boundary conditions for the model are also depicted. Boundary conditions, which can be applied to points, surfaces, edges, nodes or elements, are used to prevent the model from translating and/or rotating in a given direction. When the model is analysed, an equation is generated for each degree of freedom of each node. If a boundary condition is applied to a node, no equation is generated for that node because it experiences no translation or rotation. In nonlinear analyses, prescribed displacements can be used in place of boundary conditions when the node needs to be released at some time.

For the herein described model, three different constraints have been applied: circumferential symmetry, extremities and longitudinal symmetry.

The circumferential symmetry forces balloon lateral nodes to remain fixed on circumference radius, fixing a zero displacement along the y-axis, as highlighted in Figure 3.5.

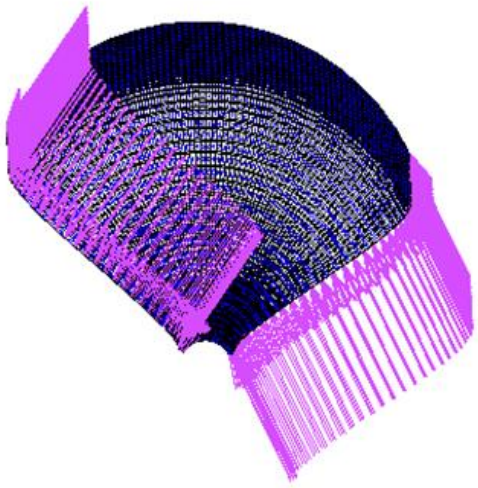

Figure 3.5 Boundary Conditions are depicted as violet arrows around the balloon: lateral nodes are forced to remain fixed on circumference radius under the constraint of circumferential symmetry. This figure has been taken from MSC Marc.

As regards the longitudinal symmetry boundary condition, the nodes belonging to a symmetric plane are required to have zero displacement in the direction normal to the symmetry plane. Finally, distal nodes have been fixed along x-axis and y-axis, allowing the balloon to move only in the radial direction.

To simulate the inflation of the previously described balloon model inside rigid and compliant vessels, loadcases have been added to the analysis.

They are sets of loads and displacements that act on a model at one time. A model can experience different loadcases at different times and each load or displacement can be included in more than one loadcase. On MSC. Marc® software, loadcases can be classified as static or dynamic.

In this particular case, the load is applied to the model by inflating the balloon with a given pressure and it consists of two steps.

In the first step (free inflation phase) a constant internal pressure equal to 0 atm is applied for 5.2 seconds. During this phase, the balloon, which is initially in a tri-folded configuration, is free to regain its original shape inside the vessel.

In the second step, a constantly increasing pressure is imposed on the internal surface of the balloon. This pressure is applied with a constant rate in 10 seconds and its value is varied from 0 to 3 atm.

Both the loadcases have a Constant Time Step equal to 0.005 while the overall number of steps is equal to 1040 in the first case and 2000 in the second one.

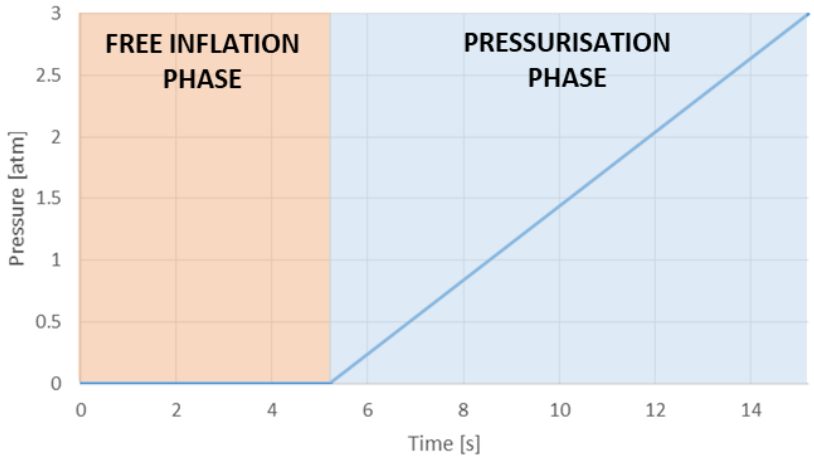

Figure 3.6 MARC Simulations: inflation pressure. Free inflation phase (0 atm) and Pressurisation Phase (ramp from 0 to 3 atm)

In Figure 3.6, a linear increase from 0 atm (vacuum) up to 3 atm is shown. It must be taken into account that, contrary to what happens in reality, in the numerical simulation on MSC. Marc® the environment surrounding the balloon is at 0 atm. Therefore, an inflation from 0 atm up to 3 atm is equivalent to an increase of the intra-balloon pressure from atmospheric condition to 4 atm. During the experimental validation, the inflation process will be performed accordingly.

d. Job Analysis and Solution

In order to correctly simulate the inflation of the balloon, an initial configuration with the balloon tri-folded needed to be recreated.

In clinical practice, in fact, the balloon is prepared for insertion by a series of steps to create three or more folded wings or flaps. The wings are wrapped circumferentially to provide a minimized outer diameter when the balloon is in its deflated state. This particular configuration is shown in Figure 3.7 (B), compared to the fully inflated state depicted on the left side (A).

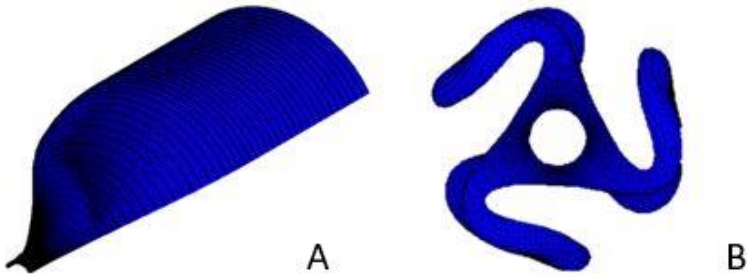

Figure 3.7 In standard clinical practice, the balloon catheter is prepared for insertion by a series of steps to create three or more folded wings or flaps. The wings are wrapped circumferentially (B) in order to provide a minimized outer diameter when the balloon is in its deflated state. In contrast, (A) shows the balloon fully inflated state. This figure has been taken from MSC Marc.

This goal has been achieved by running a preliminary simulation, during which a Pressure Cavity load (ramp from 0 to -1 atm) has been applied. In order to recreate the tri-folded configuration, a vertical force has been applied during the deflation as well. Values of stress, strain and displacement from the last increment (step #514) of the deflation analysis have then been set as initial condition properties in the inflation one. Ignoring this aspect would yield to the erroneous expansion of the balloon.

Several job parameters must be taken into account, as shown in Table 4: initial loads must be set on in defining job parameters and they include both initial conditions properties and boundary conditions.

Contact Control	Segment-To-Segment contact
Cyclic Symmetry	#repetitions = 3; axis of rotation = Z
Loadcase time	15.2 s (1520 steps)
Implicit analysis	Structural static with large strain

Table 4 Job Parameters on MSC Marc

The contact between the BAV Balloon catheter and the annulus has been modeled using the Segment-To-Segment method: it leads to much more accurate simulations, being not mesh sensitive and providing a general method to address contact problems.
The Large Strain structural analysis formulation has been also used for the loading analysis.

Besides, a cyclic symmetry interaction has been defined to model an entire 360° structure using only a single repetitive sector. In this case, the axis of symmetry and the number of sectors that create the full structure must be indicated. This feature can result in a substantial saving of computer time.

In Figure 3.8, a synthetic overview of the Edwards Balloon Numerical Model is shown.

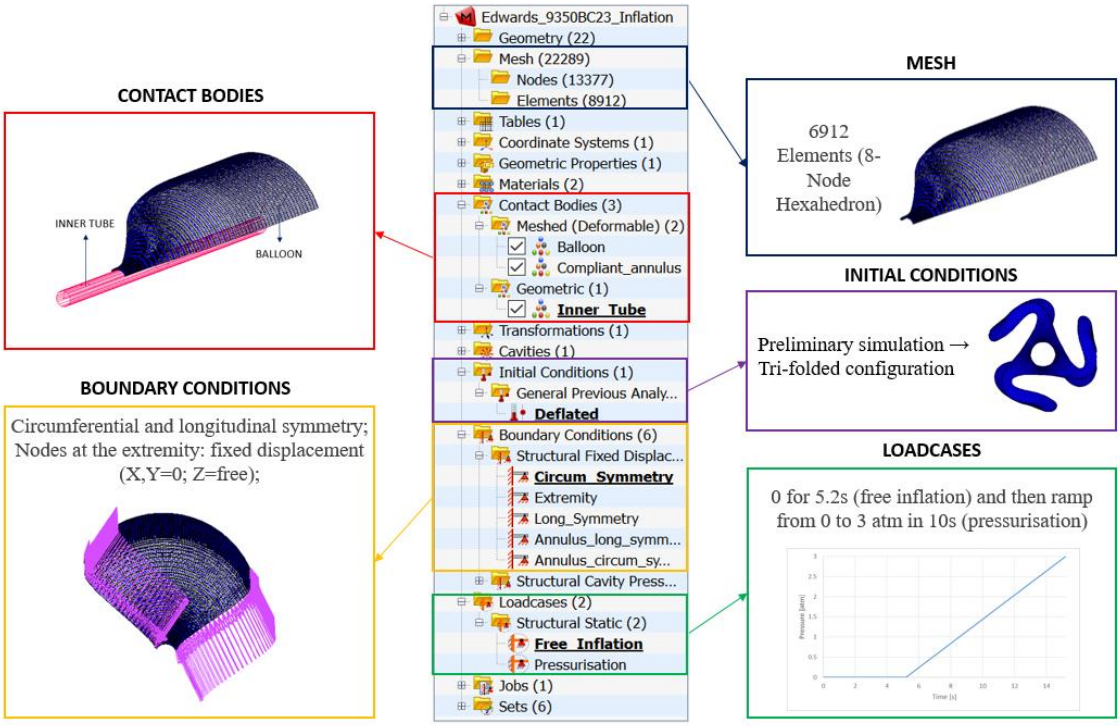

Figure 3.8 MARC Simulations: Overview of Edwards Balloon Numerical Model

While the pre-processing and post-processing phases of the finite element method are interactive and time-consuming for the analyst, the solution is often a batch process and it is demanding of computer resources. The governing equations are assembled into matrix form and are solved numerically. The assembly process depends not only on the type of analysis (i.e. static or dynamic) but also on the model's element types and properties, material properties and boundary conditions.

MSC. Marc® provides a log file, which should be searched for warnings or errors, and which will provide a quantitative measure of how well behaved the numerical procedures were during solution.

3.2 Numerical modelling of phantom vessels

3.2.1 Finite Element Models of Rigid Aortic vessels

FE models of the rigid cylindrical vessels have been firstly implemented and meshed in Abaqus/Standard (Simulia, Inc., Providence, RI, USA) and then they have been transferred to MSC. Marc® for further meshing and finite element analyses. To perform simulations on rigid vessels, six rigid cylinders with different diameters (18 mm, 19 mm, 20 mm, 21 mm, 22 mm, 23 mm) and variable length (1 cm, 2 cm, 3 cm, 4 cm and 5 cm) have been created.

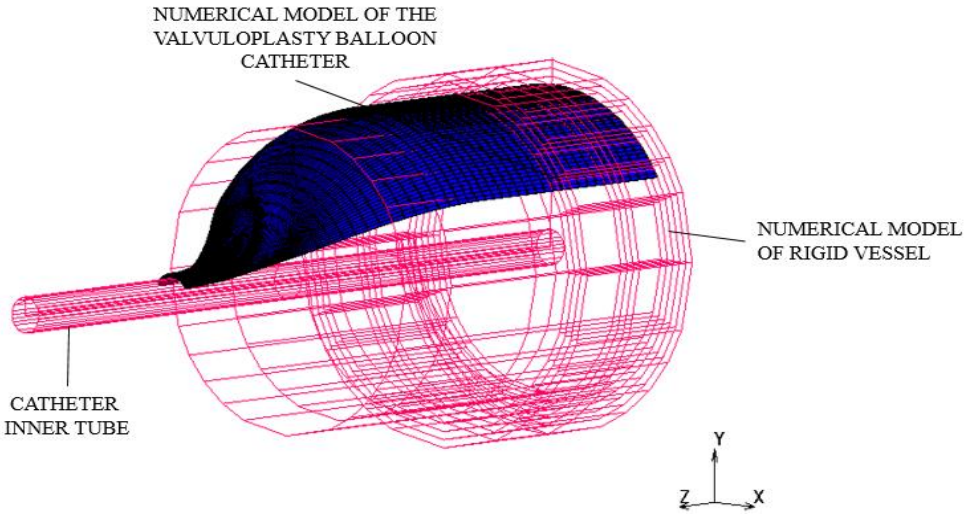

Figure 3.9 Marc Simulations: BAV Balloon catheter has been inflated inside rigid vessels, defined as geometric rigid 3D surfaces

In Figure 3.9, an example of balloon inflation inside a rigid vessel is shown. It has been defined as geometric rigid 3D surface: according to the specific simulation, the diameter of the vessel is varied as well as its length.
Following the same procedure, also 3D elliptical surfaces have been realized.

On the other hand, inflation in circular compliant phantoms is only possible with the 18 mm and 19 mm diameter cylinders, since the diameter of the balloon at atmospheric pressure is equal to 20 mm. In this second case, the effect of length and ellipticity has not been analysed.

3.2.2 Finite Element Models of Compliant Aortic vessels

In previous Sections, the numerical model of the balloon catheter has been described, starting from the real and commercially available device and then moving towards the Finite Element Analysis. Subsequently, computational models of the rigid aortic vessels have been introduced as well, to be able to simulate the inflation of the above-mentioned balloon inside rigid sites of implantation.

The present section describes instead the procedure followed to create rapid-prototyping compliant vessels, which consists of the following main steps:

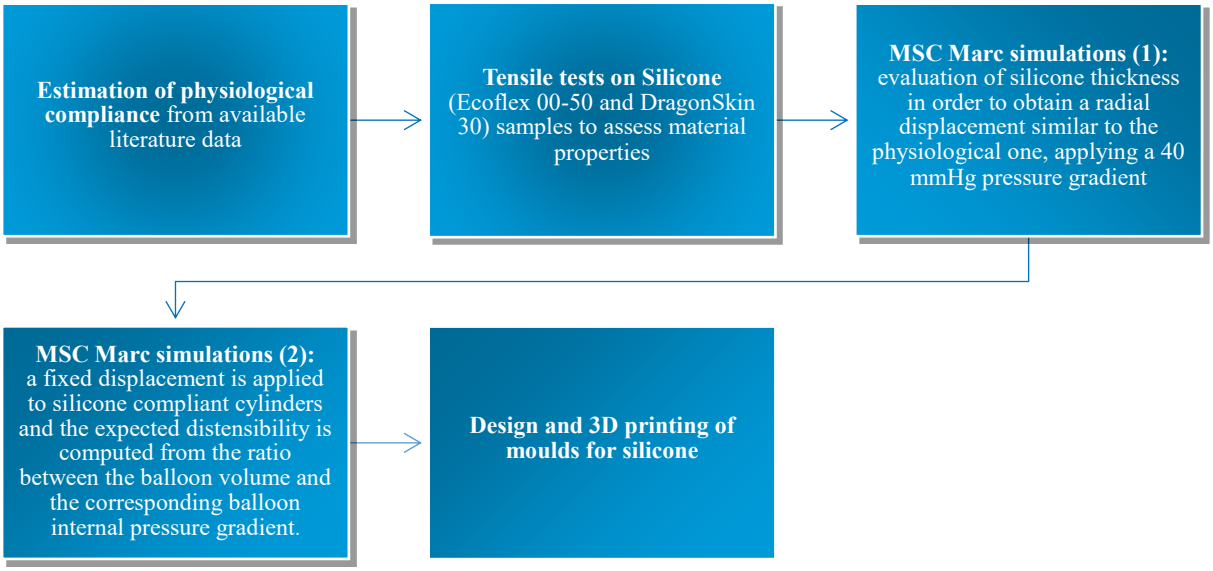

Figure 3.10 Compliant models: procedural steps followed to create Silicone cylinders to simulate compliant aortic vessels both numerically and experimentally

.

The main aim of this procedure is to create cylindrical silicone vessels: their distensibility will be first calculated numerically, following the steps indicated in Figure 3.10, and then it will be retrieved experimentally, by inflating the balloon catheter inside them. In order to make the analysis relevant from a clinical point of view, it has been decided to create silicone vessels with a distensibility as much similar as possible to the physiological one. Therefore, a first assessment of the physiological value is required: this is the reason why the first step of this procedure involves the estimation of physiological compliance from available literature data.

Then, since the herein described compliant vessels will be made of silicone and not of biological tissue, tensile tests have been performed on silicone samples in order to assess the mechanical properties of the material.

The third step of the procedure depicted in Figure 3.10 concerns the evaluation of the required silicone thickness: once, in fact, the silicone has been mechanically tested and the physiological reference value has been estimated, it is necessary to understand which thickness of the material would allow obtaining a distensibility value similar to the physiological one. It is fair to assume that the distensibility associated with a thicker vessel will be lower than the one computed for a thinner one. This is done using MSC Marc: the aim is to find a numerical radial displacement as much similar as possible to the physiological one, setting as output the corresponding thickness of the material and applying a pressure gradient equal to 40 mmHg (physiological gradient obtained as the difference between systolic and diastolic pressure).

At this step, silicone vessels with a compliance similar to the physiological one have been numerically implemented.

However, the balloon catheter will apply to the internal surface of the vessel a pressure equal to 4.5 atm and the material is highly non linear: thus, to compare two values of distensibility, numerical and experimental, associated respectively to two different values of pressure gradient, 40 mmHg and 4.5 atm, would yield to erroneous analysis. Consequently, the distensibility of the silicone vessel corresponding to an internal pressure gradient equal to 4.5 atm has been computed by means of numerical simulations in the fourth step of this procedure.

Finally, the fifth and last step shown in Figure 3.10 concerns the design and 3D-printing of moulds for silicone: a full description of this manufacturing procedure is provided in Section 3.3.4. A detailed description of each step of the procedure is provided in the following paragraphs.

Estimation of physiological compliance from available literature data

While it is generally agreed that the cross-sectional area of the annulus changes significantly during the cardiac cycle, there are conflicting data regarding the amount of cyclical change in the annular perimeter. Moreover, the fact that small changes in perimeter might affect the device selection is still up for debate.

Hamdan et al. [42] suggest that perimeter changes are very small if compared to the variation of the cross-sectional area during the cardiac cycle. In patients with calcified valve, this variation is even negligible.

In this study, carried out in 2015, authors conclude that perimeter should be used to size valves, as it shows minimal variations between systole and diastole, it is not affected by shape changes and it stretches only minimally under physiological pressure.

On the contrary, Blanke et al. [52] claim that perimeter changes between systole and diastole are relevant and, most of all, they could have major implications for device selection in the setting of borderline annuli.

The aortic annulus is often not circular or more precisely is seldom a perfect circle in shape. Therefore, vessels of the same area may have a different circumference depending on the annulus shape. The area-derived diameters will be identical in both cases, leading to the use of an identical prosthesis size, despite the different shape of the annulus. On the contrary, the circumference-derived diameters will be different in both cases, which could possibly lead to the selection of a different prosthesis size [53].

For this reason, as claimed by Murphy et al.[25], a perimeter variation of 3.50% have been considered. Starting from this value, physiological distensibility has been computed as follows.

Being in the physiological range, a minimum pressure of 80 mmHg and a maximum pressure of 120 mmHg have been taken into account, associated respectively to diastole and systole phases. Therefore, the value of ΔP has been set equal to 40 mmHg.

Assuming a deformation in annular perimeter equal to 3.50% and an initial annular diameter of 18 mm, physiological distensibility values result to be equal to 0.0018 $mmHg^{-1}$.

Same distensibility values can be referred also to 19 mm diameter annulus.

Further calculations are shown in Table 5.

	18 mm DIAMETER	19 mm DIAMETER
Initial diameter	18 mm	19 mm
Perimeter variation	3.5%	3.5%
Pressure gradient [mmHg]	40	40
Physiological radial displacement [mm]	0.3150	0.3325
Physiological Distensibility [$mmHg^{-1}$]	0.0018	0.0018

Table 5 Values of physiological radial displacement and physiological compliance according to literature. Silicone distensibility will be computed accordingly

In order to create compliant vessels with physiological values of distensibility, the same ΔP (40 mmHg) will be applied to them through numerical simulations, varying their thickness until a radial displacement similar to the one computed above will be reached.

Tensile tests on Silicone samples to assess material properties

In this work, two formulations of silicone rubber have been used from Smooth-On, Inc (Easton, Pennsylvania): Dragon Skin 30 and Ecoflex 00-50.

Ecoflex is a versatile and easy-to-use silicone, which is cured at room temperature with negligible shrinkage. It is based on Smooth-On0s Dragon Skin technology and it is currently available in four different hardnesses: 00-10, 00-20. 00-30 and 00-50.

On the other hand, DragonSkin silicone is available in Shore 10A, 20A and 30A. Table 6 provides a technical overview of the materials herein described.

	Pot Life	Cure Time	Tensile Strength	Elongation at Break %	Shrinkage
Ecoflex 00-50	18 min	3 hours	315 psi	980%	<.001 in./in.
DragonSkin 30	45 min	16 hours	500 psi	364%	<.001 in./in.

Table 6 Ecoflex 00-50 and DragonSkin 30 Technical Overview

Figure 3.11 depicts the Zwick Roellr Z 5.0 (Zwick GmbH & Co., Ulm, Germany) uniaxial tensile test machine used to perform stretching tests on 10 silicone dumbbell specimens of each material.

Figure 3.11 The Zwick Roellr Z 5.0 tensile machine used for the tensile tests on silicone samples (left) and (right) a dumb bell shaped sample during the experiment

This machine is made of a portable, single-column load frame specially designed for mechanical testing of a small sample and with low loads. The maximum test load is 5.0 kN, and the maximum crosshead speed is 600 mm/min, with a travel resolution of 0.0399 µm.
Test data are acquired by the control system in real-time, with a frequency of 500 Hz. The control system and the testing machine have been controlled via a PC and TestXpert software, which allows for multiple post-processing functions.
At the beginning of each test, the dumb-bells extremities were fixed into screw grips. After zeroing the force, each sample has been pulled until yielding, and force and displacement have been recorded. The specimens prepared according to DIN EN ISO 6892-1 have been tested until failure in the test machine and corresponding stress-strain data have been collected (Figure 3.12).
These curves have been used to define the material model in FEA.
Following the BS ISO 37:2005, tests have been performed under displacement control with a constant displacement rate of 20 mm/min.
Stress-strain curves corresponding to Ecoflex 00-50 and Dragon Skin 30 presented in Figure 3.12 are the mean curves of ten different experiments conducted under identical loading

conditions. Each curve shows the mean value and the associated standard deviation, computed for discrete points corresponding to every 0.1 % of the strain range.

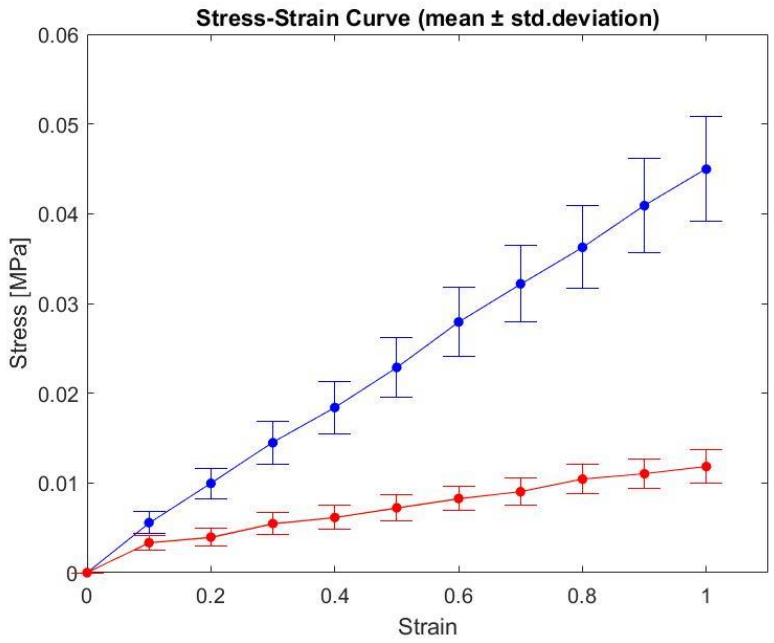

Figure 3.12 Ecoflex 00-50 (red) and Dragon Skin 30 (blue) Stress-Strain curves: mean ± standard deviation is shown.

As clear from Figure 3.12, silicone is an isotropic hyperelastic material that has a nonlinear stress-strain relationship. It is also incompressible, resulting in the Poisson's ratio (ν) being equal to 0.5. This material experiences large strains and deformations under normal loads while hysteresis and softening occur during cyclic loading.

The nonlinear stress-strain relationship and incompressibility of rubber cause difficulties to model it numerically. There are different material models that can be used for the analysis of rubber in MSC. Marc®. These include the Mooney, Ogden, Arruba Boyce, Gent, Bergstrom Boyce, Marlow and Anisotropic hyperelastic material models.
These models are used in conjunction with experimental results of silicone to determine the model parameters and eventually determine the best model for the specific application.
In this work, many different models have been evaluated for both materials, based on data fitting goodness, stability and extrapolation capability.

In particular, fitting goodness has been estimated computing the error between the real experimental curve and the numerical evaluation. In this case, the least squares error is given by Eq. 8:

$$LSE^R = \sum_{i}^{Ndata} \left(1 - \frac{\sigma_{CALC,i}}{\sigma_{MEASURED,i}}\right)^2 \qquad \text{Eq. 8}$$

where LSE^R represents the relative least squares error between the real experimental curve and the numerical evaluation, σ_{CALC} stands for the fitted engineering stress and $\sigma_{MEASURED}$ is the experimentally retrieved engineering stress.

Stability has been extrapolated by looking at the sign of the computed coefficients: for example, it is known that Ogden coefficients come in pairs. If each modulus and relative exponent have the same sign, then stability is guaranteed. If instead the modulus is positive and its corresponding exponent is negative (or vice versa) then the material model might be unstable. On the other hand, Mooney form models with all positive coefficients guarantee stability in all modes, for all strain. The simpler the material model, the higher probability it will be stable over a wider strain range.

Finally, MSC. Marc® provides an extrapolation feature, in order to extend the strain range over which the model's response is plotted, so that the user is able to see if the chosen model behaves properly even for larger values of strain. In this case, extrapolation capability of the model in correspondence to 200% and 300% of strain has been evaluated.

Consequently, a second order Ogden form has been chosen, as it provides the best fitting for the experimental data, shown in Figure 3.13, and as it has been used previously to describe non-linear stress-strain relationships of various arterial tissues [41], [42].

The form of strain energy for the Ogden model in MSC. Marc® is given by the following equation:

$$W_{deviatoric}^{ogden} = \sum_{k=1}^{N} \frac{\mu_k}{\alpha_k}\left(\lambda_1^{\alpha_k} + \lambda_2^{\alpha_k} + \lambda_3^{\alpha_k} - 3\right) \qquad \text{Eq. 9}$$

where $\lambda_1^{\alpha_k}$ are the deviatoric stretch ratios while μ_k and α_k are the material constants obtained from the curve fitting of experimental data.

The model gives a good correlation with test data in simple tension up to 700% [54]. It accommodates non-constant shear modulus and slightly compressible material behaviour.

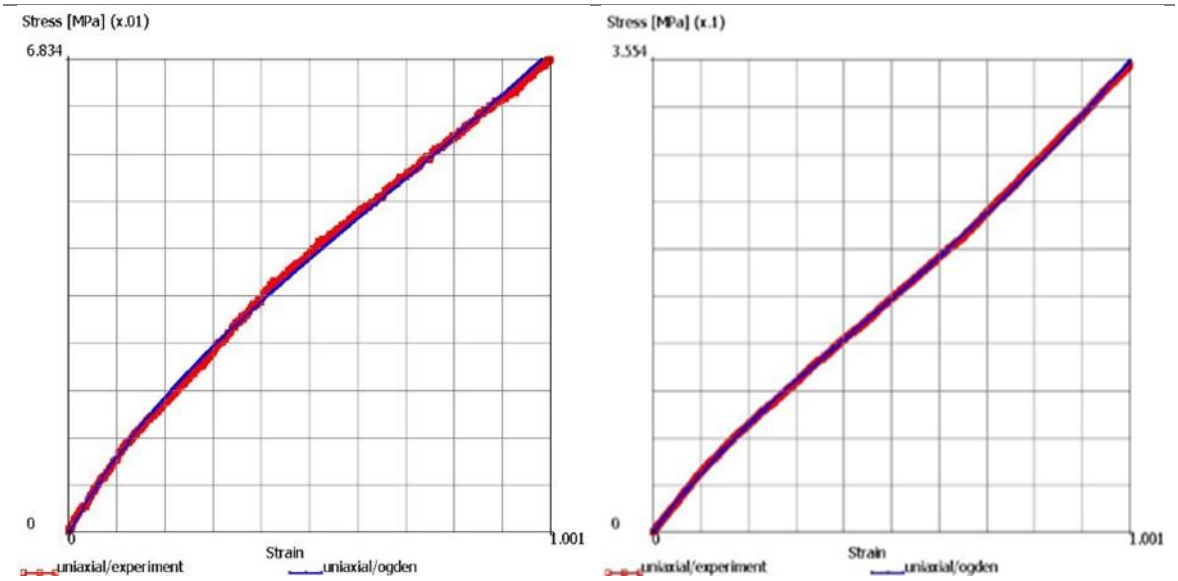

Figure 3.13 Ogden (2) hyperelastic model fitting Ecoflex 00-50 Stress-Strain experimental curve on the left and Dragonskin 30 on the right. Red lines correspond to experimental curve while blue solid line represents the hyperelastic model fitting.

In Figure 3.13, red lines represent experimental stress-strain relationships obtained by means of tensile tests previously described in this Section while blue lines correspond to their hyperelastic model fitting.

On the left, the stress-strain curve related to Ecoflex 00-50 is depicted and the associated parameters for the 2nd-order Ogden form, calibrated by MSC. Marc® from the experimental stress-strain results of uniaxial tensile tests previously described, are reported in Table 7.

	Moduli	**Exponents**
1	0.00852787	3.47424
2	-0.0370591	-1.41816

Table 7 Ecoflex 00-50 Ogden (2): Moduli and Exponents parameters computed by MSC. Marc®

On the right-hand side of Figure 3.13, the stress-strain curve related to DragonSkin 30 is depicted: in this case, the associated parameters for the 2nd-order Ogden form are given in Table 8.

	Moduli	Exponents
1	0.0327427	4.04193
2	-0.171945	-1.1512

Table 8 DragonSkin 30 - Ogden (2): Moduli and Exponents parameters computed by MSC. Marc®

MSC Marc simulations (1):

At this stage, both silicone materials could have been used to model and manufacture compliant vessels. However, in the following lines, it will be explained why DragonSkin 30 has been chosen.

As done for the balloon model, which represents only one-sixth of the overall cross-sectional area, only a portion of the compliant vessel has been modeled as well. Cylindrical models have been initially created and defined on Abaqus: as shown in Figure 3.14, C3D20R quadratic brick element has been used for discretization and the final mesh resulted in 4000 elements. Because of the localised nature of the contact stresses and strains around the contact zone, a mesh refinement has been implemented along the radial direction. It is important to get sufficient mesh refinement not only because of the accuracy it brings, but more especially because an overly coarse mesh at the contact zone will lead to bad contact detection by the program. This will, in turn, lead to the penetration of the contacting objects into each other due to failed detection of contact.
The mesh refinement is shown in Figure 3.14.

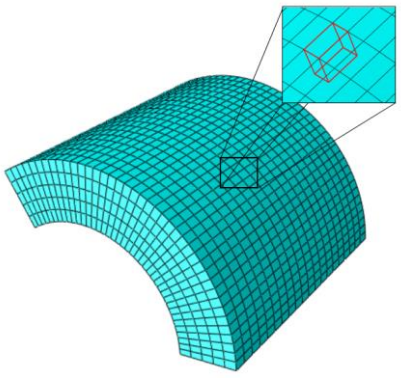

Figure 3.14 Finite Element Model of the aortic vessel meshed on Abaqus: C3D20R quadratic mesh type elements have been used. The final mesh results in 4000 elements. Figure has been taken from Abaqus.

The meshed object has been then imported into MSC. Marc®, where mesh elements have been changed to 8-node hexahedral bricks of type 7. Ogden isotropic hyperelastic behaviour has been assigned to elements.

The vessel has been modeled as an isotropic homogeneous monolayer hollow tube, having an internal diameter of respectively 18 mm and 19 mm.

Only these two sizes can be used to evaluate compliance since the balloon nominal diameter is equal to 20 mm: as previously said, to measure vessel compliance is important to avoid balloon stretching, being therefore able to neglect its material properties during the computation of distensibility.

Boundary conditions have been set as well, since they significantly influence the model response under a pressure load. The first boundary condition is the one concerning the circular section surfaces: the displacement in the axial direction has been blocked, since the vessel is not supposed to shift in this direction. Moreover, all the rotational displacements have been set equal to zero, as shown on the left side of Figure 3.15. The second boundary condition, depicted on the right side of Figure 3.15, regards instead the transversal section of the vessel. Consequentially, the only degree of freedom of the model results to be the one in the radial direction, as the vessel needs to expand when a pressure load is applied on the inside.

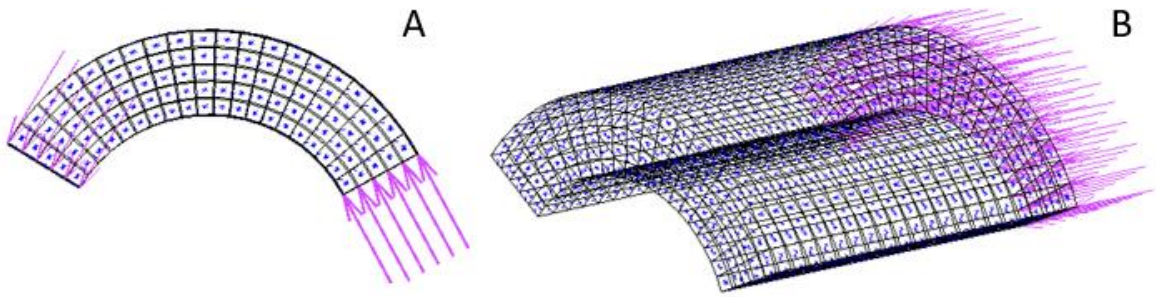

Figure 3.15 MARC Simulations: Boundary conditions applied to the compliant cylinder to prevent it from moving during the inflation process. (A) frontal view showing how rotational displacements have been set equal to zero. (B) balloon model longitudinal view showing how axial displacement has been prevented. This figure has been taken from MSC Marc; violet arrows represent boundary conditions while the blue meshed object corresponds to the modeled portion of the compliant vessel.

After the definition of geometry, materials and boundary conditions, a pressure load of 40 mmHg has been applied in order to compute the material thickness associated to a radial displacement similar to the physiological one. In other words, silicone thickness has been repeatedly modified until the radial displacement of the 18 mm cylinder internal surface, consequent to an internal pressure load of 40 mmHg, has been found equal to 0.3150 mm (see Table 5).

Similarly, the thickness of 19 mm diameter cylinder has been changed until a radial displacement of 0.3325 mm has been achieved.

In Table 9, physiological radial displacement, associated Ecoflex 00-50/DragonSkin30 thicknesses and corresponding numerical radial displacement are reported.

	18 mm diameter	**19 mm diameter**
Physiological radial displacement (see Table 5)	0.3150 mm	0.3325 mm
Computed Ecoflex thickness	35 mm	32 mm
Computed DragonSkin thickness	5 mm	4.5 mm
Numerical radial displacement (DragonSkin 30)	0.2880 mm	0.3295 mm

Table 9 Marc Numerical Simulations: physiological radial displacement, associated Ecoflex 00-50/DragonSkin30 thicknesses and corresponding numerical radial displacement are shown in the table.

As previously said, the aim was to find a numerical radial displacement as much similar as possible to the physiological one, setting as output the corresponding thickness of the material. As clear from Table 9, Ecoflex 00-50 results to be softer than DragonSkin30 and 5 mm of Ecoflex 50 would lead to a radial displacement much greater than the desired one. In fact, in order to gain the right displacement, Ecoflex 00-50 should be in the order of 3 to 4 cm while DragonSkin30 shows the right property with a thickness of 5 mm. For this reason, DragonSkin30 has been chosen as compliant vessels manufacturing material, allowing to have a thickness which is enough thick to avoid ruptures but at the same time is also enough thin to avoid material waste.

Numerically computed radial displacements result to be slightly smaller if compared to the physiological ones: this means that resulting compliant vessels will be a little stiffer than physiological vessels. However, since the purpose of this procedure is to create rapid-

prototyping compliant vessels with a distensibility within the physiological range and not to match the exact value extracted from literature, this overestimation will not be a problem for experimental analysis.

MSC Marc simulations (2):

As previously said, being the silicone material highly nonlinear, the silicone distensibility associated with the pressure applied during the balloon inflation (~4.5 atm) need to be computed. This distensibility will be, in fact, slightly different from the one associated with a physiological pressure gradient (40 mmHg). Distensibility has been defined as the ratio between the change in volume corresponding to a given change of pressure: while the change in volume is already known, the pressure gradient must be determined. Thus, this latter value has been set as the main outcome of the fourth step of this procedure.

In order to exclusively compute the compliance of the silicone material, being able to neglect the one associated with the balloon material, the final volume of the compliant cylinder has been calculated as follows:

$$V_F = \pi\left(\frac{20\ \text{mm}}{2}\right)^2 * 25\ \text{mm} = 7853.98\ \text{mm}^3 \qquad \text{Eq. 10}$$

where 20 mm is the non-stretched diameter of the balloon catheter (i.e. the diameter at atmospheric pressure) while 25 mm is the longitudinal length of the finite element model of the vessel, as previously stated. 20 mm diameter has been considered because, after this stage, the balloon would start to stretch, showing a compliance that would become indistinguishable from the one associated with the silicone material. The initial volume has been computed likewise, considering a diameter equal to 18 mm and 19 mm respectively.
Thus, the change in volume is known and equal to the difference between the final volume and the initial volume of the silicone vessel.
Starting from these values, a linear cavity mass load has been applied to the internal surface of the balloon, as shown in Figure 3.16.
Values of final volume and initial volume previously mentioned have been simply converted to final mass and initial mass of the vessel multiplying by the material density (1e-009).

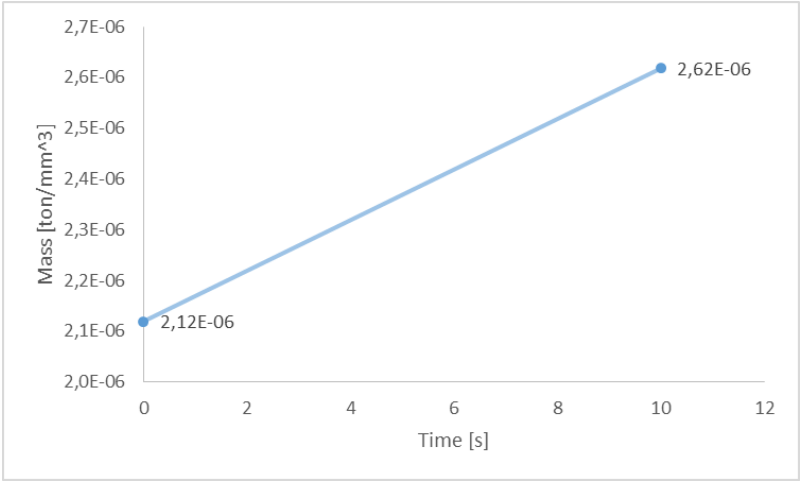

Figure 3.16 MSC Marc Numerical Simulations: Linear cavity mass load from M_1=2.12e-006 tonn/mm^3 to M_2=2.62e-006 tonn/mm^3

Thus, the initial mass (M_1) has been obtained multiplying the material density (1e-009) and the initial volume (V_1). V_1, in turn, has been computed by applying a pressure load equal to zero and by estimating the obtained cavity volume. Similarly, the final mass (M_2) has been derived from the final volume (V_F), assessed according to Eq. 10.

Mass load is indicated as ton/mm^3: in MSC. Marc®, the pressure is expressed in MPa and, for the sake of consistency, the mass should be expressed in ton and the volume is indicated in mm^3.

To model the boundaries of the intra-balloon cavity, cavity surface elements (elements types 171-174) have been used. They are for volume calculation purposes only and do not contribute to the stiffness equations of the model.

Cavity Surface Elements are shown in Figure 3.17.

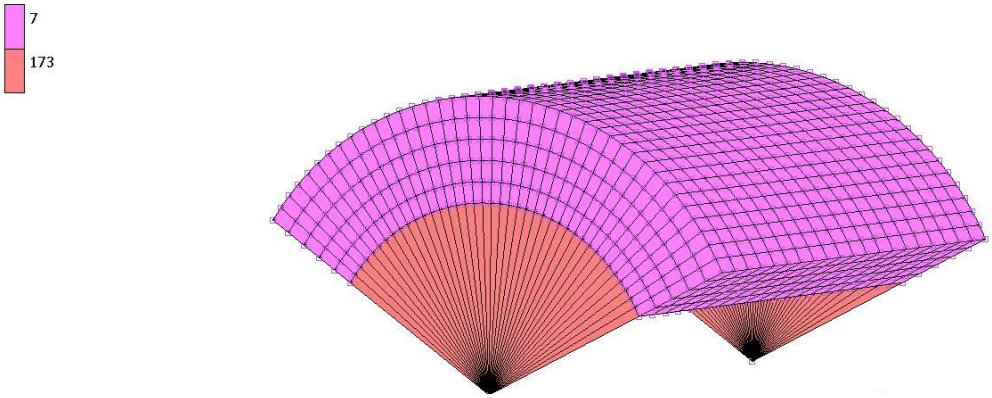

Figure 3.17 Cavity Surface Elements (173 type) have been placed on the sides of the numerical model of silicone vessel to define the cavity for volume calculation purpose

Design and 3D printing of PLA moulds

Silicone-based cylindrical vessels have been produced pouring silicone material inside 3D printed PLA moulds. The .stl file has been created through Solidworks and a complete overview of the design is given in Appendix A.

A detailed description of this manufacturing process is given in Section 3.3, where the overall experimental setup is presented.

3.3 Experimental Setup

This section described the experimental setup used to validate numerical simulations. The system should be able to measure the changing over time of volume injected into the cavity and intra-balloon pressure, displaying them in terms of pressure-volume (P-V) curves.

3.3.1 Hardware components

By means of the controlled experimental setup herein described, compliance and diameter of each vessel, rigid or compliant, are quantified by simultaneously recording the internal pressure and corresponding inflated volume of a non-compliant high-pressure Edwards valvuloplasty balloon (Edwards Lifesciences LLC, Irvine, CA, USA).

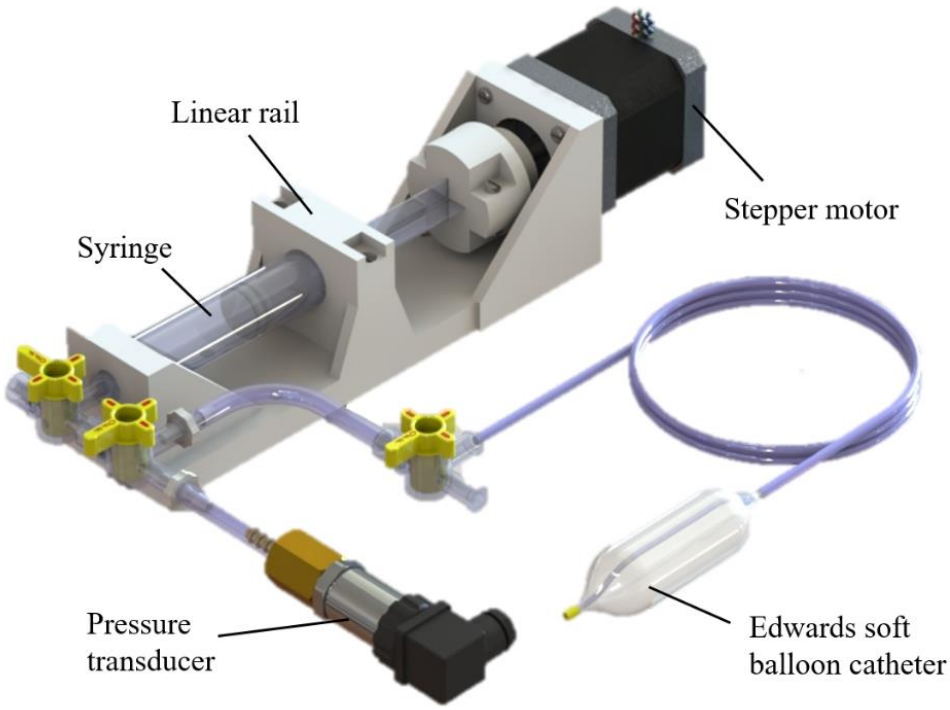

Figure 3.18 Robotic Balloon catheter: Experimental setup

As shown in Figure 3.18, a 10 ml syringe pump, filled with water, is used to inflate the balloon at a constant flow rate of 0.076 mL/s. The above-mentioned syringe pump is made of a Terumo syringe, mounted on a plastic linear rail, and a stepper motor.

The plastic support has been 3D printed for this specific purpose: it allows, in fact, the syringe to remain fixed and stable as the stepper motor moves back and forth. The diameter of the syringe plunger is 15.8 mm, with a surface area of about 196.1 mm^2. Since 1000 mm^3 are equal to 1 mL of water, the plunger has to move by approximately 5.1 mm to inject 1 mL of fluid. Moreover, the syringe is able to support up to 4 atm of pressure, which is the maximum pressure required to fully inflate the balloon, according to literature.

Water is taken from a reservoir located above with respect to the overall experimental setup and it is connected to the syringe pump through a plastic tube and a 4-way luer stopcock.

The syringe plunger is moved through a non-captive stepper motor with an anti-rotation mechanism, whose main specifications are reported in Table 10.

Threaded Shaft	Steps per revolution	Rated Current [A]	Holding Torque [mN*m]	Detent Torque [mN*m]	Inductance per phase [mH]
Tr8*8	200	0.4	460	25	45

Table 10 17HS5001-100D8 non-captive stepper motor with an anti-rotation mechanism for the threaded shaft. Main specifications

Linear actuators are generally classified as captive, non-captive or external. A captive actuator is able to convert rotary to linear motion via an integrated nut and leadscrew; as the name suggests, the latter is held captive within the motor housing welded to a stainless steel spline arrangement. The captive actuator is designed for shorter strokes and it provides precise linear movement. On the other hand, as shown in Figure 3.19, in a non-captive linear actuator the screw does pass to the back of the motor.

Figure 3.19 Captive, non-captive and external linear actuators

This kind of motor has no reasonable stroke limits; however, an assembly that will not rotate is needed in order to allow the leadscrew to extend and retract without rotating. Finally, in the external configuration, the linear actuator uses a leadscrew and nut combination that extends out from the motor. The nut traversing back and forth as the leadscrew turns creates linear motion. The piston of the syringe pump must move back and forth without rotating, therefore a captive linear actuator or a non-captive linear actuator with an anti-rotation mechanism are two acceptable and equivalent solutions.

Stepper motors have a step angle. A full 360° circle divided by the step angle gives the number of steps per revolution. In this case, 200 steps per revolution are equivalent to 1.8° per full step, which is a common step size rating. Besides, the Tr8x8 screw is characterised by a linear displacement of 8 mm per revolution, which is equal to 0.04 mm per full step.

Since the motor is powered by 12 V and 0.4 A, the maximum speed can be calculated as follows:

$$\text{Max Speed} = \frac{\text{V}}{2\text{LI}_{\text{max}}\text{S}} = \frac{12}{2 * 0.045 * 0.4 * 200} \approx 1.67 \ [\frac{\text{rev}}{\text{s}}] \qquad \text{Eq. 11}$$

Such speed can be reduced by introducing a time delay function between steps within the controller. The chosen time delay is equal to 25 ms (5 s per revolution), reducing the speed from 1.67 $\frac{rev}{s}$ to 0.18 $\frac{rev}{s}$.

Due to the high values of pressure that can be reached while inflating the balloon, a PXM319-007A10V (Omega Engineering Inc., Stamford, CT, USA) absolute pressure transducer is employed.

Pressure sensors using diaphragm technology measure the difference in pressure between the two sides of the diaphragm. Pressure applied to the transducer produces a deflection of the diaphragm, which introduces strain to the gages. The strain will produce an electrical resistance change proportional to the pressure. Depending on the reference pressure, the terms ‘Absolute’ is used when the reference is vacuum; ‘Gauge’ is used where the reference is atmospheric pressure; and ‘Differential’ is used where the sensor has two ports for the measurement of two different pressures.

The full-scale range of the sensor is 0-7 bar and the output voltage goes from 0V up to 10V. Since the pressure transducer is connected to Arduino Uno Board, the sensor output has been decreased from 10V to 6.81V using a voltage divider, as shown in Figure 3.20. The voltage divider is made of two resistances, R_1=4.7 kΩ and R_2=10 kΩ. The voltage source (V_{IN}) is applied to the series of these two resistors and the voltage drop across R_2 is called V_{OUT}.

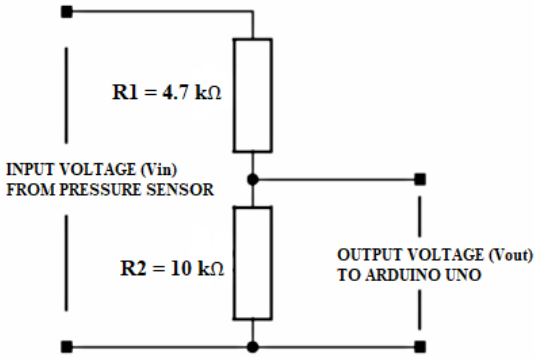

Figure 3.20 Voltage divider used to connect pressure transducer to Arduino Uno Board

This has been done in order to be able to estimate a pressure range from 0 atm up to 4.5 atm. Each test is going to be repeated five times for every vessel, in order to ensure the repeatability and reproducibility of the data. Values of pressure are acquired after each motor step, which corresponds to 0.0078 mL of injected fluid. Given the intrinsic variability of experimental tests, it is fair to assume that each test will not have the same number of samples: in fact, the maximum pressure (4 atm) could correspond to slightly different injected volumes.

However, to be able to compute the mean curve of these tests, having the same number of samples is compulsory. It has been therefore decided to measure pressures up to 4.5 atm, so that the number of samples at least up to 4 atm is going to be the same. Then, values from 4 atm to 4.5 atm have been simply neglected and the mean values curve has been computed on a range which goes from 0 to 4 atm.

With the electrical configuration shown in Figure 3.20, when the intra-balloon pressure is equal to 5 atm the output voltage of the divider is going to be equal to 4.86 V. 5V is the maximum voltage value that the Arduino Uno Board is able to measure.

The pressure sensor has been calibrated and the calibration curve is given below: the curve has an offset of 0.012 V. Consequently, the sensor sensitivity, defined as the ratio between the output signal and the measured property, is equal to 1.428 V/bar.

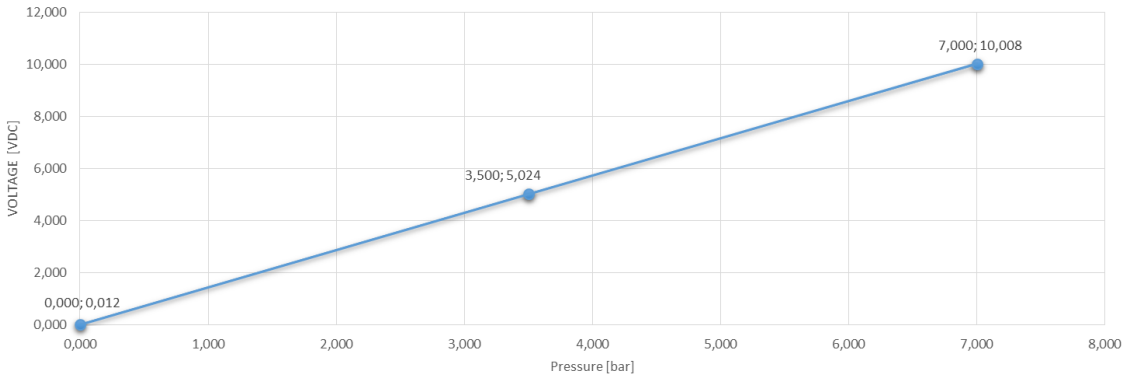

Figure 3.21 Pressure sensor calibration curve

A 4-way luer stopcock, positioned at the inflation lumen of the balloon Y-connector, provides access to both the syringe and the pressure transducer. An additional stopcock is used to attach the valvuloplasty balloon to the system: besides, this connector allows the removal of the air in the balloon through a syringe. The above-mentioned components are connected through stiff Tygon® medical tubing, in order to minimize the compliance of the overall system. Moreover, they have been securely nailed to a steel platform whose CAD design is reported in Appendix A. In this way, all components remain fixed and exactly aligned during the inflation experiment.

The pressure sensor and the stepper motor are connected to Arduino Uno board through analog and digital pins respectively. Arduino Uno is a microcontroller board based on the ATmega328P. It has 14 digital input/output pins, 6 analog inputs, a 16 MHz quartz crystal, a USB connection, a power jack, an ICSP header and a reset button.
Moreover, a Velleman Motor and Power shield have been used to easily control motor direction and speed, as shown in Figure 3.22. It also allows to power the linear actuator with a separate power supply of up to 12V.

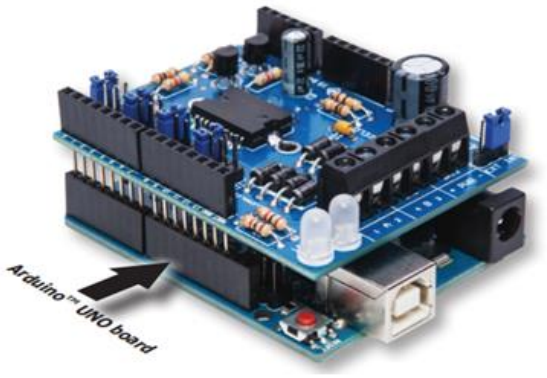

Figure 3.22 Arduino Uno Board and Velleman motor shield

By using this motor shield, it is possible to choose between an external or internal power supply. Furthermore, it is based on the dual full-bridge driver L298P and it has been provided with a stackable design: the shield can in fact be stacked with other shields in order to control different motors. Further specifications are presented in the following table:

Power Supply	Max. Current	Outputs
From 7 to 46 VDC	2A	Up to 2 DC motors or 1 bipolar stepper motor

Table 11 Velleman Motor shield specifications

3.3.2 Experimental Protocol

During the experimental tests, the BAV balloon catheter has been filled with water through the previously described experimental setup. In order for the balloon to be stable and suspended horizontally during the test, thus avoiding geodetical effects, it has been placed on 3D-printed nylon supports; however, it has been chosen to not secure the catheter to the supports with metallic screwed cups, in order to avoid additional constraints. These would have invalidated the overall procedure, bringing additional pressures.
All the air is initially removed from both the system and the balloon using an additional Terumo syringe, so that the balloon is able to recover its tri-folded initial configuration.

After the preparation of the setup, experimental tests are carried out by manually typing on the user interface the amount of fluid to be injected into the balloon and the motor speed. Pressure and volume data are continuously recorded during the whole experiment and they are plotted real-time to generate the corresponding P-V relationships. Given the small dimension of the syringe, two different inflation cycles are performed.
Each test has been repeated five times for every cylinder, in order to ensure the repeatability and reproducibility of the data. Mean curve and standard deviation of experimental tests are computed as well.

3.3.3 Firmware and user interface

First, a communication protocol named StandardFirmata has been uploaded on Arduino Uno. This is a general purpose sketch which allows communicating with microcontrollers from software on a host computer, containing different libraries for many different software. Several Firmata client libraries have been implemented in a variety of popular programming languages and Processing is one of them. Thus, a sketch developed in Processing controls the overall acquisition. Processing is an open source computer programming language and integrated development environment (IDE), which provides a simple and straightforward graphics. The experimental setup, in fact, needs an application capable of receiving a flux of data from the pressure sensor, plotting them on the screen in real-time, and a simple interface to control the stepper motor and the syringe pump.

What has been realised is presented in Figure 3.23.

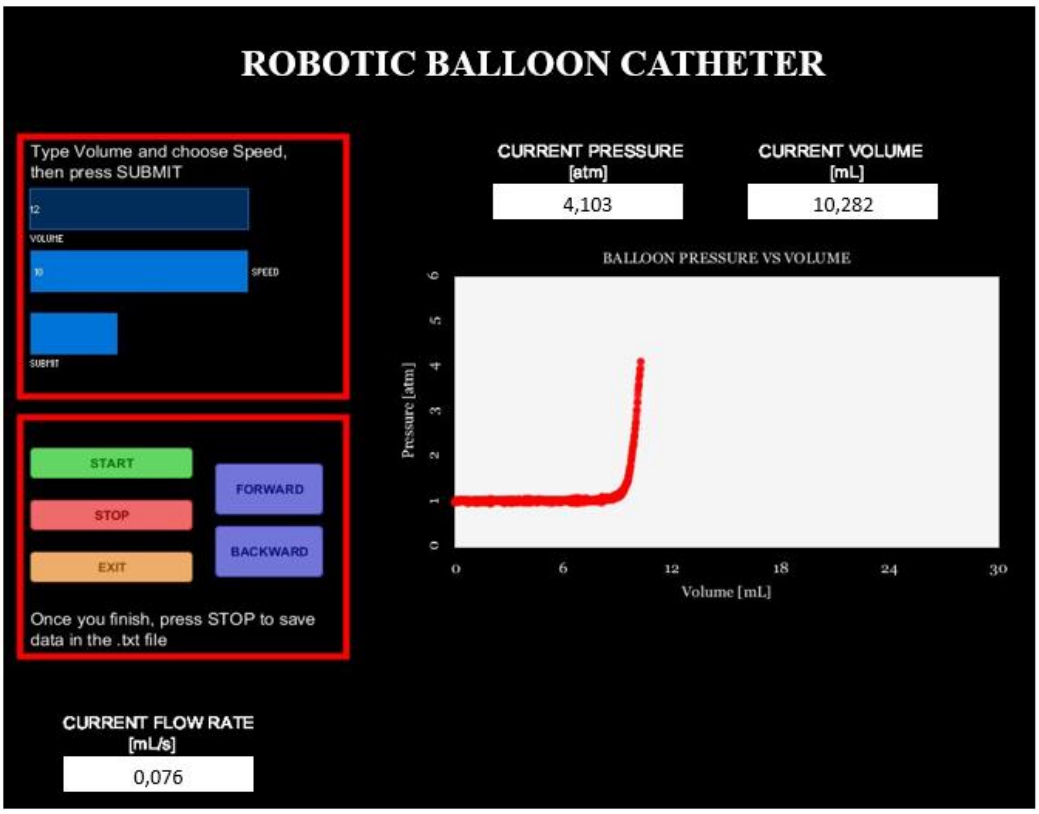

Figure 3.23 User interface built on Processing. The user can type the desired volume and the desired speed on the left part of the screen and move the stepper motor using GUI buttons (Start, Stop and Exit). On the right side of the screen, the P-V curve is plotted real-time and values of Pressure, Volume and Flow Rate are displayed. This figure has been taken from Processing.

The user interface is divided into two main parts: the first one allows the user to decide the amount of fluid to be injected into the system as well as the motor speed, displayed in terms of steps delay. In this specific case, 100 corresponds to a delay of 100 ms and therefore a lower velocity if compared to the one obtained with a 10 ms delay.

The delay refers, in fact, to the time passing between two consecutive motor steps. Moreover, energizing the electromagnets in different directions, it is possible to drive the motor backwards or forwards.

On the other hand, the right side of the screen shows real-time values of pressure, volume and flow rate. The P-V curve is plotted on the display.

The code has been written using Processing standard functions and adding some additional libraries such as "*cc.arduino*" to receive data from Arduino Uno Board, "*grafica*" and "*controlP5*" to create and handle graphic elements.

Two Tabs make this code:

1. "**P-V Plot**" Tab includes additional libraries, defines and sets useful variables and it is made of Setup() and Draw() functions. While the statements in the Setup() function execute once when the program begins, the code inside the Draw() function runs continuously with a default frequency of 60 fps from top to bottom until the program is stopped.
   In the image below, workflow of the main instructions executed in both Setup() and Draw() phases is presented.

The Setup() phase is used to create the GUI, to configure pins to behave as inputs or outputs and to set P-V plot in terms of axis, title and labels. Then, in the Draw() function, the program receives typed volume and motor speed, saving these values into two variables. After each motor step, pressure data and inflated volume are acquired, saved and plotted real-time on the graphical user interface.

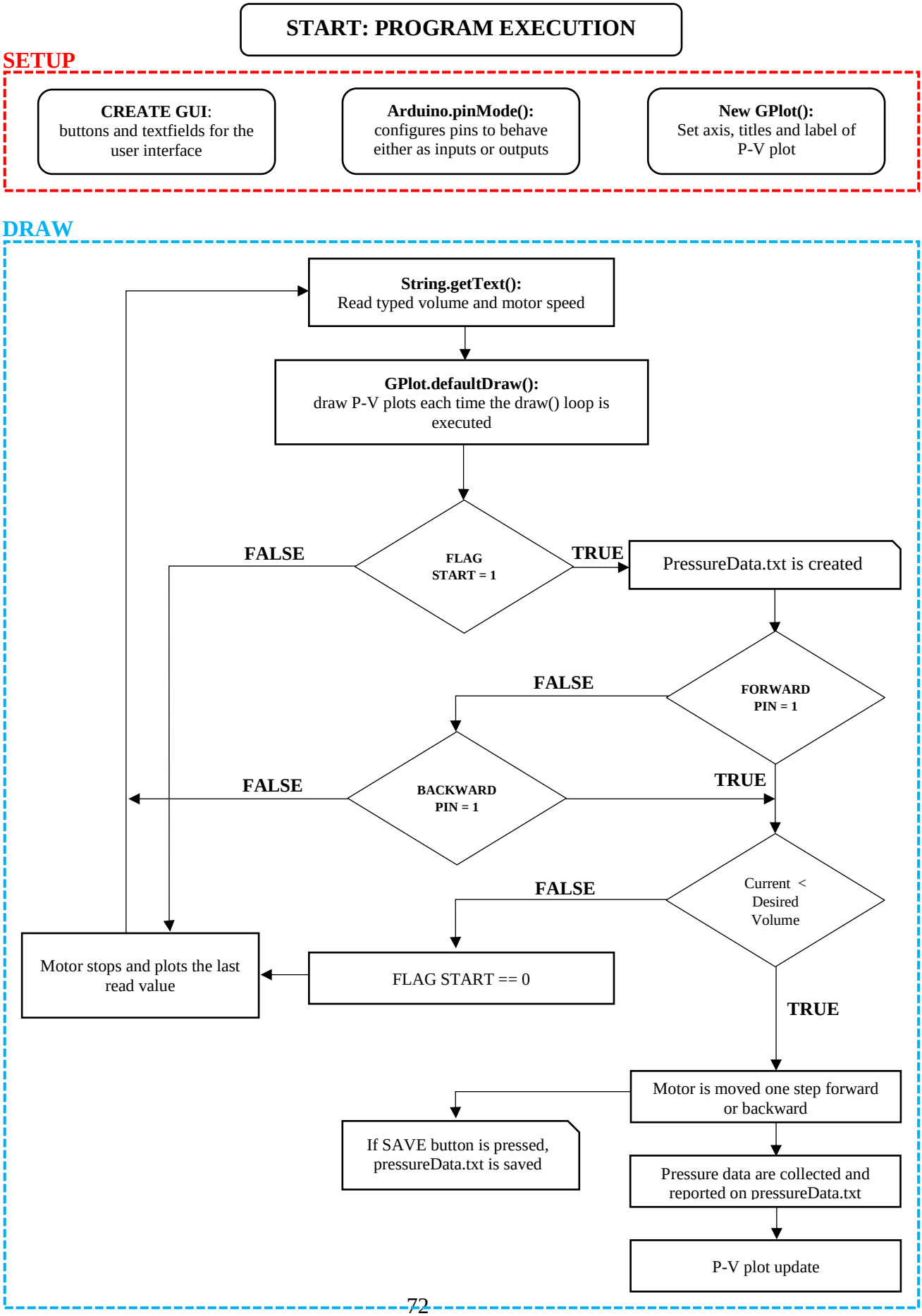
START: PROGRAM EXECUTION
SETUP
CREATE GUI:
buttons and textfields for the user interface
Arduino.pinMode():
configures pins to behave either as inputs or outputs
New GPlot():
Set axis, titles and label of P-V plot
DRAW
String.getText():
Read typed volume and motor speed
GPlot.defaultDraw():
draw P-V plots each time the draw() loop is executed
FLAG START = 1
FALSE
TRUE
PressureData.txt is created
FORWARD PIN = 1
FALSE
TRUE
BACKWARD PIN = 1
FALSE
Current < Desired Volume
FALSE
TRUE
Motor stops and plots the last read value
FLAG START == 0
Motor is moved one step forward or backward
If SAVE button is pressed, pressureData.txt is saved
Pressure data are collected and reported on pressureData.txt
P-V plot update

The inflated volume is computed as follows:

$$V = V_0 + \frac{S * 0.04\ mm}{5.1\ mm} \qquad \text{Eq. 12}$$

where S is the number of motor steps, V_0 represents initial balloon volume, 0.04 mm corresponds to the linear shift/step and 5.1 mm is the plunger longitudinal displacement to inject 1 mL of water.

2. "**GUI**" Tab is mainly auto-generated thanks to dedicated Processing toolbox. It includes buttons creation and functions used to deal with click-events.

Pseudocode is shown in Figure 3.24.

PSEUDOCODE

```
SETUP
Define variables and constants
Set input/output pin modes
Create user interface

DRAW
if (START BUTTON is pressed) {
    if (desired volume > current volume) {
        Motor moves back or forth
        Upload user interface with current values of pressure and volume
        Save values into a .txt file
        if (SAVE BUTTON is pressed) {
            .txt file is saved and closed
        end
    } else {
        Motor switches off
    end
end
```

Figure 3.24 PseudoCode of the user interface built using Processing software

3.3.4 Phantom models of rigid and compliant aortic vessels

Twelve cylindrical and elliptical samples, whose details are listed above, have been created by using a CNC (computer numerical control) machine, in order to have high precision and accuracy.

As shown in Figure 3.25, six cylindrical hollows have been manufactured to simulate circular rigid vessels. The diameter range is 18 mm – 23 mm while the length can be varied thanks to the presence of seven Poly(methyl methacrylate) (PMMA) slabs. The central slab has a thickness of 2 cm, which, according to literature, is the physiological length of the aortic annulus. Additional slices have been added to the central one in order to have a maximum length of 5 cm, which would cover the overall cylindrical length of the balloon catheter. Complete CAD Design is provided in appendix A.

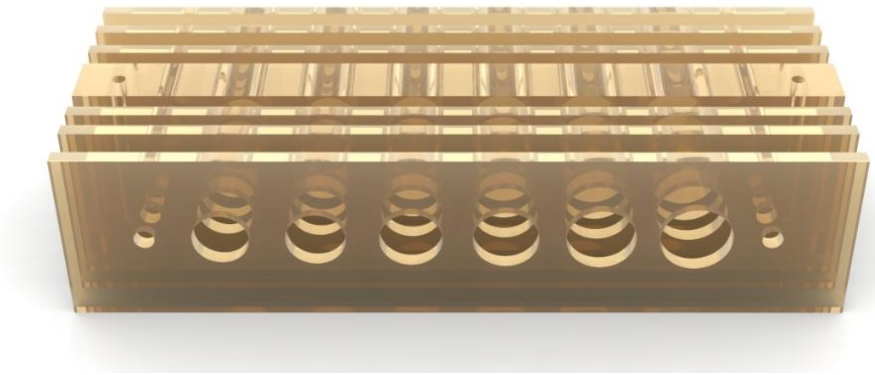

Figure 3.25 Six rigid cylinders used to test the balloon inflation inside the rigid material. They are made of seven different PMMA slabs in order to be able to test the influence of annular length

PMMA slabs are aligned through two longitudinal screws and the overall parallelepiped is anchored to the steel platform thanks to two vertical M6 screws, as shown in Figure 3.30. Due to manufacturing technique, the diameter of these vessels is slightly smaller (0.2 mm less) than the nominal one.

Regarding elliptical shapes, samples have been sized considering a mean aortic annulus ratio (i.e. short axis diameter/long axis diameter) of 0.82 mm (0.81±0.06 mm) [52] and a perimeter equal to the previously analysed circumferences. This could have been done considering the area of previously analysed vessels as well; however, results would not have changed much.

Figure 3.26 shows the balloon catheter inflated inside rigid phantoms of the aortic annulus.

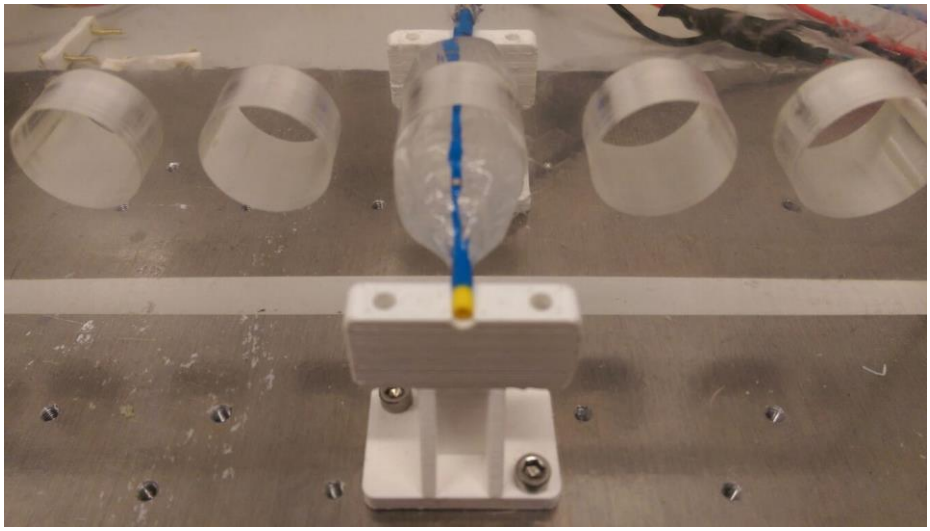

Figure 3.26 Vessel geometry assessment: the BAV balloon catheter is inflated inside rigid PMMA phantom vessels. The diameter range is 18 mm – 23 mm, increasing from left to right, while the length can be varied thanks to the presence of seven Poly(methyl methacrylate) (PMMA) slabs, within a range of 2 cm – 5 cm.

Besides, as shown in Figure 3.26, two holders have been specifically designed for this purpose: they have been 3D printed in polylactic acid (PLA) with a rapid prototyping 3D printer. The .stl file has been obtained by means of the CAD software Solidworks.
During the experiments, the position of the holders remains fixed on the steel platform in order to maintain them exactly aligned. This system allows the balloon to remain fixed as well and suspended during the whole inflation phase, in order to ensure that the shape variation is only due to the inflation process. However, holder cups have not been fixed on the top of the holders, so that the balloon can slightly adjust during the inflation process. An excessive balloon constraint would have produced additional pressure loads inside the cavity, invalidating the overall procedure.

On the other hand, as regards silicone-based compliant vessels, two different moulds have been created and successively nailed together with a tolerance of 0.2 mm. As shown in Figure 3.27, the internal cylinder has a diameter equal to 18 mm ($D_{INT}{}^{1}$) while the external one is a cylindrical casing, whose internal diameter has been set equal to 28 mm ($D_{INT}{}^{2}$) with a thickness equal to 5 mm (T_{casing}).

The difference between the internal diameter of the external casing ($D_{INT}{}^{2}$) and the diameter of the internal cylinder ($D_{INT}{}^{1}$) is equal to the thickness of the compliant vessel (T_{vessel}), whose extent has been determined with the procedure described in details in Section 3.2.2.

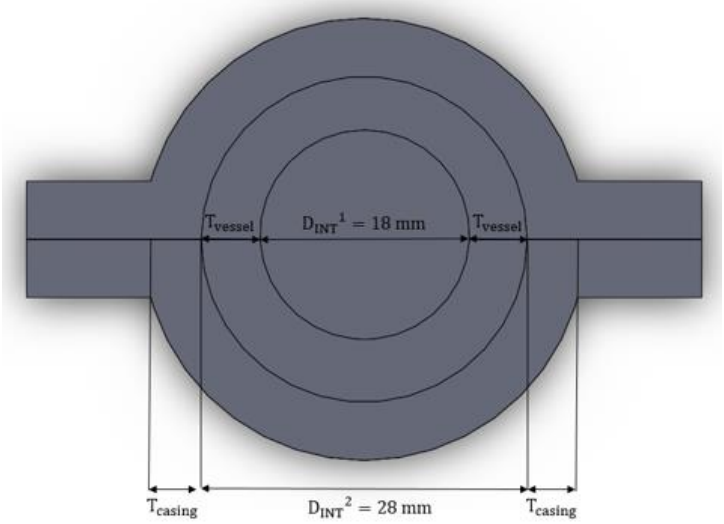

Figure 3.27 PLA moulds for Ecoflex material: 3D model

The length of the mould has been set equal to the length of the balloon cylindrical section (5 cm). Even in this case, complete CAD Design is provided in appendix A.
The same procedure has been followed to realise a Ø19 mm compliant mould: in this case, according to Table 9, DragonSkin30 thickness should be equal to 4.5 mm.

An example of PLA mould is shown in Figure 3.28.

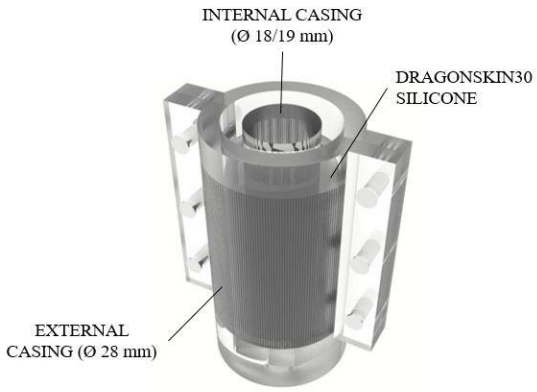

Figure 3.28 3D rendering of PLA mould for silicone: Ø18/19 mm internal cylinder and Ø28 mm external casing. DragonSkin30 is poured inside and allowed to cure at room temperature.

Ecoflex 00-50 and DragonSkin 30 come in two parts: parts A and B. To achieve moulding, both parts of the silicone material are mixed in equal quantity (by weight or volume), poured into the 3D printed moulds and allowed to cure at room temperature.

Prior to that, the compound has been placed inside a vacuum machine for 2-3 minutes to eliminate any entrapped air. To facilitate easy removal of the cured silicone from the mould, a release agent (Ease Release 200) is applied to the mould surface prior to pouring the liquid silicone into it.

Figure 3.29 shows the BAV balloon catheter inflated inside a Ø18 mm silicone-based compliant vessel.

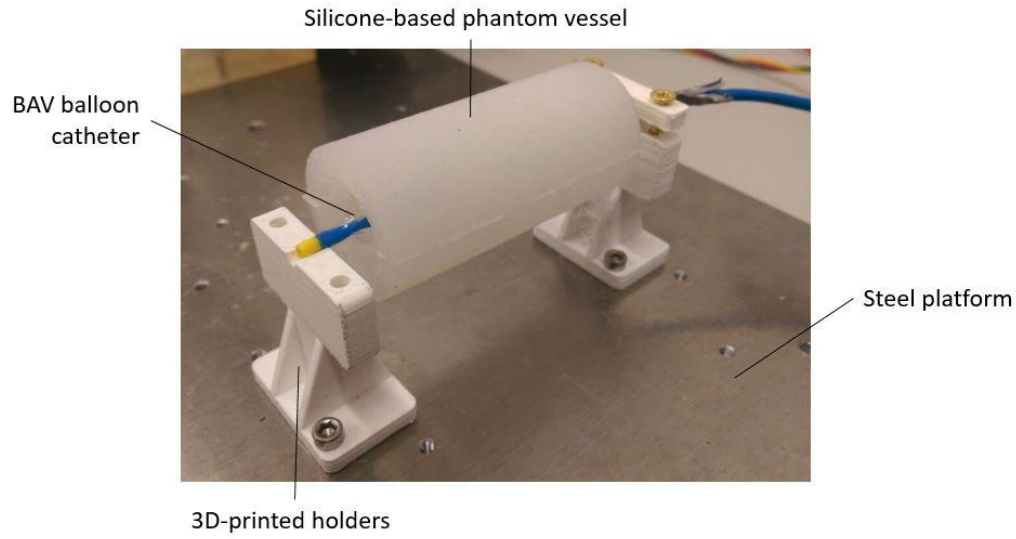

Figure 3.29 Compliance assessment: BAV balloon catheter is gently secured within two 3D-printed holders and it is then inflated inside a silicone-based phantom vessel, whose length has been fixed equal to the length of the balloon cylindrical section (5 cm). The overall setup is anchored on a steel platform, shown in the figure as well.

In Figure 3.30, the real system anchored on the platform (1) is shown. Phantom models of the aortic annulus, both circular rigid (2) and compliant (3), are depicted on the left side of the image. Moving then from left to right, the linear rail (4), the absolute pressure sensor (5), voltage divider (6) and Arduino board (7) are shown as well. The BAV balloon catheter (8) is inflated within 3D-printed holders (9) inside rigid phantoms of elliptical aortic vessels (10).

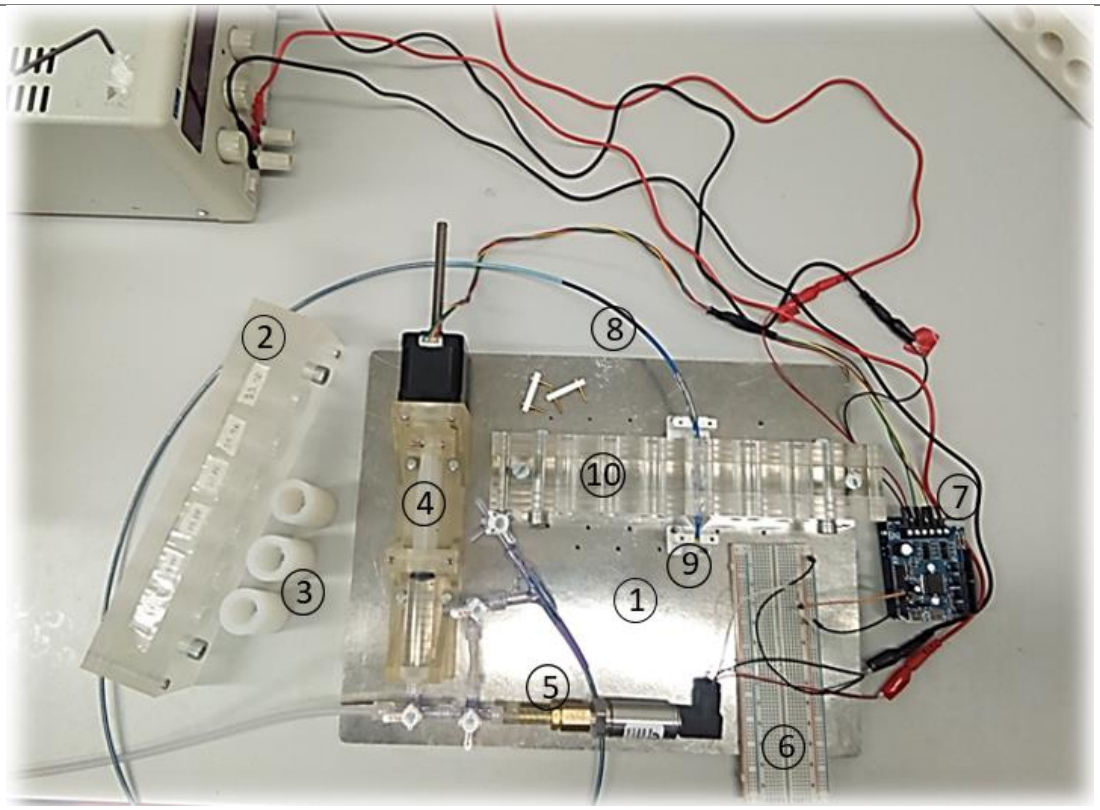

Figure 3.30 Real Experimental Setup: (1) steel platform; (2) circular rigid models of aortic vessels and (3) compliant phantoms of aortic vessels; (4) linear rail; (5) absolute pressure sensor; (6) voltage divider; (7) Arduino Uno board; (8) BAV balloon catheter; (9) holders; (10) rigid phantoms of elliptical aortic vessels.

3.4 Summary

This chapter has described the numerical and experimental methods used in this investigation. Regarding the estimation of vessel geometry, a numerical model of the BAV Balloon Catheter has been created and it has been inflated inside rigid annuli. A specifically designed mechatronic system has been introduced to show how computational results are going to be validated: it comprises electronic components such as a stepper motor, a pressure sensor and an Arduino Uno board, but also CAD-designed objects, like a linear rail, a steel platform and PLA 3D-printed supports. Finally, these different components interact with each other thanks to a user-friendly Processing interface. For the purpose of compliance assessment, additional simulations have been done considering a non-linear hyperelastic material. DragonSkin 30 has been selected as the most suitable material to manufacture compliant vessels. In the following pages, a summary of the main numerical and experimental findings is provided and discussed.

Chapter 4

DATA COLLECTION, RESULTS AND DISCUSSION

In this Chapter, results of both numerical and experimental analysis described in Chapter 3 are reported. Specifically, the first part of this section focuses on the assessment of phantom vessel geometry while the second one concerns the analysis of silicone-based vessels distensibility. A twofold approach characterises each section: the first part focuses in fact on numerical simulations while the second and last part covers bench tests results. Experimental and numerical findings are presented through P-V curves: below each graph, in addition to findings description, a brief discussion of the results is provided. Mean and standard deviation of experimental tests are presented as well.

Finally, Section 4.3 provides a strategy to automatically retrieve annular dimensions from the previously described results.

4.1 Estimation of Vessel Geometry

This section focuses on the analysis of vessel geometry: the first part (Section 4.1.1) describes numerical results while the second and last part (Section 4.1.2) provides experimental findings. Results concerning the following tests, both experimental and numerical, will be presented:

- Balloon is inflated inside rigid circular vessels with fixed length (5 cm) and different diameters (from 18 mm to 23 mm)
- Balloon is inflated inside Ø18 mm vessel with variable length (from 5 cm to 2 cm)
- Balloon is inflated inside rigid circular vessels with fixed length (2 cm) and different diameters (from 18 mm to 23 mm)
- Balloon is inflated inside rigid elliptical vessels with fixed length (2 cm) and different diameters (from 18 mm to 23 mm)

The first test has been performed to assess whether or not the balloon is able to detect different annular diameters. The second one has been carried out in order to establish a correlation between changes in annular length and P-V curves. The third test has been done in order to assess whether or not the balloon is able to detect different annular diameters even in the case of reduced length (L=2 cm). Finally, the fourth and last test has been introduced to understand if the balloon catheter is able to detect the shape of the annulus. Below each graph, in addition to findings description, a brief discussion of the results is provided.

4.1.1 Numerical Results

Regarding rigid vessels, different combinations have been evaluated, taking into account the influence of multiple parameters such as annulus diameter, annulus length and annular ellipticity.

Effect of annular dimension

The numerical model of the balloon catheter has been inflated inside vessels with different diameters (18 mm, 19 mm, 20 mm, 21 mm, 22 mm and 23 mm) and fixed length (5 cm). Figure 4.1 shows an example of numerical inflation of the balloon catheter inside rigid

vessels having a diameter equal to 18 mm and 21 mm respectively. The main outcomes of these simulations, shown in terms of P-V curves, are depicted in Figure 4.2.

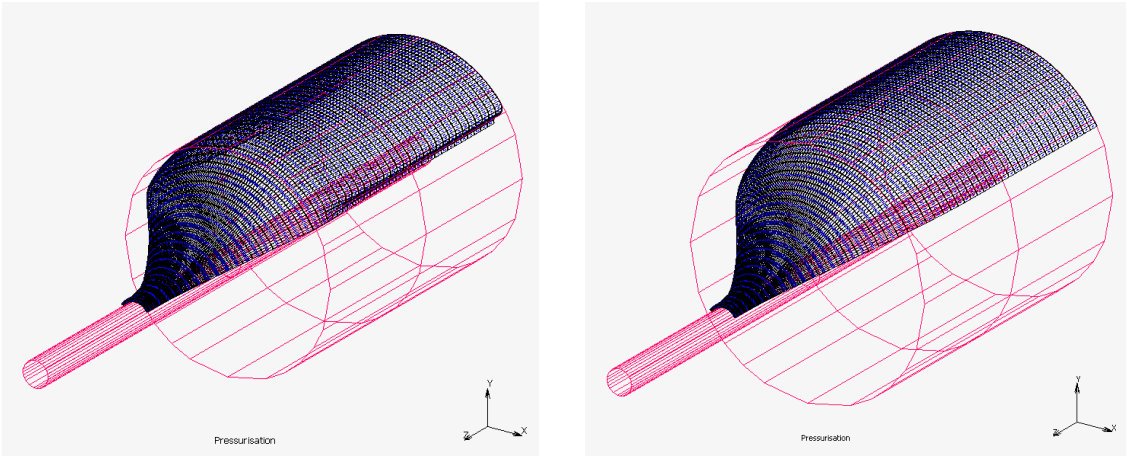

Figure 4.1 Example of numerical inflation of the balloon catheter inside rigid vessels having a diameter equal to 18 mm and 21 mm respectively. Looking at the upper surface of the balloon catheter, it can be seen that in the first case the balloon touches the walls prior to achieve a fully unfolded configuration. This does not happen in the second case, being the vessel diameter greater than the balloon diameter at atmospheric pressure. This figure has been taken from MSC Marc.

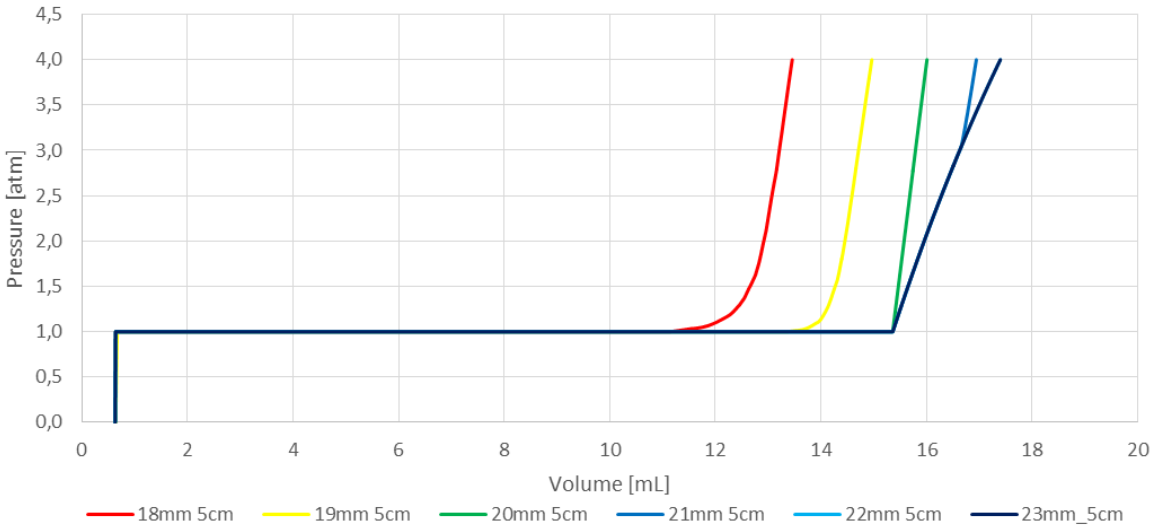

Figure 4.2 Balloon inflation inside six different vessels having different diameters and a fixed length (5 cm).

From the data in Figure 4.2, it is clear that P-V curves can be divided into two main parts: the first one regards the free-inflation phase, during which the balloon simply regains its natural configuration from its initial tri-folded state. The free-inflation phase is characterised

by a constant pressure equal to the atmospheric one (1 atm), while the final amount of volume injected varied accordingly to the dimension of the balloon, as expected. In particular, smaller diameters show a pressure increase which is prior to the one associated with greater annuli.

On the other hand, the second part of these curves is marked by a sudden increase of pressure in correspondence to different volumes. This pressure rise is caused by the contact between the balloon and the vessel walls: the rigid walls of the annulus, in fact, prevent the balloon from expanding while a growing amount of fluid is injected into the cavity.
However, the same pressure escalation is observed even when the external diameter is equal to 23 mm: this could seem counterintuitive since, as previously said, the balloon diameter at atmospheric pressure is equal to 20 mm. However, when the intra-balloon pressure overcomes the atmospheric pressure, the balloon material starts to stretch. This determines an increase in pressure, which is smoother than the one observed in smaller rigid diameters, but is still clearly visible.

The switchover between the free-inflation phase and the pressurisation stage varies depending on the annulus dimension: the smaller the annulus the smoother the transition. Inside smaller annuli, in fact, the balloon does not have the opportunity to completely unfold, as shown in Figure 4.1. Consequently, remaining folds delay the rapid increase of pressure, acting as mechanical cushions and causing a knee in the curve, whose extent decreases as the diameter becomes bigger. This is the first physical parameter that could be used to distinguish different curves and different annuli.

The curves for Ø22mm and Ø23 mm overlap because, according to numerical simulations, the balloon never reaches the annular walls (non-tensioned balloon diameter is 20mm) during pressurisation. Furthermore, even Ø21 mm diameter curve is partially overlaid to the previous ones. However, contrarily to what happens for greater annuli, in this latter case the balloon slightly touches the walls during pressurisation. Consequently, the slope starts to change when the intra-balloon pressure reaches a value equal to more or less 3 atm.
For Ø20 mm curve, the balloon touches the walls exactly at the end of free inflation, while for diameters < 20mm, the contact happens during the free inflation phase. Moreover, from the graph it is clear that the slope of the curves related to Ø18, Ø19, Ø20 and Ø21 is very similar above 3 atm, where it could be considered almost linear.

Inflating a Ø23 mm balloon inside a Ø23 mm gives the same results of a free inflation of the balloon. Therefore, Ø23 mm and free inflation curves are perfectly equivalent. The slope of these latter curves can be considered approximately linear, even if, according to the following calculations, the relationship between volume and pressure appears to be quadratic:

$$\begin{cases} V = \frac{\pi L}{4}\left[D_f\right]^2 \\ \sigma = E\varepsilon \\ \sigma_r = \frac{pd}{2t} \\ D_f = D_i(1+\varepsilon) \end{cases} \quad \rightarrow \quad V = \frac{\pi L}{4}\left[D_i\left(1+\frac{pd}{2tE}\right)\right]^2 \qquad \text{Eq. 13}$$

The system shown in Eq. 13 consists of four equations: the first one expresses the final volume of the cylinder, whose diameter is retrieved by the initial one according to the fourth and last equation. The second equation expresses the Hooke's law while the third one is Eq. 5, mentioned in Section 3.1 speaking of balloon radial stress.

In conclusion, these results suggest that to have an effective annulus estimation, it is of particular importance to oversize the balloon catheter. If the nominal diameter of the device is smaller than the vessel, it will not be able to discriminate different annular dimensions. Moreover, the previously described findings indicate that it should be possible to extract meaningful information from P-V data, to univocally identify diameters ≤ 21mm.

In the next steps, it will be investigated whether that holds even when more variables like annular length, cross-sectional shape and compliance are added.

Length effect on P-V Curves

A change in the annular length is supposed to affect smaller diameters more, therefore the impact of annular length has been assessed on eight vessels with different length (5 cm, 4 cm, 3.5 cm, 3 cm, 2.5 cm, 2 cm, 1.5 cm and 1 cm) and a Ø18mm diameter, as shown in Figure 4.3. Thanks to numerical simulations, even intermediate thickness (i.e. 3.5 cm, 2.5 cm and 1.5 cm) have been considered.

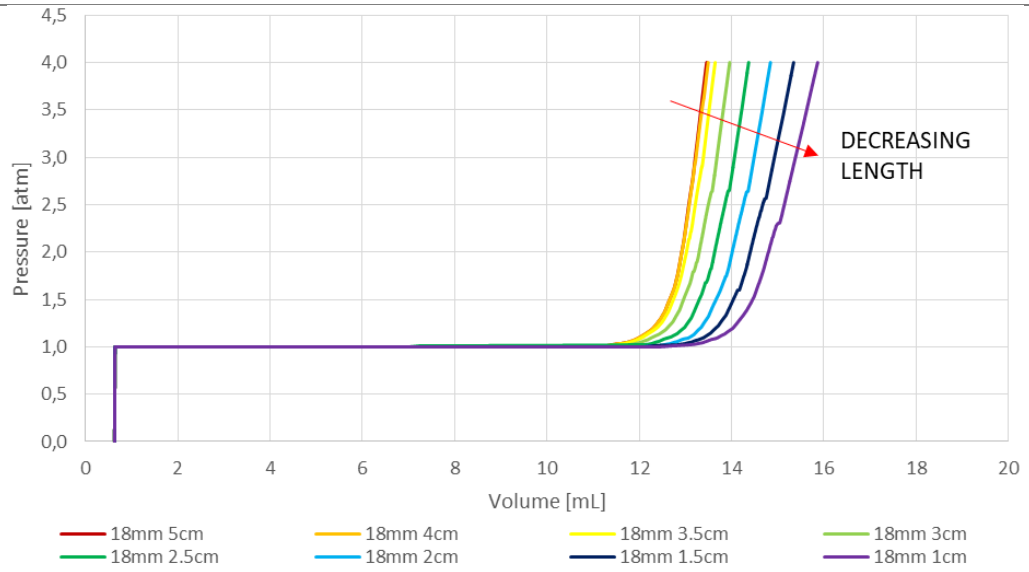

Figure 4.3 Eight different curves showing the impact of annular length on the same vessel (18 mm diameter).

Curves for 5 cm and 4 cm nearly overlap, which is consistent with the length of the cylindrical part of the balloon catheter (4 cm). A shorter vessel results to slightly reduce the slope of all the P-V curves during the pressurisation phase. Moreover, it shifts to the right the P-V curves associated with diameters smaller than the non-tensioned diameter of the balloon, as shown in Figure 4.4.

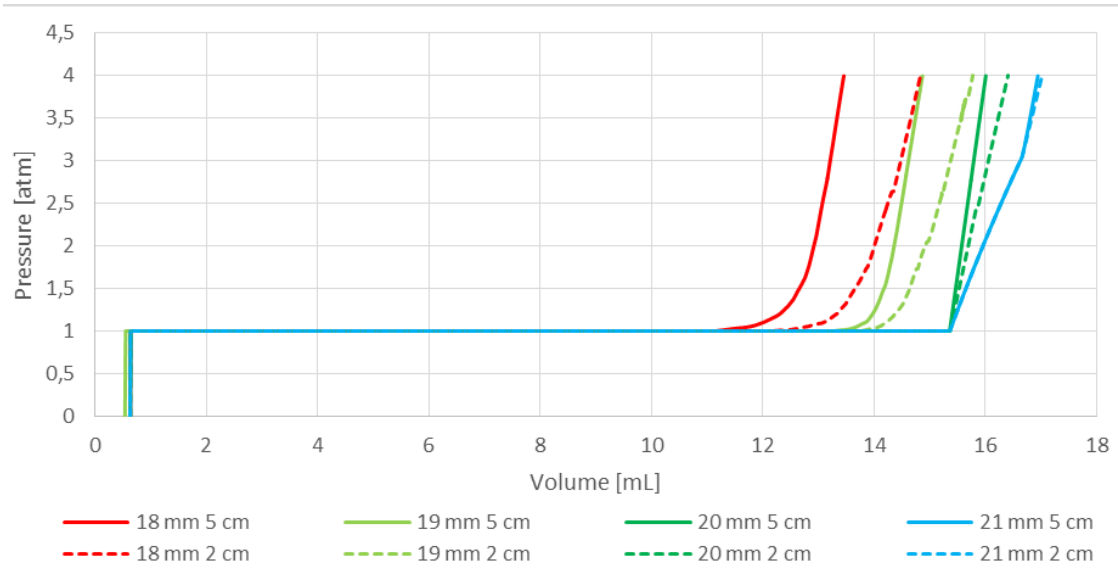

Figure 4.4 Effect of annular length: dot lines represent four different diameters (18 mm, 19 mm, 20 mm, 21 mm) having a length equal to 2 cm. Solid lines depict instead diameters with a length of 5 cm. From this image, it is clear that a length decrease results to shift to the right the P-V curves associated with diameters smaller than the non-tensioned diameter of the balloon.

As clear from Figure 4.4, even in the case of 2 cm length, it is still possible to univocally identify a diameter-length combination, for diameters ≤ 21mm, by simply looking at the P-V curves. Furthermore, it is fair to assume that the curves for 3 cm and 4 cm are bounded by the ones associated with 5 cm and 2 cm.

Figure 4.5 shows an example of numerical inflation of the balloon catheter inside rigid vessels having a diameter equal to 18 mm and a length equal to 5 cm and 2 cm respectively. In the first case (L=5 cm), the rigid mould prevents the balloon to freely expand outside its constraint.

This does not happen in the second case (L=2 cm), where the balloon, being not as captive as before, is free to expand, especially in correspondence to balloon extremities. Consequently, a greater amount of fluid needs to be injected into the balloon to make the pressure increase, causing a shift of P-V curves.

Moreover, since the balloon is not anymore fully constrained inside a rigid cavity, the pressure increases is due to the stretch of the balloon material: the slope is therefore smoother and closer to the free-inflation slope, which represents the lowest achievable pendency.

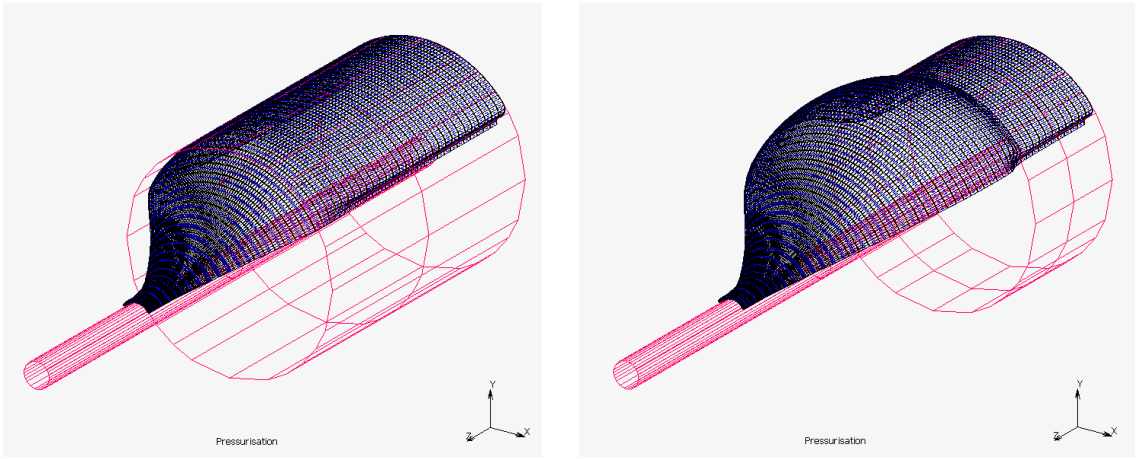

Figure 4.5 Example of numerical inflation of the balloon catheter inside rigid vessels having a length equal to 5 cm and 2 cm respectively and a fixed diameter (18 mm). In the first case (L=5 cm), the rigid mould prevents the balloon to freely expand outside its constraint. This does not happen in the second case (L=2 cm), where the balloon, being not as captive as before, is free to expand, especially in correspondence to lateral cones.

Elliptical shape: P-V curves

Ellipticity has been defined as short axis diameter/long axis diameter and its average value in human aortic vessels results to be equal to 0.82 [55]. The balloon has been inflated into six elliptic annuli, 2cm long, with ellipticity 0.82 and perimeters equal to the previously analysed circumferences, as shown in Figure 4.6.

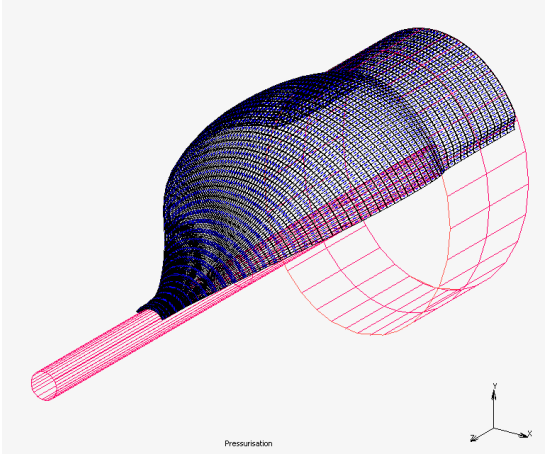

Figure 4.6 Example of numerical inflation of the balloon catheter inside a rigid elliptical vessel having a length equal to 2 cm.

The main outcomes of these simulations, shown in terms of P-V curves, are depicted in Figure 4.7.

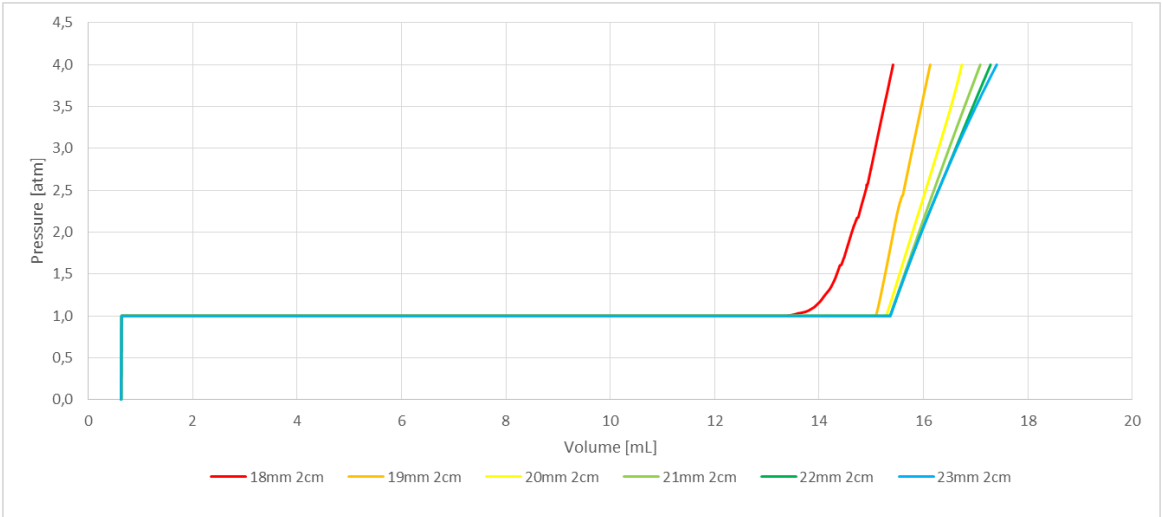

Figure 4.7 P-V curves representing the balloon inflation inside 2 cm elliptical vessels.

In Figure 4.8, a comparison between cylindrical and elliptical vessels having the same length (2 cm) is shown. The ellipticity of the annulus shifts the P-V curves to the right and modifies the slope during the pressurisation phase in a non-trivial way. Dot lines represent inflation inside elliptic vessels while solid lines depict pressurisation inside circular ones.

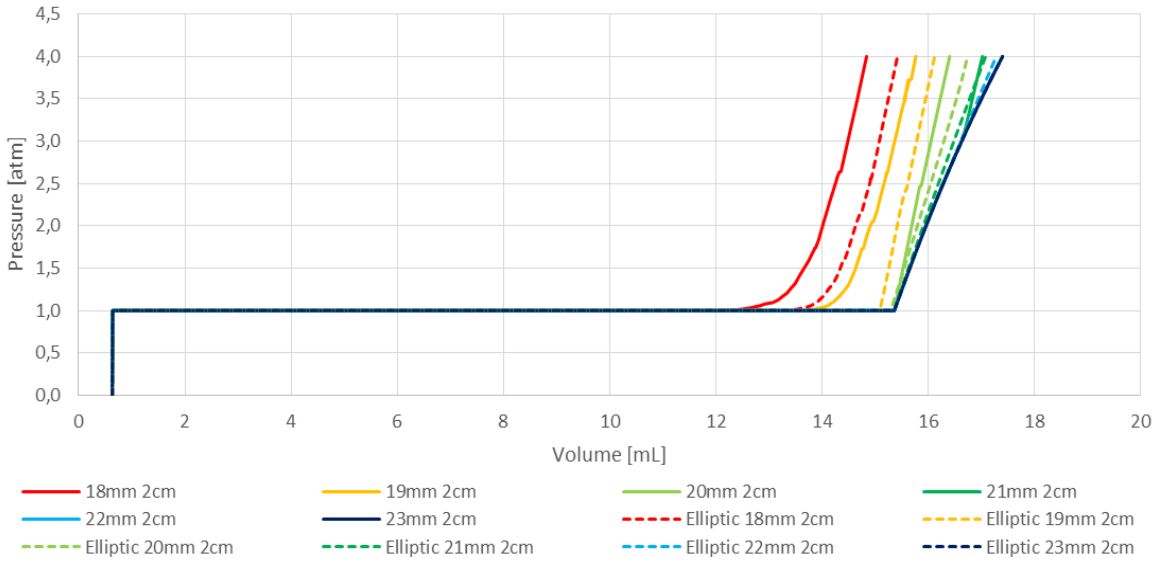

Figure 4.8 Comparison between cylindrical and elliptical vessels having the same length (2 cm). Dot lines represent inflation inside elliptic vessels while solid lines depict pressurisation inside circular ones.

Since ellipticity and reduction in annular length have a very similar effect on P-V curves, it might be very difficult, or even impossible, to univocally associate a curve to a combination of diameter, length and ellipticity.

4.1.2 Experimental results

After numerical simulations, whose findings have been described in previous section (Section 4.1.1), the same tests have been performed experimentally. Each test is depicted in terms of configuration of the experimental setup, description of meaningful findings and discussion of the main results. Despite some differences, which are going to be explained in the next paragraphs, experimental and numerical results are qualitatively very similar: therefore, experimental outcomes are shown together with numerical ones, in order to both enhance significant comparisons and outline existing discrepancies.

Effect of annular dimension

Figure 4.9 depicts balloon inflation inside circular rigid vessels having a fixed length set at 5 cm and a diameter range equal to 18 mm – 23 mm. This test has been performed to assess whether or not the balloon is able to detect different annular diameters, by monitoring the evolution of intra-balloon pressure and injected volume over time, and its main outcomes are presented in Figure 4.10.

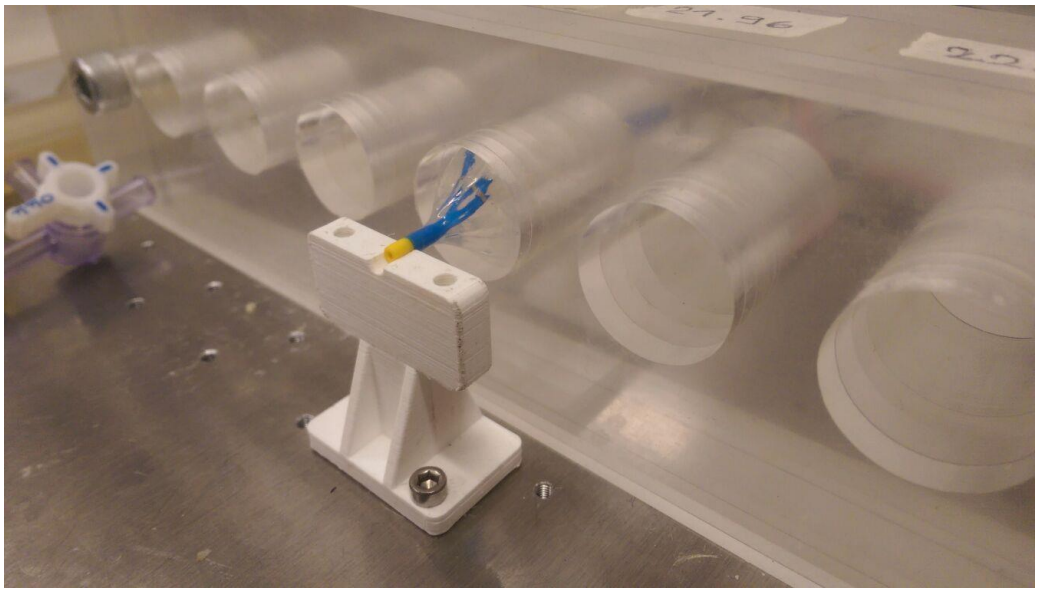

Figure 4.9 BAV balloon catheter inflated inside circular rigid vessels. Diameter ranges from 18 mm to 23 mm while annular length has been fixed equal to 5 cm.

The differences between numerical and experimental data are highlighted in Figure 4.10. As expected, free inflation curve completely overlaps to the line associated with 23 mm diameter annulus.

Numerical curves associated with smaller diameters (Ø18 mm, Ø19 mm and Ø20 mm) result to be slightly shifted towards the right. On the contrary, Ø23 mm diameter and free inflation curves present the opposite behaviour, being shifted towards the left. Moreover, the extent of this shift is not constant.

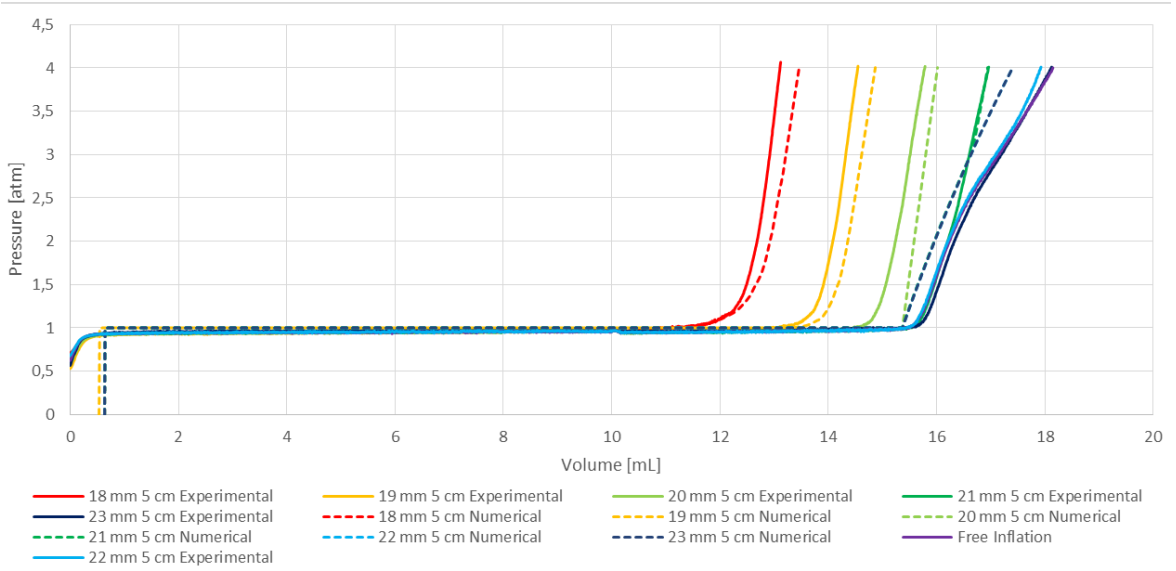

Figure 4.10 Balloon inflation inside six different phantom vessels having different diameters and a fixed length (5 cm). Dot lines represent Numerical Data while solid curves correspond to Experimental Results

There are several explanations for this behaviour.

First, looking at free inflation curves, it is clear that the numerical model has been slightly underestimated. It is fair to assume that the nominal diameter should be closer to 21 mm instead of 20 mm, as stated from the beginning. This under-estimation causes the shift to the left of numerical curves: being smaller than the real one, the numerical balloon shows similar pressure increase in correspondence to smaller volumes.

Regarding instead smaller diameters, it must be taken into account that, due to the inherent inaccuracy of the micromachining process, the nominal diameter of the holes is slightly smaller if compared to the one used inside numerical simulations. Being the system so sensitive, this could result in an experimental shift towards the left.

Furthermore, an additional interesting point regards the behaviour of the free inflation curve at high pressures. The pattern of this specific curve recalls the stress-strain behaviour of hyperelastic materials. P-V curves can be related to Stress-Strain evaluation: as a matter of the fact, the volume represents an estimation of strain while pressure applied on the internal cavity of the balloon can be considered a measure of stress. This pattern is visible during the free inflation phase, when the balloon material is free to expand and stretch, while it cannot be seen looking at smaller diameters curves, where the balloon is bound inside the annulus. Finally, the material disruption should be also taken into account: the balloon has been tested more than 100 times and, probably, the material has been radially damaged.

Figure 4.11 shows the standard deviation of experimental tests. As clearly visible from the graph, data result to be closely distributed around the mean value. The highest value of standard deviation belongs to the free inflation curve and is equal to 0.026 atm.
Low values of standard deviation indicate a great repeatability and reproducibility of the procedure.

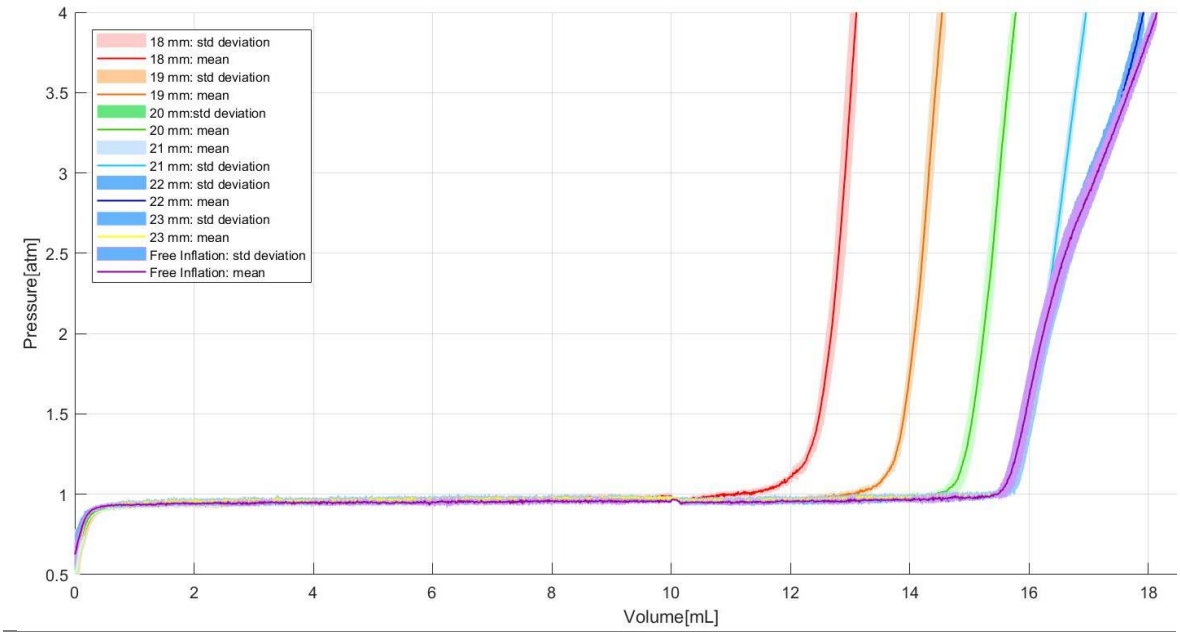

Figure 4.11 Experimental Tests: mean curves and standard deviation

Length effect on P-V Curves

Regarding the influence of the length on P-V curves, its impact has been assessed on four vessels with different length (5 cm, 4 cm, 3 cm, 2 cm) and a Ø18mm diameter, as done for numerical tests.

In this case, intermediate lengths have not been tested for the sake of simplicity: however, it is fair to assume that they would have been bounded by the ones associated with external lengths. This test has been carried out in order to establish whether there is a correlation between changes in annular length and P-V curves shifts.

It is clear from Figure 4.12 that experimental results confirm the same phenomenon previously observed with computational data (Figure 4.3): a shorter annulus results to slightly reduce the slope of all the P-V curves during the pressurisation phase.

In this case it could be also appreciated the mild bending of the 2 cm long curve, due to the hyperelasticity of the material. This behaviour is not evident from curves related to longer cylinders, as the rigid mould prevents the balloon to freely expand outside its constraint. Moreover, even numerical curves do not show this particular pattern, since the numerical model has been created considering a linear elastic material.

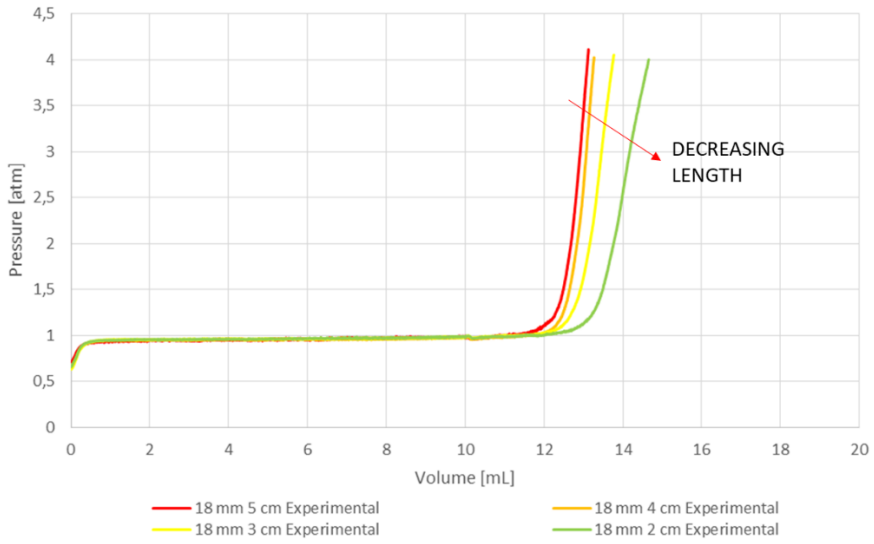

Figure 4.12 Balloon inflation inside the same annulus (18 mm diameter) having four different lengths: 5 cm, 4 cm, 3 cm and 2 cm.

Even in this case, values of standard deviation prove a good reproducibility of experimental tests, being on average equal to 0.025 atm.

However, as previously observed with numerical simulations, annular length results to have a twofold effect: it slightly reduces the slope of all the P-V curves during the pressurisation phase but it also shifts to the right P-V curves associated with diameters smaller than the non-tensioned diameter of the balloon. In this regard, the balloon catheter has been inflated inside rigid vessels having different diameters and a fixed length equal to 2 cm, as shown in Figure 4.13.

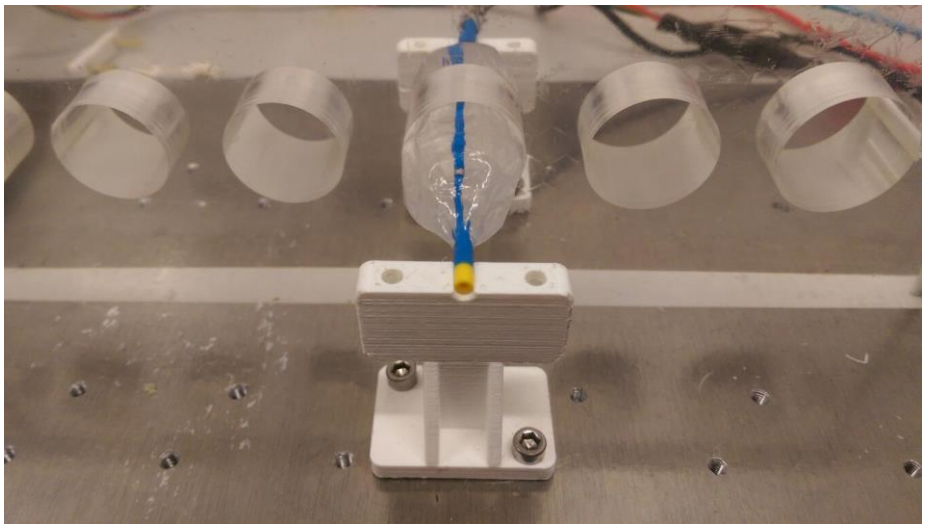

Figure 4.13 balloon inflation inside circular rigid vessels having a fixed length set at 2 cm and a diameter range equal to 18 mm – 23 mm.

The main outcomes of this test, compared with experimental tests inside 5 cm vessels, are depicted in Figure 4.14. P-V curves associated with shorter vessels are slightly shifted towards the right; the extent of this shift is not constant and it seems to decrease as the vessel diameter increases. The hyperelastic behaviour in curves associated with 2 cm long vessels is clearly visible: being not as captive as before, the balloon is now free to expand, especially in correspondence to lateral extremities. This characteristic shape, shown in Figure 4.15, has been termed the “dog-bone” effect in literature.

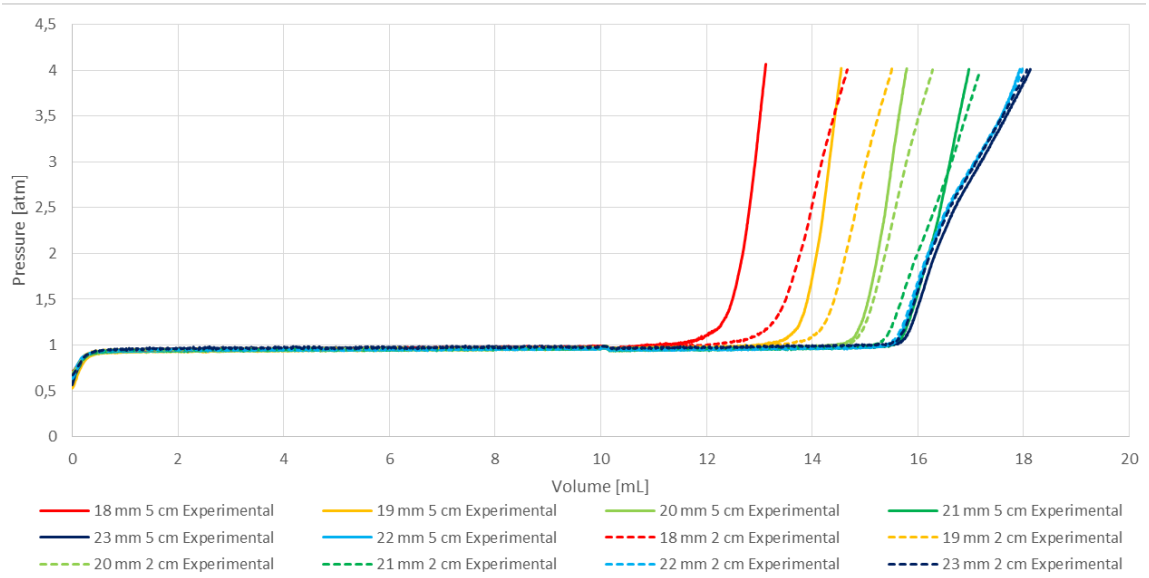

Figure 4.14 P-V curves showing the twofold effect of changes in annular length: balloon has been inflated inside rigid vessels having different diameters and a fixed length equal to 2 cm and 5 cm respectively. Dot lines represent curves associated with balloon inflation inside vessels 2 cm long while solid lines are related to 5 cm rigid phantom vessels. P-V curves are shifted towards the right and their slope during the pressurisation phase is decreased. Moreover, dot curves show the hyperelastic behaviour of balloon material. All data refer to experimental tests.

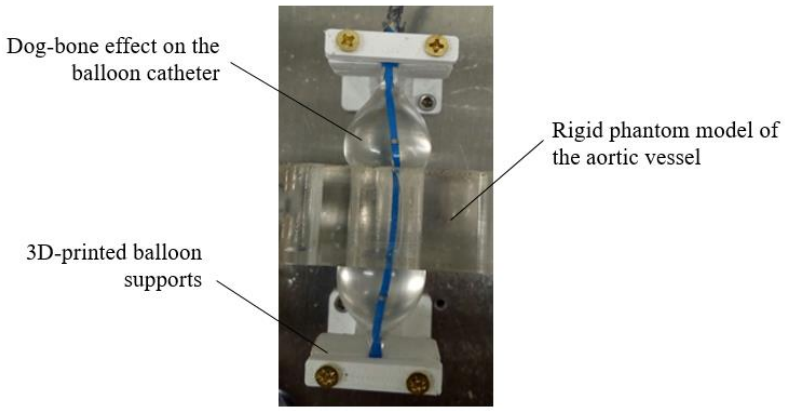

Figure 4.15 Dog-bone Effect: this particular shape is much more evident when the annulus length is equal to 2 cm.

Besides this pending toward the right, however, it is still possible to univocally identify a diameter-length combination, for diameters ≤ 21mm, by simply looking at the p-V curves.

Elliptical shape: P-V curves

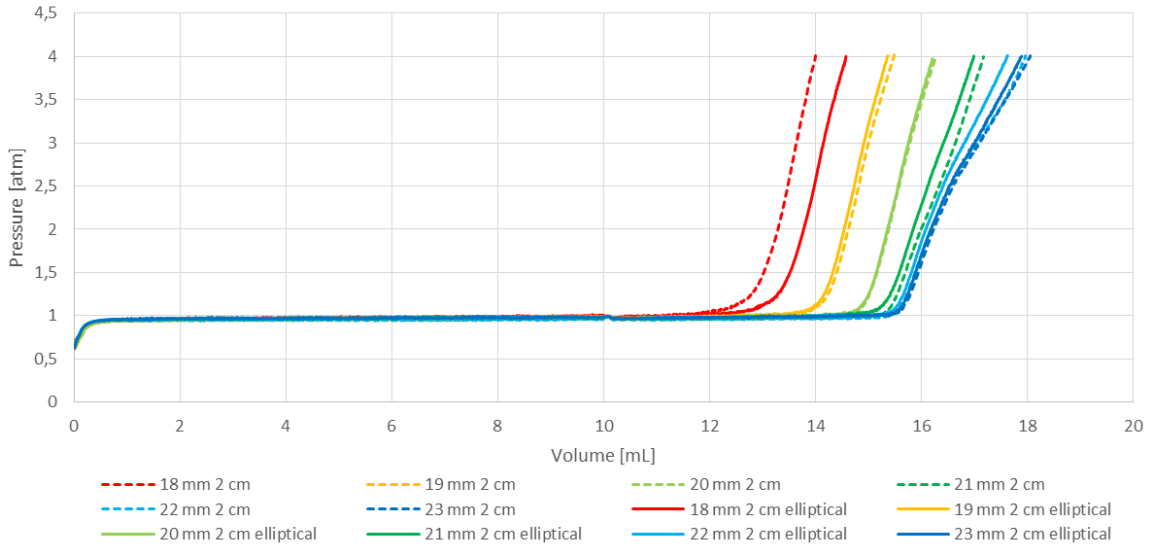

Figure 4.16 Comparison between elliptical and circular annuli: the balloon was inflated in 6 elliptic annuli, 2cm long, with ellipticity 0.82 and perimeters equal to the previously analysed circumferences

These tests have been performed by inflating the balloon catheter inside elliptical phantom vessels and by simultaneously recording the intra-balloon pressure and the injected volume. Even in this case, tests have been repeated five times for each vessel and the values of standard deviation are quite low, being on average equal to 0.016 atm. Figure 4.16 compares experimental inflations inside circular and elliptical phantom vessel. This test has been done in order to assess whether the balloon catheter is able to retrieve not only the geometry and the length but also the shape of the vessel. Unfortunately, as clear from Figure 4.16, ellipticity and reduction in annular length have a very similar effect on P-V curves: both parameters determine in fact a moderate shift towards the right. Consequently, it might be very difficult, or even impossible, to univocally associate a curve to a combination of diameter, length and ellipticity. The shape of the annulus cannot be retrieved with this approach, especially if combined with length variability.

4.2 Detection of Soft Tissue Distensibility

Once the experimental setup has validated the numerical model regarding the inflation of the balloon inside rigid annuli, a more challenging scenario has been taken into account, whereby the balloon has been inserted inside compliant silicone vessels.

In this case, both the diameter and the length of the vessel have been kept constant and equal to 18/19 mm and 5 cm respectively. Only circular vessels have been considered and, similarly to the rigid analysis, experimental results are here presented in terms of P-V curves. The values of D is calculated for the inflation phase as the local slope of the V-P curve and it is normalised over the initial volume, giving the value of distensibility of each sample.
As previously done with rigid annuli, each test has been repeated five times for every cylinder, in order to ensure the repeatability and reproducibility of the data.
Below each graph, in addition to findings description, a brief discussion of the results is provided. Mean curve and standard deviation of experimental tests are shown here as well.

4.2.1 Numerical Results

Knowing cavity pressure and volume variations, calculated according to the procedure illustrated in Section 3.2.2, distensibility has been computed; these values, shown in Table 12, will be compared to the values extracted through experimental tests.

	18 mm diameter	**19 mm diameter**
Pressure gradient [MPa]	189.3568	92.3656
Distensibility [mmHg^{-1}]	0.00124	0.00175

Table 12 Marc Numerical Simulations: expected silicone distensibility and corresponding pressure gradient

As expected, obtained distensibility is smaller than the physiological one extracted from literature data (see Table 5). As explained in Chapter 3, the thickness of this phantom vessel has been chosen in order to mimic the physiological distensibility reported in literature; however, since a thickness of 4.5 mm results in a radial displacement which is on average

0.01 mm lower than the desired one (see Table 9 Chapter 3), the numerically computed distensibility results to be slightly smaller.

However, the most striking result to emerge from the data in Table 12 is the distensibility of 18 mm diameter annulus: the latter, in fact, is lightly stiffer with respect to both 19 mm diameter vessel (0.00175 $mmHg^{-1}$) and the physiological reference value (0.0018 $mmHg^{-1}$).

In line with previous considerations, the greater the difference between physiological radial displacement and numerical radial displacement (see Table 9) the larger the difference in terms of distensibility.

These are the reference values that have been compared with the one retrieved experimentally, as explained in Section 4.2.2.

4.2.2 Experimental Results

Figure 4.18 shows P-V curves obtained from the inflation of the BAV Balloon Catheter inside Ø18 mm (top) and Ø19 mm (bottom) compliant vessels respectively. The configuration of the experimental setup is shown in Figure 4.17.

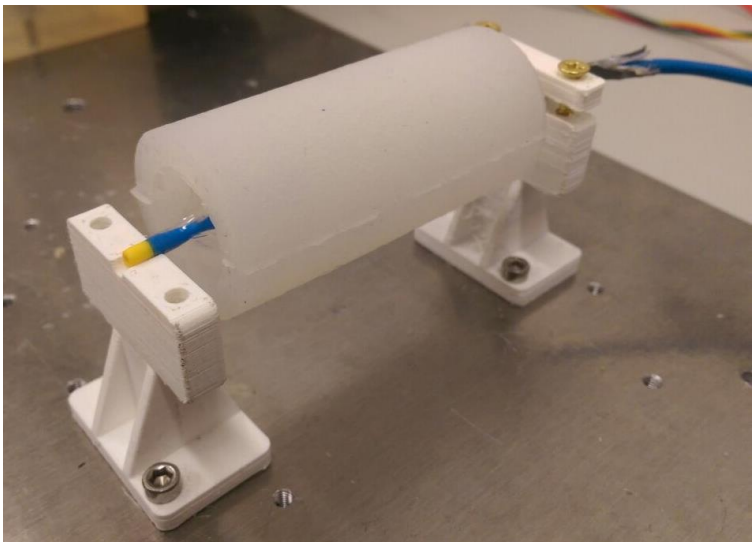

Figure 4.17 Experimental setup used to retrieve compliance measurements: the BAV balloon catheter is inflated inside silicone-based phantom vessels. During the inflation process, 3D-printed holders are used to keep the device in place.

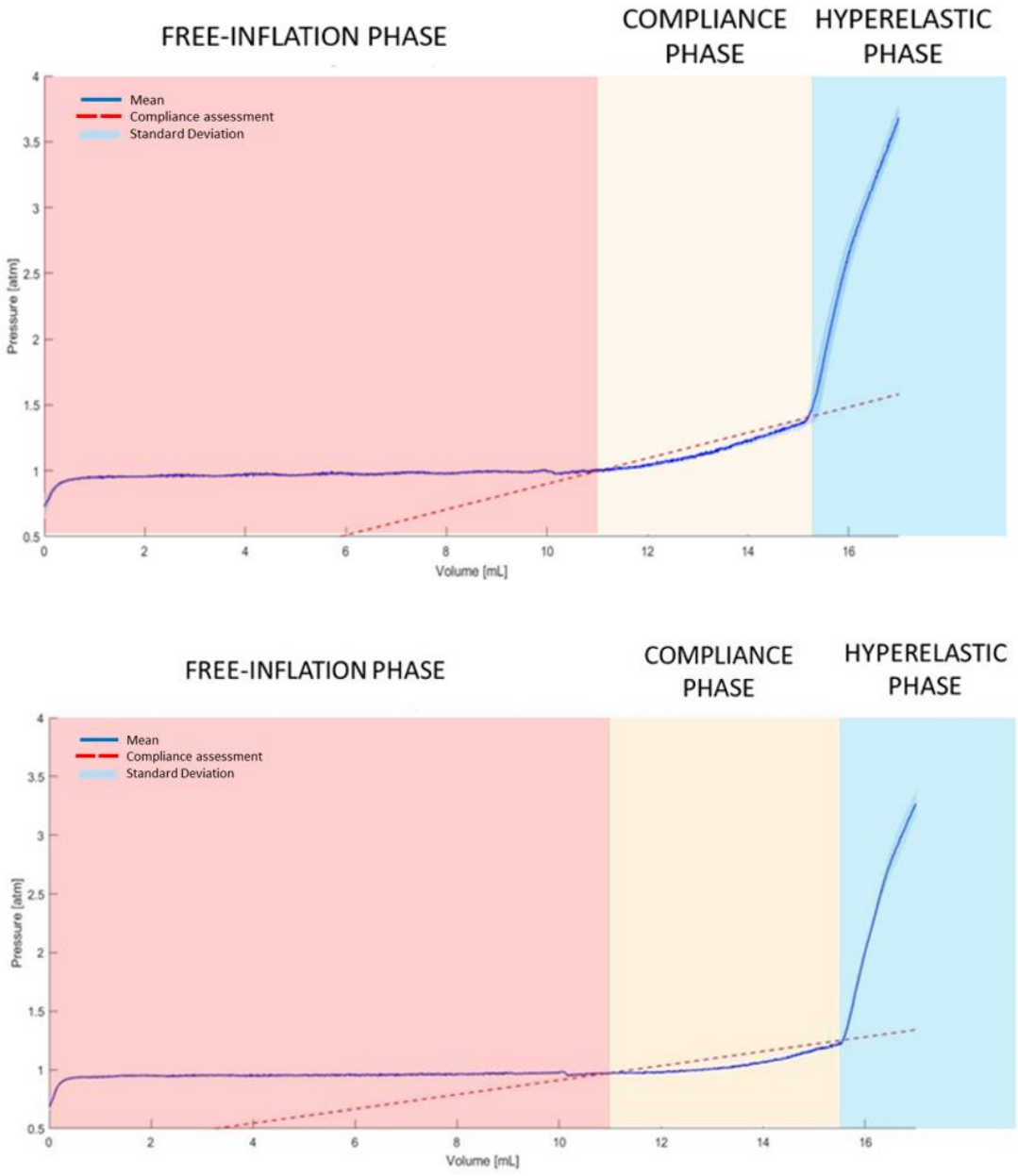

Figure 4.18 Compliance assessment: P-V curves have been obtained by inflating the balloon catheter inside Silicone-based compliant annuli. In the graphs, mean curve and standard deviation are shown respectively as blue solid and shaded lines. The red dot line represents vessel distensibility under linear assumptions.

As shown in Figure 4.18, data can be divided into three main sections, named free-inflation phase, compliant phase and hyperelastic phase.

As far as Ø18 mm vessel is concerned, during the free-inflation phase the balloon simply regains its natural configuration from the initial tri-folded state.

The free-inflation phase is characterised by a constant pressure equal to the atmospheric one, while the final amount of volume injected varied accordingly to the dimension of the balloon, as expected. Until this point, nothing has changed with respect to balloon inflation inside rigid vessels.

Then, the pressure starts to increase. Contrarily to what happens inside rigid vessels, the rise is initially very slow and almost linear. During this phase, the balloon is touching the walls of the compliant vessels and the internal surface of the cylinder is expanding. The extent of this radial displacement goes from 0 mm up to 1 mm. In the graph, the red dot line represents the linear approximation that has been used to compute the annular distensibility, as the ratio between the volume variation and the associated pressure change. The steepest the pendency of this curve, the smaller the distensibility of the vessel. This line has been drawn on Matlab defining two points: the first point is where the pressure of the intra-balloon cavity increases by 5 % of the whole pressure elevation. The second point, instead, corresponds to the knee of the curve in the transition between the compliant phase and the hyperelastic one.

Finally, the third and last part comprises the expansion of both the vessel and the balloon. Again, the hyperelasticity of the balloon material can be observed. Being not able to distinguish the compliance of the vessel from the compliance of the BAV balloon catheter, this curve section cannot be considered in the evaluation of the annulus distensibility.

Ideally, neglecting the compliant section, it would be possible to regain one of the curves shown in the rigid analysis, by simply connecting the free inflation phase with the hyperelastic one.

The numerically estimated distensibility is equal to 0.00124 $mmHg^{-1}$ while the value retrieved from experimental tests corresponds to 0.00121 $mmHg^{-1}$. The error, computed as the difference between the numerically computed and the experimental value, is therefore equal to 0.00003 $mmHg^{-1}$.

Then, the same approach has been used to compute the distensibility associated with a silicone-based Ø19 mm cylinder, shown in the second graph of Figure 4.18. In this case, the radial displacement of the silicone vessel should go from 0 up to 0.5 mm; above this value,

the computed compliance results to be comprehensive of both the distensibility of the tissue and the distensibility associated with the balloon material.

According to the red dot line shown in the above picture, the distensibility of the vessel is equal to 0.00195 $mmHg^{-1}$. The error, computed as the difference between the numerically assessed and the experimental value, is therefore equal to 0.0002 $mmHg^{-1}$.

Standard deviation is always very low, with average values equal to 0.026 $mmHg^{-1}$ and 0.017 $mmHg^{-1}$ respectively, implying both a good reproducibility and repeatability of the measurements.

4.3 Curves Analysis: how to retrieve annulus diameter from P-V curves

In this section, an analytical method to automatically retrieve annulus diameter from P-V curves is introduced. For the sake of clarity, the following strategy has been firstly applied to numerical results, since phenomena under consideration appear more marked and visible. Subsequently, this method has been verified on experimental data as well.

The reason why this algorithm is described in Chapter 4 instead of Chapter 3 is twofold: on the one hand, it represents additional analysis on P-V curves and it could be therefore considered as further discussion but, most importantly, it is strictly related and based on numerical and experimental results, which have been shown only in the present Chapter.

To obtain a meaningful analysis, further numerical simulations concerning intermediate diameters vessels (Ø18.5 mm, Ø19.5 mm, Ø20.5 mm) have been performed.
A fixed length equal to 5 cm has been considered, neglecting length, ellipticity and compliance effects.
Later on, length influence as well as ellipticity and compliance effects could be included in the analysis: to do this, the number of required parameters must increase with the growing number of unknowns, corresponding to different combinations of length, ellipticity and compliance values.

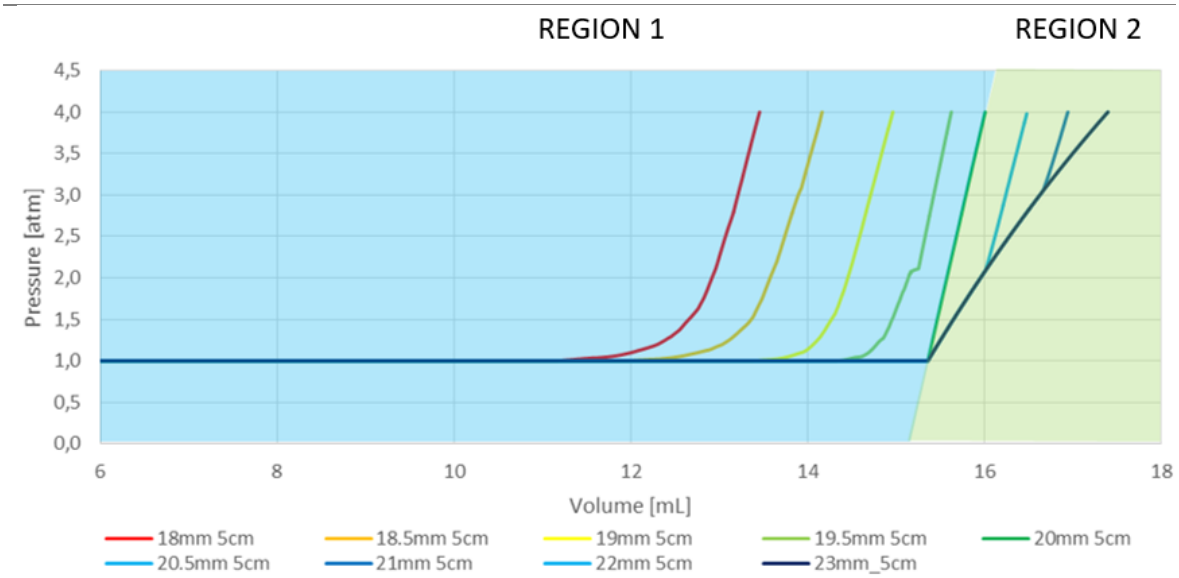

Figure 4.19 According to their trend, numerical P-V curves associated with balloon inflation inside rigid vessels can be divided into two regions: the first one refers to annulus diameters smaller than 20 mm while the second on the right represents P-V curves of 21 mm, 22 mm, 23 mm diameters and free inflation.

As shown in Figure 4.19, the graph has been divided into two regions: the first one refers to vessels diameters smaller than 20 mm while the second represents P-V curves of 21 mm, 22 mm, 23 mm diameters and free inflation.

As clearly visible in Figure 4.20, curves in region 1 show a trend similar to

$$f(x) = \ln(1 + e^{x}) \qquad \text{Eq. 14}$$

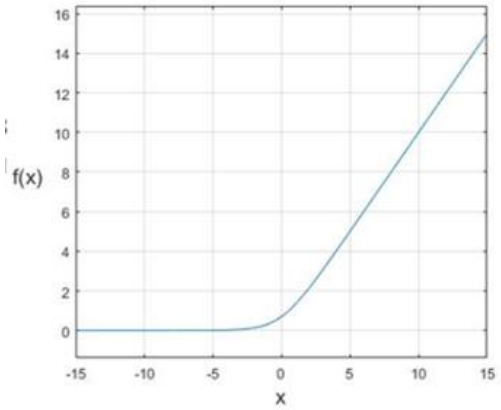

Figure 4.20 P-V curves associated with diameters lower than 20 mm show a trend similar to Eq. 14

The first derivative of this function is the logistic sigmoid curve, shown in Eq. 15 and graphically represented in Figure 4.21.

$$\frac{df(x)}{dx} = g(x) = \frac{e^x}{e^x + 1} \qquad \text{Eq. 15}$$

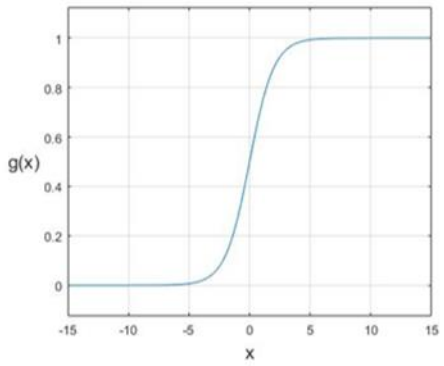

Figure 4.21 Graphical representation of the logistic sigmoid function, retrieved as the first derivative of Eq. 14

A parametric version of Eq. 14 has been used to fit data associated with an annular length equal to 5cm by means of Matlab Curve Fitting Toolbox™, which provides an app and functions for fitting curves and surfaces to data.

The correspondent equation is reported in Eq. 16, showing a dependence from three parameters a, b and c.

$$f_p(x) = a\ln(1 + e^{b(x-c)}) + 1 \qquad \text{Eq. 16}$$

$f_p(x)$ is made of two different terms: the first one, $f(x)$, which is the parametrical integral of the sigmoid, and an additional one, 1, which has been introduced to vertically shift all the curves so that the initial pressure is equal to 1 atm.

The influence of these three parameters has been analysed in details. The slope of the linear part of the curve is influenced by the value of "b" parameter while "c" coefficient represents its horizontal shift. Mathematically, it is the centre of the knee of the function $f(x) = \ln(1 + e^x)$ (or the maximum of $\frac{d^2f(x)}{dx^2}$), for which the third derivative is equal to zero. In Figure 4.22, blue line represents f(x), red line corresponds to its first derivative while yellow curve represents its second derivative. As clear from the graph, the value of c corresponds to the centre of knee of the f(x) function but also to the maximum of the second derivative curve.

Besides, "a" parameter indicates the width of the knee of the function $f(x) = \ln(1 + e^x)$.

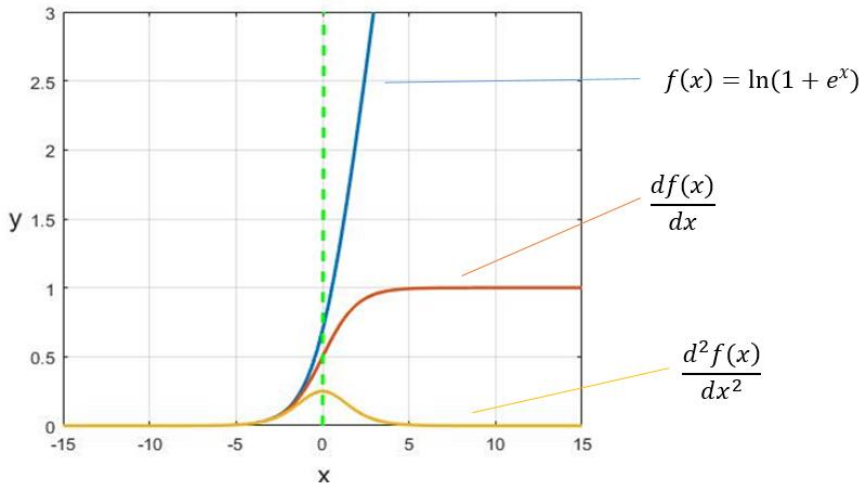

Figure 4.22 Blue line represents f(x), red line corresponds to its first derivative while yellow curve represents its second derivative. As clear from the graph, the value of c (green dot line) corresponds to the centre of the knee of the f(x) function but also to the maximum of the second derivative curve.

Figure 4.23 shows the variation of P-V curves depending on parametrical values. As expected, as the value of "a" increases, knees become steeper. On the other hand, the bigger the value of "b" parameter the greater the slope of the curve. Finally, as the value of "c" changes, P-V curves horizontally move to the right.

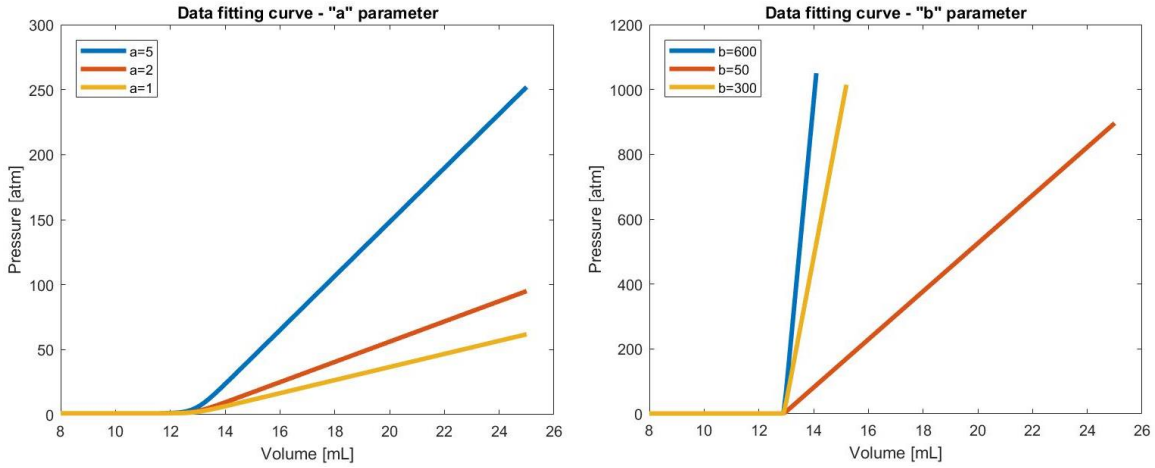

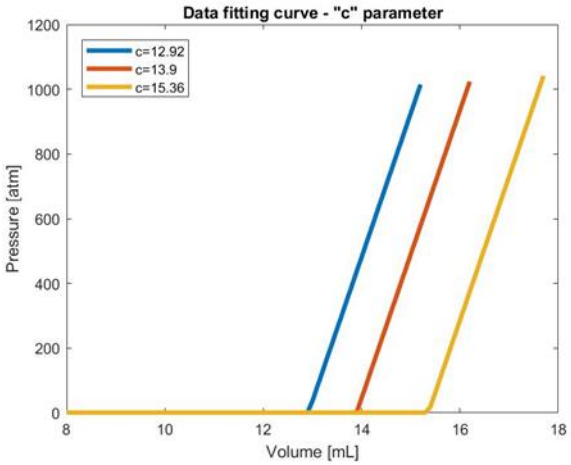

Figure 4.23 Influence of the three parameters (a, b, c) on data fitting curve f(x): (a) as the value of a increases, knees become steeper; (b) the bigger the value of "b" parameter the greater the slope of the curve; (c) as the value of "c" changes, P-V curves horizontally move to the right.

Among the three parameters previously mentioned, the only one which shows a strong and monotonic correlation with the annular diameter is "c", as shown in Table 13. R^2 and RMSE errors have been computed as well, according to Eq. 17 and Eq. 18:

$$R^2 = \frac{SSR}{SST} = \frac{\sum_{i=1}^{n} w_i(\hat{y}_i - \bar{y})^2}{\sum_{i=1}^{n} w_i(y_i - \bar{y})^2} \qquad \text{Eq. 17}$$

$$RMSE = \sqrt{\frac{\sum_{i=1}^{n} w_i(y_i - \hat{y}_i)^2}{\nu}} \qquad \text{Eq. 18}$$

where SSR is the sum of squares of the regression and SST is the total sum of squares. In particular, y_i represents experimental data, $\bar{y}$ is the mean value of experimental data and $\hat{y}_i$ corresponds to estimated data from the model. Finally, ν indicates the number of independent pieces of information involving the *n* data points that are required to calculate the sum of squares.

R^2 measures how successful the fit is in explaining the variation of the data (R^2=1 represents a perfect fitting). In a very similar way, an RMSE value closer to 0 indicates a fit that is more useful for prediction. Both these values show optimal results, indicating an excellent fitting.

DIAMETER [mm]	a	b	c	R^2	RMSE
18	1.482	3.571	13.173	0.9994	0.0217
18.5	0.9207	4.297	13.7147	0.9995	0.02
19	0.3518	7.342	14.2575	0.9956	0.0609
19.5	1.111	5.689	15.0241	0.9934	0.0725
20	0.008141	568.3	15.4617	1.0000	0.0018

Table 13 Automatic algorithm has been applied to numerical data: values of "c" parameter depending on annular diameter is shown. Furthermore, values of R^2 and RMSE errors are presented, indicating optimal fitting.

The goodness of this approximation can be observed also in Figure 4.24, where the numerical curves and the numerical fitting are provided.

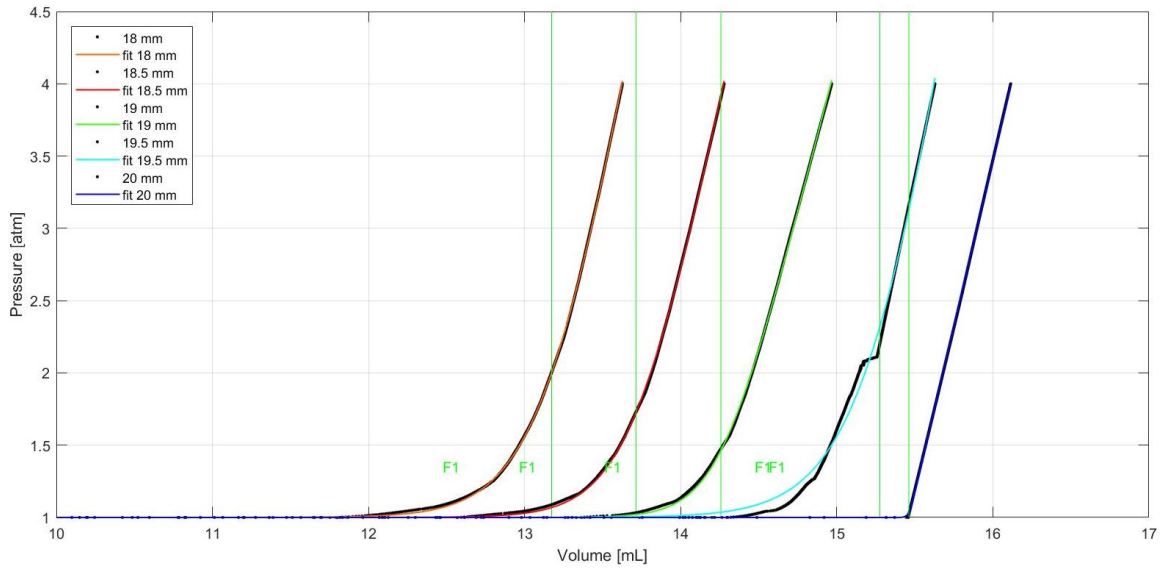

Figure 4.24 Data Fitting: black dots represent data retrieved from numerical simulations while solid lines correspond to fitting curves. Moreover, green lines are displayed as well, representing the value of c parameter (F1 Feature).

Figure 4.25 displays the positive and almost linear correlation between c parameter and annular dimension: five discrete values of the "c" parameter have been linearly interpolated. Knowing this curve, it could be now possible to retrieve even intermediate dimensions of the aortic annulus by simply looking at the value of the third parameter c, displayed along the y-axis.

As previously said, this value of c can be obtained by fitting P-V curve associated to the vessel with the parametric integral of the sigmoid function previously reported.

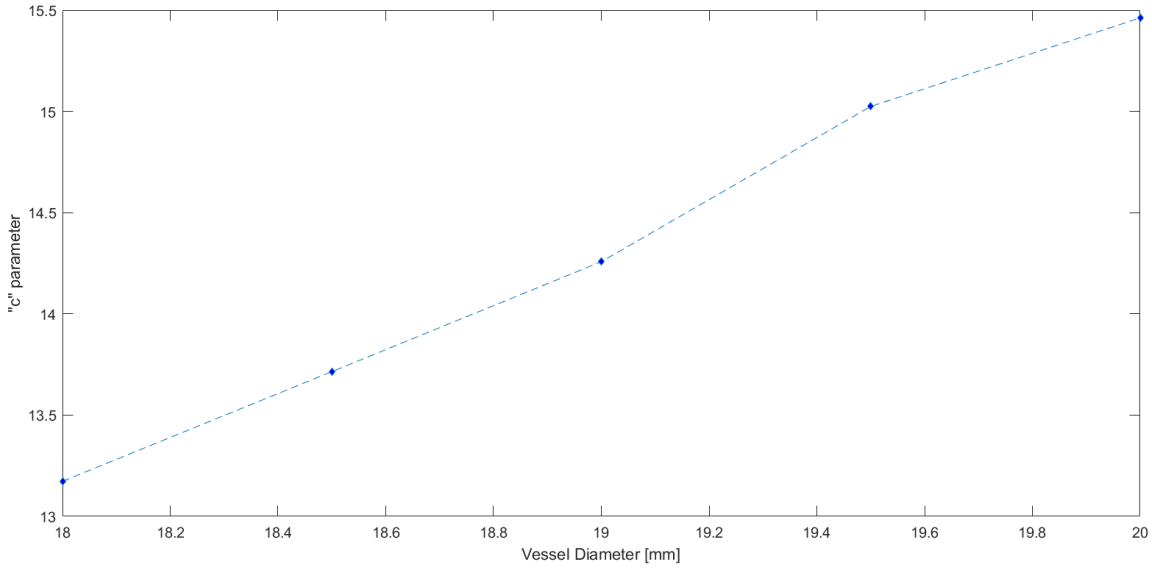

Figure 4.25 Correlation between the value of the c coefficient and the correspondent annulus diameter

Previous pages focused on curves associated with diameters smaller than 20 mm, belonging to the first region displayed in Figure 4.19. In this case, by fitting the numerical P-V curves with the parametric integral of the logistic function, it is possible to retrieve the annulus diameter by simply looking at “c” parameter.

Regarding instead the second region of Figure 4.19, which displays numerical curves associated to Ø20.5 mm, Ø21 mm, Ø22 mm and Ø23 mm (totally overlapped with free inflation curve), the approach is slightly different and more straightforward. In this case, the increase in pressure is not anymore due to the contact between the balloon and the vessels walls but instead the balloon material stretching causes it. As clear from Figure 4.26, there is a positive correlation between the inflection point of the curve, computed as the intercept of the specific P-V curve and the free inflation one, and the diameter of the vessel.
Values, reported in Table 14, have been computed by fitting the slope of the curve after the inflection point and by retrieving the intercept between this fitting and the line associated with free inflation.

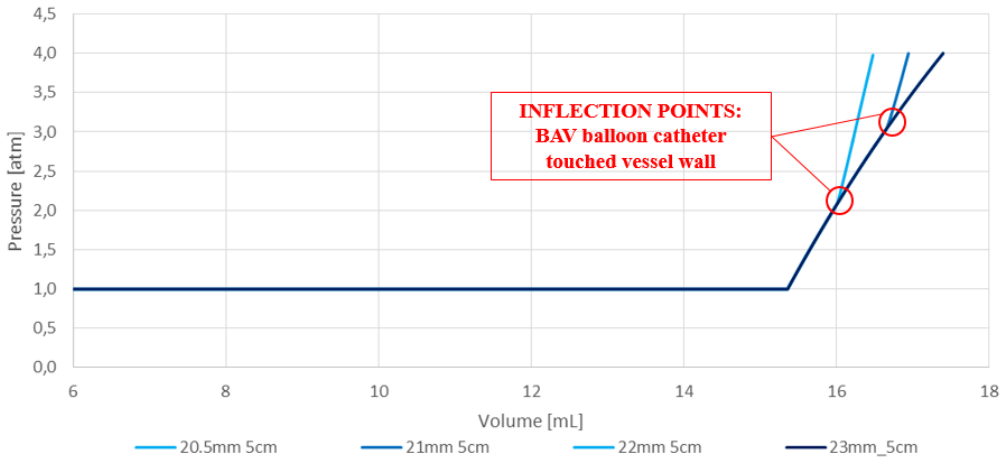

Figure 4.26 Numerical data, Region 2: in this case, a positive correlation between the position of the inflection point and the dimension of the annulus is present. As clear from the image, the larger the dimension of the vessel the higher is the y-coordinate (or the x-coordinate) of its inflection point.

Vessel Diameter [mm]	Inflection point (X)	Inflection point (Y)
20.5 mm	16.02	2.089
21 mm	16.67	3.054

Table 14 Correlation between the position of the inflection point and the correspondent annulus diameter

Moving now towards experimental data, the same approach has been applied to experimentally gathered P-V curves. As previously done with numerical data, even in this case the herein described strategy is made of two different approaches: the first one is applied to vessels diameters smaller than 20 mm while the second one regards P-V curves of 21 mm, 22 mm, 23 mm diameters and free inflation. In the following lines, the main results are briefly described.

Curves belonging to the first category have been fitted with the previously described logistic function and the values of "c" parameter, R^2 and RMSE errors are shown in Table 15.

DIAMETER [mm]	a	b	c	R^2	RMSE
18	1.778	4.188	12.7479	0.9992	0.0195
19	0.8845	5.794	13.9567	0.998	0.0137
20	0.5332	7.351	15.0078	0.9997	0.0158

Table 15 Automatic algorithm has been applied to numerical data: values of "c" parameter depending on annular diameter is shown. Furthermore, values of R^2 and RMSE errors are presented, indicating optimal fitting.

As clear from the table, values of R^2 and RMSE errors indicate an optimal fitting. The positive correlation between the "c" parameter of the logistic function and the value of the annular diameter is confirmed by experimental results. The herein described strategy to retrieve vessel diameter lower than 21 mm is therefore validated by experimental tests as well. The goodness of the model approximation can be observed also in Figure 4.27, where the experimental curves and the numerical fitting are provided.

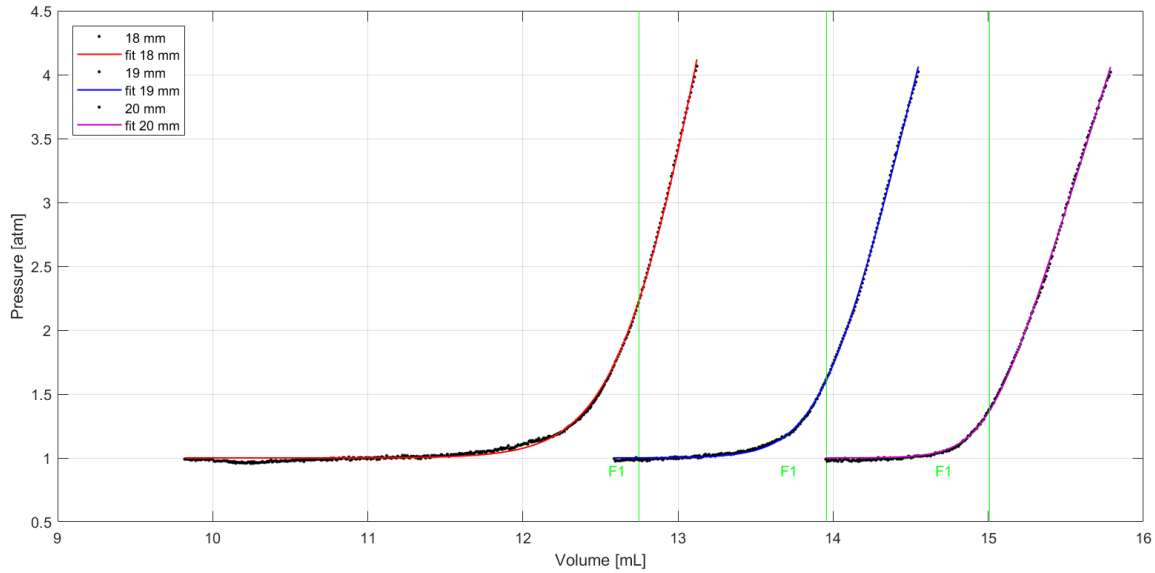

Figure 4.27 Data Fitting: black dots represent data retrieved from experimental tests while solid lines correspond to fitting curves. Moreover, green lines are displayed as well, representing the value of c parameter (F1 Feature).

Regarding instead inflation curves associated with greater diameters, in accordance with numerical observations, there is a positive correlation between the position of the inflection point and the dimensions of the vessel. Coordinates values have been computed by fitting the slope of the curve after the inflection point and by retrieving the intercept between this fitting and the line associated with free inflation.

In conclusion, the retrieval of the annulus diameter from P-V curves can be split into two different analysis: when the vessel is smaller than the non-tensioned diameter of the balloon (20 mm, Region 1), data must be fitted with a parametrical logistic function, considering the value of the "c" parameter. Instead, when the vessel is greater than the non-tensioned diameter of the balloon, the dimension of the annulus can be retrieved by looking at one of the two coordinates of the inflection point.

The region on the left-hand side of Figure 4.19 seems to be more favourable to the retrieval of vessel dimensions: the inflection point is an invariant measure of annulus geometry, being not dependent on the length of the vessel. On the other hand, the "c" parameter does not represent an equally good and reliable benchmark, since its value slightly changes according to the length of the phantom vessel. Therefore, in this last case, the herein suggested method is applicable merely under assumptions of constant annular length.

4.4 Summary

In the present section, all the data collected from both numerical and experimental analysis are reported. These results further support the idea that it is possible to retrieve the annulus geometry and the distensibility of the soft tissue without using imaging techniques, but instead simply recording P-V curves from the intra-balloon cavity. Apart from some little differences, which will be discussed in details in the final chapter of this thesis, numerical and experimental results are consistent.

Regarding geometry retrieval, the balloon catheter is not only able to detect the dimension of the phantom vessel but it is also sensitive to changes in annular length. On the contrary, as far as shape analysis is concerned, the device is not able to distinguish between elliptical and circular vessels, under the assumption of length variability.

In terms of compliance assessment, the difference between numerically computed values and experimental ones is equal to 0.0002 $mmHg^{-1}$ and 0.00003 $mmHg^{-1}$, associated respectively to Ø19 mm annulus and Ø18 mm one. The balloon catheter is therefore able to retrieve soft tissue compliance, under the assumption of length and shape constancy.

Finally, an analytical algorithm to automatically retrieve the dimension of the annulus from P-V curves has been introduced and validated with experimental results. This strategy comprises two different approaches: when the vessel is smaller than the non-tensioned diameter of the balloon (20 mm, Region 1), data must be fitted with a parametrical logistic function, considering the value of the "c" parameter. Instead, when the vessel is greater than the non-tensioned diameter of the balloon, the dimension of the annulus can be retrieved by looking at one of the two coordinates of the inflection point.

Further discussions are provided in the next and last chapter of this thesis.

Chapter 5

CONCLUSIONS AND SUGGESTIONS FOR FUTURE WORK

This chapter summarises and highlights the main achievements of each section.

In the next lines, the clinical relevance and the limitations of the present approach are identified as well, leading to suggestions for future work.

5.1 Clinical Relevance

Sophisticated and complex techniques to retrieve vessel geometry and soft tissue compliance have been extensively described and they are currently applied in clinical practice.
However, these techniques seem to lack in accuracy and they seldom bring to overestimation of annular dimensions.

These results, whose interpretation must take into account a number of approximations and idealizations introduced in order to simplify the numerical requirements and the experimental validation, suggest a reliable method to accurately estimate vessel material and geometrical properties.

The clinical relevance of this work is twofold. On the one hand, it presents a cost-effective and accurate method to use a commercially available device to perform a more conservative selection of prosthesis sizes, matching the patient's anatomical dimensions and therefore reducing TAVR complications without including any kind of imaging technique. On the other side, this work lays the foundations for the future development of a new soft-robotic

catheter, able to automatically obtain patient-specific implantation sites features by means of a mechatronic and completely stand-alone system.

5.2 Conclusions

The following conclusions are drawn:

Methodological considerations

1. All chapters of this thesis are conceptually organised into two different parts, which are nevertheless strictly related. This is consistent with the approach followed experimentally. First, results regarding the analysis of vessel geometry have been introduced; subsequently, graphs and P-V data obtained from the inflation of the BAV Balloon catheter inside silicone-based compliant vessels have been presented. Besides, each of these sections provides a comparison between two different approaches: a numerical approach, aimed at inferring the feasibility of the herein suggested strategy, and an experimental analysis, whose purpose is to validate numerical simulations verifying that a commercially available device can really improve TAVR procedure and results.

Measuring soft tissue compliance and vessel geometry – State of the art

2. A thorough and consolidated literature sought to identify a gold standard for the exact measurement of the aortic annulus diameter and compliance. Prior to TAVR, annulus size can be estimated using either imaging techniques or intra-balloon pressure measurements. Additionally, a more sophisticated catheter that uses conductance measurements to track the diameter of the balloon in real-time has been introduced. On the other hand, in-vitro or in-vivo measurements provide compliance assessment. While the former has some significant limitations, not taking into account factors such as the pre-tensional state of the annulus or the dynamic effect of the pulsatile flow, the latter overcome such weaknesses using imaging techniques.
   Among the above-mentioned procedures, intra-balloon pressure measurements have been chosen as a starting point to develop the herein provided experimental approach.

Retrieval of annular geometry

1. The balloon catheter is not only able to detect the dimension of the phantom vessel but it is also sensitive to changes in annular length. On the contrary, as far as shape analysis is concerned, the device is not able to distinguish between elliptical and circular vessels, under the assumption of length variability.

2. The geometry of the balloon for the computational model has been retrieved by tracing contours of the underlying polariscopic image uploaded on Solidworks. The inherent inaccuracy of this procedure could have been caused under- or overestimation of the numerical model, introducing shifts of numerical P-V curves. In fact, by looking at the offset between free inflation curves, it is fair to assume that the model has been slightly underestimated. Surprisingly, the extent of this misleading sizing is very small, being in the order of tenth of mm.

   A mesh convergence test has been done by increasing the mesh density until the results converge satisfactorily. The final discretisation is made of 13824 hexahedral elements: this number allows obtaining an accurate solution with a mesh that is sufficiently dense but not overly demanding of computing resources. In contrast to what has been done for compliant vessels models, 2D triangular cavity elements have not been included in the model of the BAV balloon catheter.

   Although this work admittedly only took into consideration one specific balloon and many other types of balloons are available on the market, the conclusions herein presented, attained on Edwards Ø23 mm, could be extended to Edwards balloons of different sizes, under the assumption that they are made of the same material and produced with the same manufacturing technique.
   If a very accurate model of a different brand is required, details on the material properties and configuration must be collected; however, such differences are likely to be negligible with respect to the overall differences between balloon types.

3. For the sake of simplicity, a linear elastic approximation of the balloon material has been done, whose properties ($E = 600$ N/mm^2; $\nu = 0.45$) have been taken from literature. This simplification is particularly evident in the comparison between experimental and numerical results, mostly affecting curves related to larger

diameters. Despite these approximations, the interaction between balloons and simplified patient-specific models has been validated by obtaining minimal errors. Moreover, the deflation process and the tri-folding configuration used in clinical practice have been included into the numerical model, dramatically improving virtual results. A variable thickness, attributable to parison stretching and manufacturing techniques, has been taken into account, making the model even more accurate.

4. The simulation of balloon inflation has been performed by applying the fluid exchange interaction to the cavity defined in the inner volume of the balloon. In such interaction property, the bulk modulus of the fluid has to be assigned and, in this case, an approximation of water bulk modulus (~ 2.2 GPa) has been chosen. However, since the bulk modulus describes the increases of pressure due to a relative decrease in volume, its approximation might have been affected the value of pressure reached inside the balloon cavity.

5. According to the experimental protocol introduced in Chapter 3, the BAV balloon catheter has been placed on 3D-printed nylon supports; however, it has been chosen to not secure the catheter to the supports with metallic screwed cups, in order to avoid additional constraints. These would have invalidated the overall procedure, bringing additional pressures. Besides, the unavoidable bending of the catheter does not seem to affect experimental measurements: playing with the flexibility of the shaft, different configurations have been tested, resulting in a negligible shift of the P-V curves below the tenth of mL. It must be taken into account, however, that many disturbances are present in clinical applications: therefore, constraining the balloon would have resulted in a greater overlapping of experimental and numerical P-V curves though reducing the reliability of the present approach.

6. As the main limit of every in vitro characterization, the in vivo conditions have been only partially replicated. The action of the tissues surrounding the annulus and the blood circulation have been neglected, as in fact tests have been performed in air.

7. More than 100 experimental tests have been done using the same device: consequently, the material of the balloon catheter could have been permanently damaged. This is particularly evident by looking at the free inflation curves corresponding to tests separated by a distance of months: the hyperelastic behaviour

of the material is in fact much more evident on recent tests rather than on the first ones. Furthermore, according to Eq. 5, the radial stress experienced by the balloon catheter through the experiments is equal to 40.53 MPa, considering a uniform thickness equal to 0.1 mm, a 20 mm non-tensioned diameter and an intra-balloon pressure equal to 4 atm. Since the yield stress of PTFE is equal to 41 MPa, assuming a constant thickness equal to 0.8 mm, there is a good chance the balloon material has been damaged.

8. Rigid vessels have been manufactured by using a CNC (computer numerical control) machine, whose inherent inaccuracy is equal to 0.1/0.2 mm. Being the experimental system so sensitive, an error equal to 0.2 mm would have affected the position of experimental curves. In this case, since all the vessels have been slightly underestimated if compared to the nominal one used in numerical analysis, experimental curves result to be mildly shifted towards the left.

Compliance assessment

9. Knowing cavity pressure and volume variations, distensibility has been numerically computed; these values (0.00124 $mmHg^{-1}$ and 0.00175 $mmHg^{-1}$ for Ø18 mm and Ø19 mm respectively) have been compared to the values extracted through experimental tests, calculated as the local slope of the V-P curves and normalised over the initial volume. As far as Ø18 mm phantom vessel is concerned, the value retrieved from experimental tests corresponds to 0.00121 $mmHg^{-1}$. The error, computed as the difference between the numerically retrieved and the experimental value, is therefore equal to 0.00003 $mmHg^{-1}$. According instead to Ø19 mm vessel, the distensibility is equal to 0.00195 $mmHg^{-1}$. The error, in this case, is 0.0002 $mmHg^{-1}$. Standard deviation of experimental results is always very low, with average values equal to 0.026 $mmHg^{-1}$ and 0.017 $mmHg^{-1}$ respectively, implying both a good reproducibility and repeatability of the measurements.

10. With regard to rapid-prototyped phantoms and researching materials suitable for reproducing the mechanical properties of blood vessels, two different silicone materials have been tested, capable of reproducing simplified (i.e. cylindrical) implantation sites with different stiffness and distensibility characteristics. In this context, Dragon Skin 30 has been considered the best choice, being able to reproduce

the same range of distensibility of human vessels when compared to values from the clinical literature. As expected, the distensibility of the material increases with an increase in wall thickness.

11. As far as the material used to model the vessels is concerned, a 2nd grade Ogden energy function for hyperelastic behaviour has been adopted, representing the function which best-fits the experimental data. However, a proper material evaluation in MSC Marc would have required, in this case, biaxial test data, instead of the uniaxial ones here available. In addition, the Poisson's ratio assumed for the material (ν=0.45) has been taken from literature data.

12. Physiological values of compliance have been retrieved from clinical literature [25] and they have been replicated by varying the thickness of Dragon Skin phantoms. The appropriate thickness has been selected by means of numerical simulations, performed in MSC Marc. Computed radial displacements differ from physiological movements by 0.027 mm at most; this causes an underestimation of soft tissue distensibility, equal to 0.00056 mmHg^{-1} and 0.00005 mmHg^{-1} respectively. However, since the purpose of this procedure is to create rapid-prototyping compliant vessels with a distensibility within the physiological range and not to match the exact value extracted from literature, this underestimation has not been considered a problem for the herein described analysis. As expected, the larger the difference from physiological displacement, the greater the error in terms of distensibility.

13. Linear approximation has been used to compute the annular distensibility, as the local slope of the V-P curve normalised over the initial volume. The steepest the pendency of this line, the smaller the distensibility of the vessel. This curve has been drawn on Matlab defining two points: the first point is where the pressure of the intra-balloon cavity increases by 5 % of the whole pressure elevation. The second point, instead, corresponds to the knee of the curve in the transition between the compliant phase and the hyperelastic one. Surprisingly, despite the approximation made, optimal results have been obtained, showing that the device is very sensitive not only to variations in the annular dimensions but also to minimal changes in its material properties.

14. As claimed by Murphy et al.[25], a perimeter variation of 3.50% has been considered. These authors provide also the mean cross-sectional area and perimeter measurements in systole and diastole with percentage difference across a range of aortic annular calcifications from grade 0 to 3 (respectively 3.43% and 2.48%). Stenotic compliance has not been tested in the present work: however, it's a fair assumption that a stenotic annulus would be stiffer than a healthy one. Consequently, the compliance of this vessel would be bounded between the cases corresponding to rigid vessels and the silicone-based distensibility tested in Chapter 4. This latter case results to be therefore the worst case available and, for this reason, the most challenging one.

15. All models are based on the aortic annulus being simulated by a cylindrical contact surface, which is not representative of the anatomy into which TAVR devices are implanted. In reality, this varies from patient to patient and irregularities in the annulus geometry, which is often described as roughly elliptical, are mostly common. For this purpose, even elliptical phantoms have been tested and it has been demonstrated that it might be very difficult, or even impossible, to univocally associate a curve to a combination of diameter, length and ellipticity using a commercially available balloon catheter.

Curves analysis: automatic algorithm to retrieve annulus dimension

16. In the last section of Chapter 4, an analytical algorithm to automatically retrieve the dimension of the annulus from P-V curves based on fitting P-V data with the parametric integral of the logistic function has been introduced. Undoubtedly, it would have been much easier to simply mapping the correlation between the diameter and the injected volume corresponding to the sudden increase of pressure. On the contrary, a more complex algorithm that exploits the parametric integral of the logistic function has been used. The major benefit of this approach is that a fitting on the overall curve, instead of focusing only on the knee of the function, would provide additional parameters to evaluate also the influence of length, distensibility and ellipticity changes.

17. The integral of the sigmoid function provides an impressive approximation of both experimental and numerical P-V curves associated with a diameter lower than the

non-tensioned diameter of the balloon (20 mm). The obtained errors are in fact extremely low, indicating a remarkable data fitting. Nevertheless, further and alternative approximations have been investigated, providing however less satisfying results. The coefficient "c" shows in fact a direct correlation with the diameter and it could be used as a feature F1 to assess the size in the case of fixed annular length.
Instead, when the vessel is greater than the non-tensioned diameter of the balloon, the dimension of the annulus can be retrieved by looking at one of the two coordinates of the inflection point. This last case seems to be more favourable to the retrieval of vessel dimensions: the inflection point is an invariant measure of annulus geometry, being not dependent on the length of the vessel.
However, how to determine whether gathered data belong to the first or to the second section is still subject of analysis.

5.3 Suggestions for future work

It is evident that there are also some limitations, which serve to provide a basis for future work. These include:

1. As far as the model itself is concerned, further refinements might improve the overall reliability of the method. A more complete characterization of the balloon material, by means of tensile tests, should be carried out as a first step, in order to assess its constitutive law, which is expected to be hyperelastic. Consequently, the validation of the interaction between balloons and simplified anatomies should be extended, by including a nonlinear behaviour of the balloon material as well. Furthermore, biaxial tensile tests should be performed on silicone materials likewise, allowing a proper and better material evaluation in MSC Marc. This point is particularly important since materials nonlinearities are at the basis of every biological tissue, thus expected also for the aortic annulus, especially when it substantially deforms during overloading conditions.

2. In addition, the anisotropy of the different layers constituting the arterial wall, as well as the real properties of the calcium deposited on the AV leaflets, might be interesting parameters to replicate. In this case, vessel walls and stenosis should be modeled using different materials, since in reality the mechanical properties of the calcium residuals are significantly different from the ones of the tissue where they are deposited.

3. Moreover, the presence of the circulatory system and the blood flow might be included both experimentally, by means of pulsatile mock loops, and computationally.

4. Further simulations could be performed taking into account the inaccuracy of CNC (computer numerical control)-based annuli, in order to perfectly match the results concerning both numerical and experimental analysis. Moreover, simulations could be performed by applying an external pressure to the phantom vessels. This pressure, roughly equal to 50 mmHg in order to simulate the rapid pacing induced in clinical practice, is not expected to substantially vary the obtained results.

5. The definition of cavity surface elements inside the balloon could refine by 0.1 mL the computed volume of the balloon, shifting the associated curves towards the right. This shift, albeit very small, could be visibly appreciated on the graphs, being the system sensitive to variations equal to one-tenth of mL.

6. The automatic algorithm provided at the end of Chapter 4 has been implemented considering only annular dimensions changes, neglecting annular length, soft tissue compliance and shape variability. What other feature of the function could possibly provide a direct correlation with the length must be still verified. A possible useful feature F2 could be the slope of the upper linear part of the curve; as seen in the discussion of the previously obtained results, in fact, a shorter annulus results to slightly reduce the slope of all the P-V curves during the pressurisation phase. This parameter could be estimated either by fitting data with the integral of the sigmoid or even by considering an averaged slope of the tangent of the linear-looking part of the knee.

Furthermore, a reliable criterion to assess whether gathered data belong to the first section (diameters lower than the non-tensioned diameter of the balloon) or to the second one (diameters > 20 mm) must be defined. In this regard, goodness-of-fit statistics (SSE, R^2 or RMSE) could be used: numerical (or experimental) results are fitted with the logistic function and the fitting error is computed. If this error is greater than a predetermined threshold, the P-V curve belongs to the second section; if the error is instead lower than this threshold, the fitting of the sigmoid function is good and therefore the P-V curve can be considered within the first region of analysis.

7. In addition, in order to make such a process applicable in every kind of clinical conditions, a model for each brand and size of the balloon should be created and validated, although the modeling workflow is not expected to substantially vary.

8. In conclusion, moving towards the clinical application, the next step of this work is represented by the validation of the approach with ex vivo animal specimen, eventually followed by in vivo trials. Furthermore, in order for the method to be applied to a wider range of anatomies and diseases, more patient-specific morphologies should be analysed.

APPENDIX A

CAD DESIGN: GEOMETRY OF THE BALLOON CATHETER PLATFORM AND PHANTOM MODELS OF THE VESSEL

For the sake of completeness, this is a collection of technical drawings and pictures pertaining to the construction of the balloon holders and platform used during experimental tests. Moreover, drawings of CAD moulds for silicone are shown.

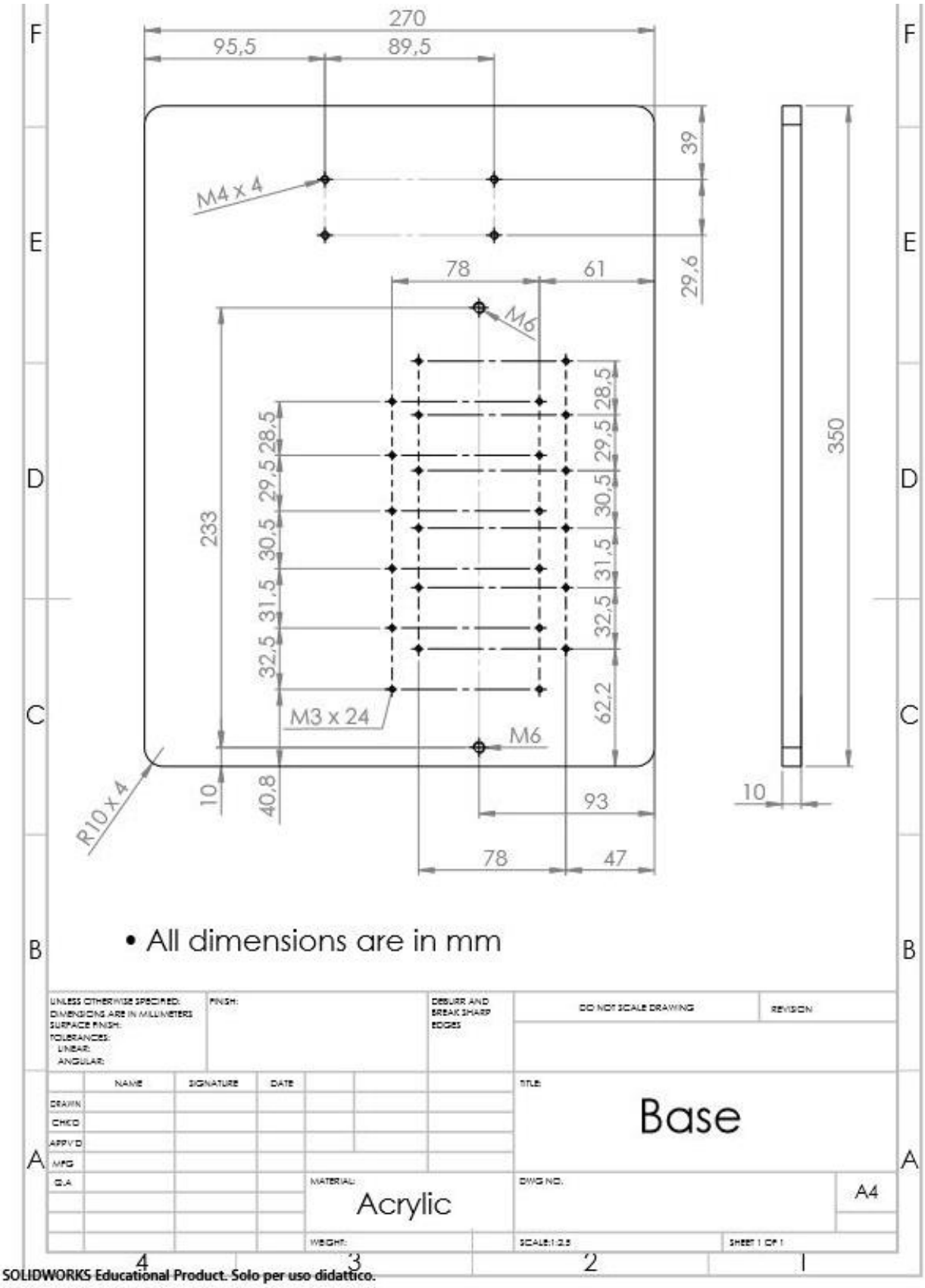
270
95,5
89,5
39
M4 x 4
78
61
29,6
M6
28,5
29,5
30,5
31,5
32,5
233
M3 x 24
62,2
M6
R10 x 4
10
40,8
93
78
47
350
10
• All dimensions are in mm
UNLESS OTHERWISE SPECIFIED:
DIMENSIONS ARE IN MILLIMETERS
SURFACE FINISH:
TOLERANCES:
LINEAR:
ANGULAR:
FINISH:
DEBURR AND BREAK SHARP EDGES
DO NOT SCALE DRAWING
REVISION
NAME
SIGNATURE
DATE
DRAWN
CHK'D
APP'V'D
MFG
Q.A
TITLE:
Base
MATERIAL:
Acrylic
DWG NO.
A4
WEIGHT:
SCALE:1:2.5
SHEET 1 OF 1
SOLIDWORKS Educational Product. Solo per uso didattico.

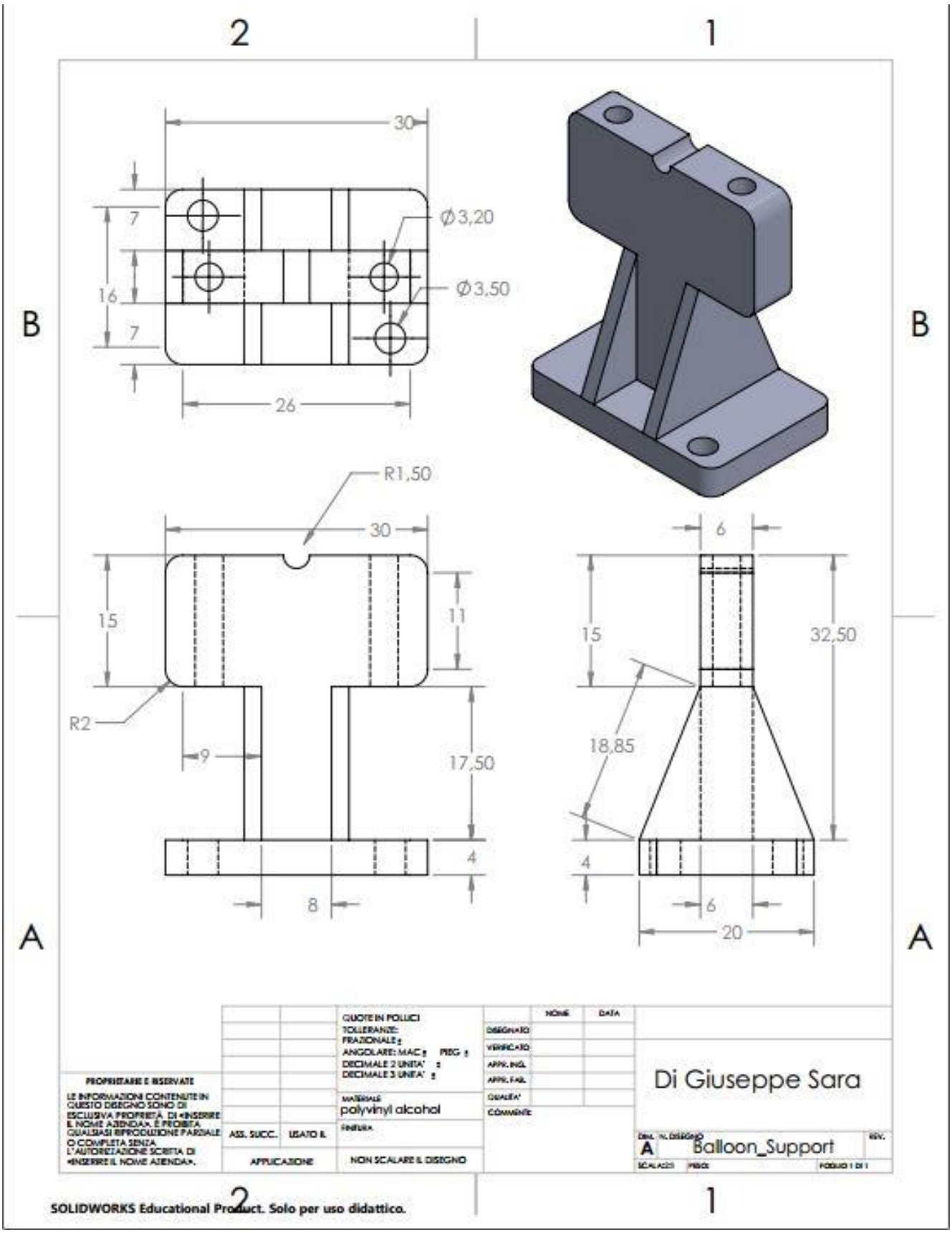
2
1
B
A
30
7
16
7
26
Ø3,20
Ø3,50
R1,50
30
15
11
R2
9
17,50
4
8
6
15
32,50
18,85
4
6
20
GIUOTE IN POLLICI
TOLLERANZE:
FRAZIONALE ±
ANGOLARE: MAC ± PREC ±
DECIMALE 2 UNITA' ±
DECIMALE 3 UNITA' ±
MATERIALE
polyvinyl alcohol
FINITURA
NON SCALARE IL DISEGNO
NOME
DATA
DISEGNATO
VERIFICATO
APPR. ING.
APPR. FAB.
QUALITA'
COMMENTI
Di Giuseppe Sara
DIM. N. DISEGNO
A
Balloon_Support
REV.
SCALA:1:1
PESO:
FOGLIO 1 DI 1
PROPRIETARIE E RISERVATE
LE INFORMAZIONI CONTENUTE IN QUESTO DISEGNO SONO DI ESCLUSIVA PROPRIETÀ DI «INSERIRE IL NOME AZIENDA». È PROIBITA QUALSIASI RIPRODUZIONE PARZIALE O COMPLETA SENZA L'AUTORIZZAZIONE SCRITTA DI «INSERIRE IL NOME AZIENDA».
ASS. SUCC.
USATO IL
APPLICAZIONE
SOLIDWORKS Educational Product. Solo per uso didattico.

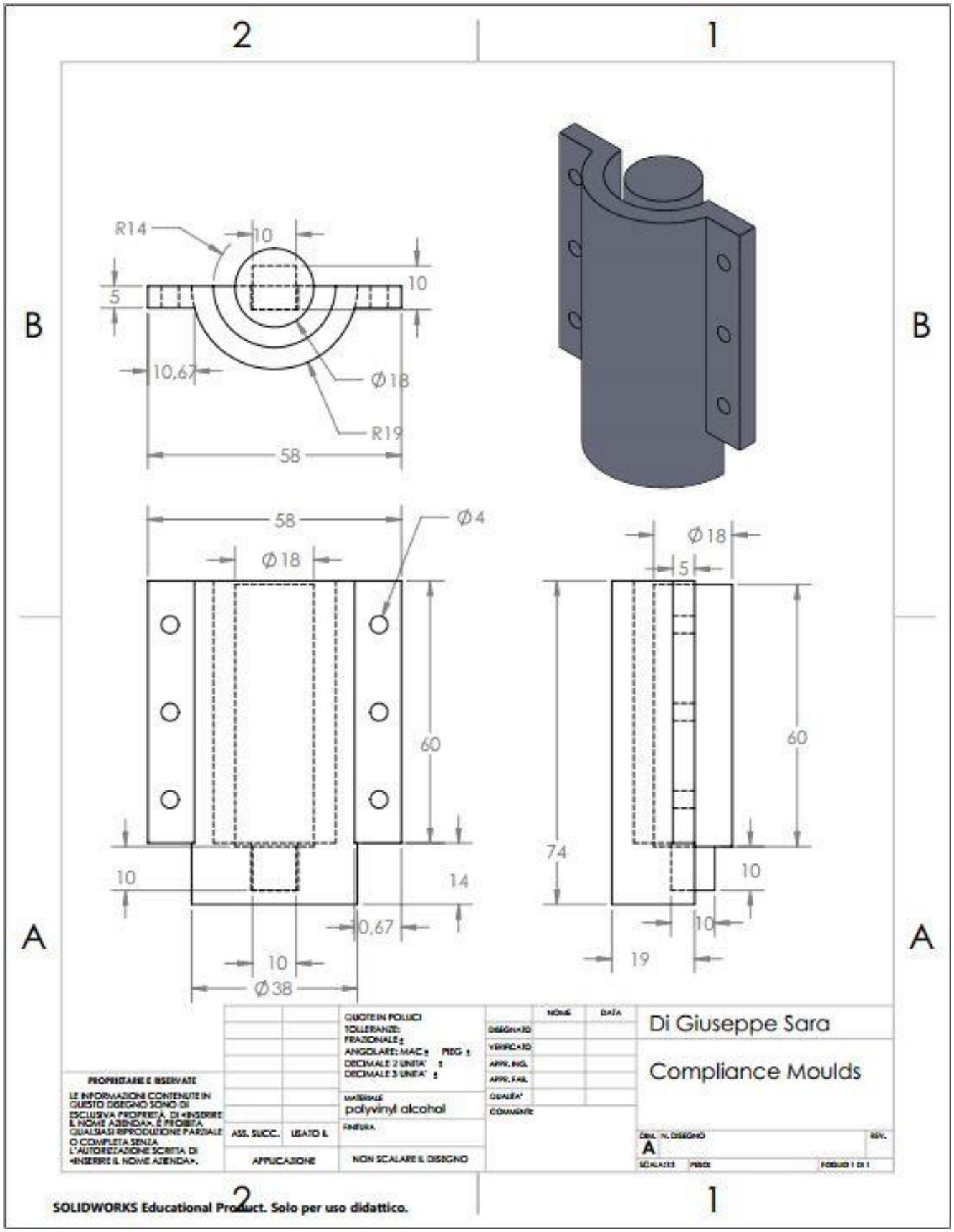
2
1
B
A
R14
10
5
10
10,67
Ø18
R19
58
Ø4
Ø18
60
10
14
10,67
10
Ø38
Ø18
5
60
74
10
10
19
SOLIDWORKS Educational Product. Solo per uso didattico.
PROPRIETARIE E RISERVATE
LE INFORMAZIONI CONTENUTE IN QUESTO DISEGNO SONO DI ESCLUSIVA PROPRIETÀ DI «INSERIRE IL NOME AZIENDA». È PROIBITA QUALSIASI RIPRODUZIONE PARZIALE O COMPLETA SENZA L'AUTORIZZAZIONE SCRITTA DI «INSERIRE IL NOME AZIENDA».
ASS. SUCC.
USATO IL
APPLICAZIONE
QUOTE IN POLLICI
TOLLERANZE:
FRAZIONALE ±
ANGOLARE: MAC ± PREC ±
DECIMALE 2 UNITA' ±
DECIMALE 3 UNITA' ±
MATERIALE
polyvinyl alcohol
FINITURA
NON SCALARE IL DISEGNO
NOME
DATA
DISEGNATO
VERIFICATO
APPR. ING.
APPR. FAB.
QUALITÀ'
COMMENTI
Di Giuseppe Sara
Compliance Moulds
DIM. N. DISEGNO
A
REV.
SCALA:1:1
PESO:
FOGLIO 1 DI 1

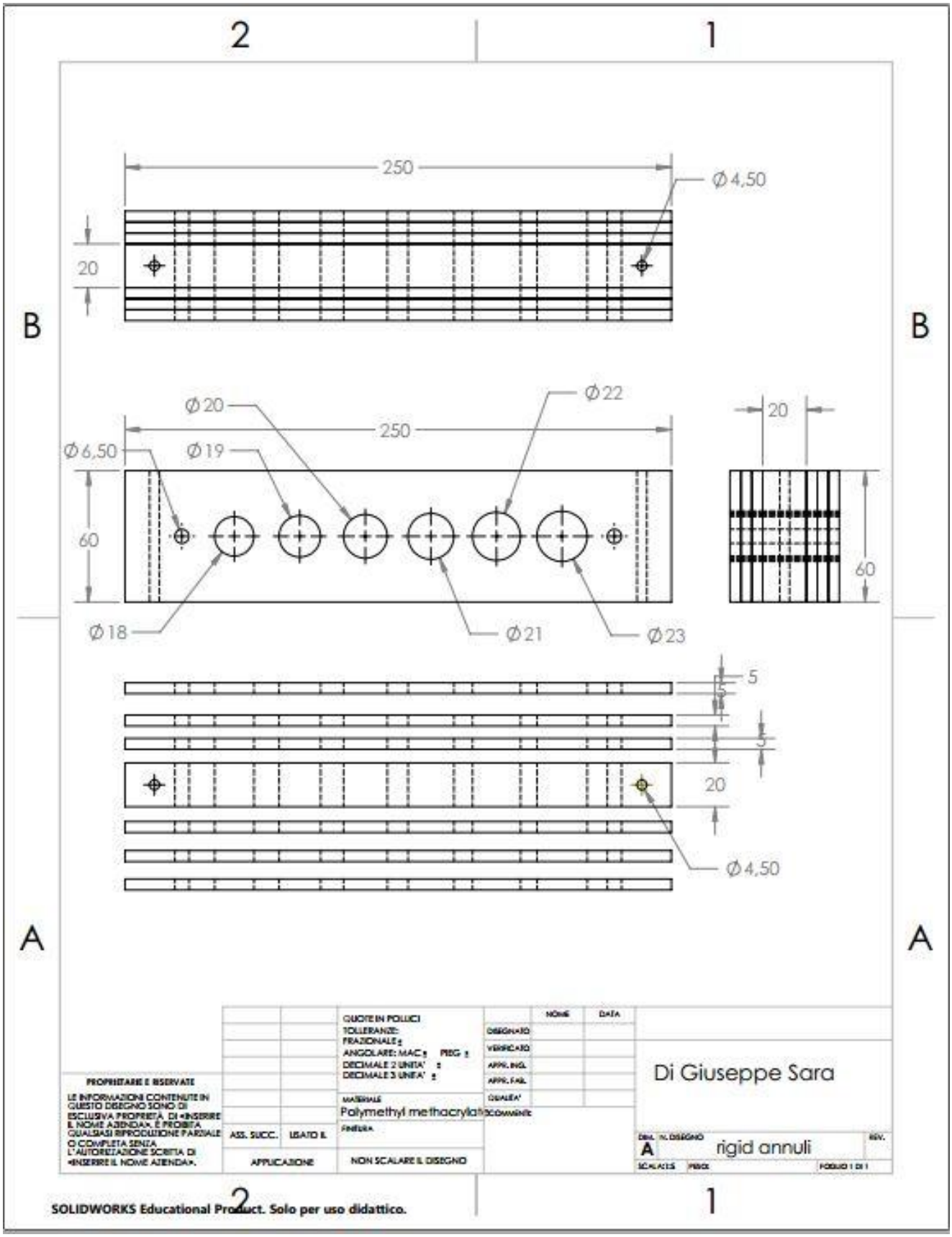
2
1
B
B
250
Ø4,50
20
Ø20
Ø22
250
20
Ø6,50
Ø19
60
60
Ø18
Ø21
Ø23
5
5
20
Ø4,50
A
A
QUOTE IN POLLICI
TOLLERANZE:
FRAZIONALE ±
ANGOLARE: MAC ± PIEG ±
DECIMALE 2 UNITA' ±
DECIMALE 3 UNITA' ±
MATERIALE
Polymethyl methacrylate
FINITURA
NOME
DATA
DISEGNATO
VERIFICATO
APPR. ING.
APPR. FAB.
QUALITA'
COMMENTI
PROPRIETARIE E RISERVATE
LE INFORMAZIONI CONTENUTE IN QUESTO DISEGNO SONO DI ESCLUSIVA PROPRIETÀ DI «INSERIRE IL NOME AZIENDA». È PROIBITA QUALSIASI RIPRODUZIONE PARZIALE O COMPLETA SENZA L'AUTORIZZAZIONE SCRITTA DI «INSERIRE IL NOME AZIENDA».
ASS. SUCC.
USATO IL
APPLICAZIONE
NON SCALARE IL DISEGNO
Di Giuseppe Sara
DIM. N. DISEGNO
A
rigid annuli
REV.
SCALA:1:5
PESO:
FOGLIO 1 DI 1
SOLIDWORKS Educational Product. Solo per uso didattico.
2
1

BIBLIOGRAPHY

[1] S. Mendis, P. Puska, and B. Norrving, "Global Atlas on cardiovascular disease prevention and control," *World Heal. Organ.*, p. 164, 2011.

[2] A. A. Klein, N. J. Skubas, and J. Ender, "Controversies and complications in the perioperative management of transcatheter aortic valve replacement," *Anesth. Analg.*, vol. 119, no. 4, pp. 784–798, 2014.

[3] P. Généreux *et al.*, "Bleeding complications after surgical aortic valve replacement compared with transcatheter aortic valve replacement: Insights from the PARTNER i trial (Placement of Aortic Transcatheter Valve)," *J. Am. Coll. Cardiol.*, vol. 63, no. 11, pp. 1100–1109, 2014.

[4] H. Mollmann, W.-K. Kim, J. Kempfert, T. Walther, and C. Hamm, "Complications of transcatheter aortic valve implantation (TAVI): how to avoid and treat them," *Heart*, vol. 101, no. 11, pp. 900–908, 2015.

[5] M. J. Czarny and J. R. Resar, "Diagnosis and management of valvular aortic stenosis," *Clin. Med. Insights Cardiol.*, vol. 8, pp. 15–24, 2014.

[6] S. K. Kodali *et al.*, "Two-Year Outcomes after Transcatheter or Surgical Aortic-Valve Replacement," *N. Engl. J. Med.*, vol. 366, no. 18, pp. 1686–1695, 2012.

[7] A. G. Cerillo, M. Mariani, S. Berti, and M. Glauber, "Sizing the aortic annulus.," *Ann. Cardiothorac. Surg.*, vol. 1, no. 2, pp. 245–56, 2012.

[8] C. Bleakley, M. Eskandari, and M. Monaghan, "3D transoesophageal echocardiography in the TAVI sizing arena: should we do it and how do we do it?," *Echo Res. Pract.*, vol. 4, no. 1, pp. R21–R32, 2017.

[9] N. Piazza, P. de Jaegere, C. Schultz, A. E. Becker, P. W. Serruys, and R. H. Anderson, "Anatomy of the aortic valvar complex and its implications for transcatheter implantation of the aortic valve.," *Circ. Cardiovasc. Interv.*, vol. 1, no. 1, pp. 74–81, 2008.

[10] R. H. Anderson, “Clinical anatomy of the aortic root.,” *Heart*, vol. 84, no. 6, pp. 670–673, 2000.

[11] A. Hager *et al.*, “Diameters of the thoracic aorta throughout life as measured with helical computed tomography,” *J. Thorac. Cardiovasc. Surg.*, vol. 123, no. 6, pp. 1060–1066, 2002.

[12] S. . Hadinegoro *et al.*, “New England Journal,” *N. Engl. J. Med.*, vol. 373, no. 13, pp. 1195–1206, 2015.

[13] P. A. Pellikka, R. A. Nishimura, K. R. Bailey, and A. J. Tajik, “The natural history of adults with asymptomatic, hemodynamically significant aortic stenosis,” *J. Am. Coll. Cardiol.*, vol. 15, no. 5, pp. 1012–1017, 1990.

[14] J. B. Barlow and D. Jankelow, “Prospective study of asymptomatic aortic stenosis,” *Circulation*, vol. 97, no. 16, pp. 1651–1653, 1998.

[15] M. J. Reardon *et al.*, “Surgical or Transcatheter Aortic-Valve Replacement in Intermediate-Risk Patients,” *N. Engl. J. Med.*, vol. 376, no. 14, pp. 1321–1331, 2017.

[16] R. R. Makkar *et al.*, “Transcatheter Aortic-Valve Replacement for Inoperable Severe Aortic Stenosis,” *N. Engl. J. Med.*, vol. 366, no. 18, pp. 1696–1704, 2012.

[17] I. M. Panayiotides and E. Nikolaides, “Transcatheter aortic valve implantation (TAVI): Is it time for this intervention to be applied in a lower risk population?,” *Clin. Med. Insights Cardiol.*, vol. 8, pp. 93–102, 2014.

[18] S. Tzamtzis, J. Viquerat, J. Yap, M. J. Mullen, and G. Burriesci, “Numerical analysis of the radial force produced by the Medtronic-CoreValve and Edwards-SAPIEN after transcatheter aortic valve implantation (TAVI),” *Med. Eng. Phys.*, vol. 35, no. 1, pp. 125–130, 2013.

[19] U. K. Allahwala *et al.*, “Transcatheter aortic valve implantation: current trends and future directions,” *Future Cardiol.*, vol. 12, no. 1, pp. 69–85, 2016.

[20] M. Abdel-Wahab *et al.*, “Comparison of Balloon-Expandable vs Self-expandable Valves in Patients Undergoing Transcatheter Aortic Valve Replacement,” *Jama*, vol. 311, no. 15, p. 1503, 2014.

[21] J. Webb and A. Cribier, “Percutaneous transarterial aortic valve implantation: What do we know?,” *Eur. Heart J.*, vol. 32, no. 2, pp. 140–147, 2011.

[22] C. W. Hamm, M. Arsalan, and M. J. Mack, “The future of transcatheter aortic valve implantation,” *Eur. Heart J.*, vol. 37, no. 10, pp. 803–810, 2016.

[23] C. W. Hamm *et al.*, “The German Aortic Valve Registry (GARY): In-hospital outcome,” *Eur. Heart J.*, vol. 35, no. 24, pp. 1588–1598, 2014.

[24] K. Gebauer *et al.*, “The Risk of Acute Kidney Injury and Its Impact on 30-Day and Long-Term Mortality after Transcatheter Aortic Valve Implantation,” *Int. J. Nephrol.*, vol. 2012, pp. 1–8, 2012.

[25] D. T. Murphy *et al.*, “Dynamism of the aortic annulus: Effect of diastolic versus systolic CT annular measurements on device selection in transcatheter aortic valve replacement (TAVR),” *J. Cardiovasc. Comput. Tomogr.*, vol. 10, no. 1, pp. 37–43, 2016.

[26] A. M. Kasel *et al.*, “Standardized imaging for aortic annular sizing: Implications for transcatheter valve selection,” *JACC Cardiovasc. Imaging*, vol. 6, no. 2, pp. 249–262, 2013.

[27] A. C. Pouleur, J. B. L. P. De Waroux, A. Pasquet, D. Vancraeynest, J. L. J. Vanoverschelde, and B. L. Gerber, “Planimetric and continuity equation assessment of aortic valve area: Head to head comparison between cardiac magnetic resonance and echocardiography,” *J. Magn. Reson. Imaging*, vol. 26, no. 6, pp. 1436–1443, 2007.

[28] H. Baumgartner *et al.*, “Echocardiographic Assessment of Valve Stenosis: EAE/ASE Recommendations for Clinical Practice,” *J. Am. Soc. Echocardiogr.*, vol. 22, no. 1, pp. 1–23, 2009.

[29] J. L. Zamorano *et al.*, “EAE/ASE recommendations for the use of echocardiography in new transcatheter interventions for valvular heart disease,” *Eur. Heart J.*, vol. 32, no. 17, pp. 2189–2214, 2011.

[30] J. D. Holmes, D.R., Mack, M.J., Kaul, S., Agnihotri, A., Alexander, K.P., Bailey, S.R....Thomas, “2012 ACCF/AATS/SCAI/ STS Expert consensus document on transcatheter aortic valve replacement,” *J. Thorac. Cardiovasc. Surg.*, vol. 144, no. 3, pp. e29–e84, 2012.

[31] D. Messika-Zeitoun *et al.*, “Multimodal Assessment of the Aortic Annulus Diameter. Implications for Transcatheter Aortic Valve Implantation,” *J. Am. Coll. Cardiol.*, vol. 55, no. 3, pp. 186–194, 2010.

[32] M. C. Svendsen *et al.*, “Two-in-one aortic valve sizing and valvuloplasty conductance balloon catheter,” *Catheter. Cardiovasc. Interv.*, vol. 86, no. 1, pp. 136–143, 2015.

[33] J. Kempfert *et al.*, “Aortic annulus sizing: Echocardiographic versus computed tomography derived measurements in comparison with direct surgical sizing,” *Eur. J. Cardio-thoracic Surg.*, vol. 42, no. 4, pp. 627–633, 2012.

[34] L. A. Freeman, P. M. Young, T. A. Foley, E. E. Williamson, C. J. Bruce, and K. L. Greason, “CT and MRI assessment of the aortic root and ascending aorta,” *Am. J. Roentgenol.*, vol. 200, no. 6, 2013.

[35] J. Leipsic *et al.*, “Multidetector computed tomography in transcatheter aortic valve implantation,” *JACC Cardiovasc. Imaging*, vol. 4, no. 4, pp. 416–429, 2011.

[36] K. Otani *et al.*, “Assessment of the aortic root using real-time 3D transesophageal echocardiography.,” *Circ. J.*, vol. 74, no. 12, pp. 2649–2657, 2010.

[37] P. Marcos-Alberca *et al.*, “Intraoperative monitoring with transesophageal real-time three-dimensional echocardiography during transapical prosthetic aortic valve implantation,” *Rev. Española Cardiol.*, vol. 63, no. 3, pp. 352–356, 2010.

[38] O. Husser *et al.*, “Impact of three-dimensional transesophageal echocardiography on prosthesis sizing for transcatheter aortic valve implantation,” *Catheter. Cardiovasc. Interv.*, vol. 80, no. 6, pp. 956–963, 2012.

[39] V. C. Babaliaros *et al.*, “Use of Balloon Aortic Valvuloplasty to Size the Aortic Annulus Before Implantation of a Balloon-Expandable Transcatheter Heart Valve,” *JACC Cardiovasc. Interv.*, vol. 3, no. 1, pp. 114–118, 2010.

[40] J. O’Dea and D. J. Nolan, “Assessment of annular distensibility in the aortic valve,” *Interact. Cardiovasc. Thorac. Surg.*, vol. 15, no. 3, pp. 361–363, 2012.

[41] J. A. Funder *et al.*, “Aortic root distensibility and cross-sectional areas in stented and subcoronary stentless bioprostheses in pigs.,” *Interact. Cardiovasc. Thorac. Surg.*, vol. 10, no. 6, pp. 976–980, 2010.

[42] A. Hamdan *et al.*, “Deformation dynamics and mechanical properties of the aortic annulus by 4-dimensional computed tomography: Insights into the functional anatomy of the aortic valve complex and implications for transcatheter aortic valve therapy,” *J. Am. Coll. Cardiol.*, vol. 59, no. 2, pp. 119–127, 2012.

[43] C. E. Ruiz, “Optimizing transcatheter aortic valve sizing and minimizing vascular complications,” *J. Am. Coll. Cardiol.*, vol. 59, no. 2, pp. 128–129, 2012.

[44] L. M. De Heer *et al.*, “Pulsatile distention of the nondiseased and stenotic aortic valve annulus: Analysis with electrocardiogram-gated computed tomography,” *Ann.*

Thorac. Surg., vol. 93, no. 2, pp. 516–522, 2012.

[45] M. S. Schlicht, K. Khanafer, A. Duprey, P. Cronin, and R. Berguer, "Experimental foundation for in vivo measurement of the elasticity of the aorta in computed tomography angiography," *Eur. J. Vasc. Endovasc. Surg.*, vol. 46, no. 4, pp. 447–452, 2013.

[46] T. R. Keeble, A. Khokhar, M. M. Akhtar, A. Mathur, R. Weerackody, and S. Kennon, "Percutaneous balloon aortic valvuloplasty in the era of transcatheter aortic valve implantation: a narrative review," *Open Hear.*, vol. 3, no. 2, p. e000421, 2016.

[47] I. Inglessis and M. J. Landzberg, "Interventional catheterization in adult congenital heart disease," *Circulation*, vol. 115, no. 12, pp. 1622–1633, 2007.

[48] A. Cribier, "Development of transcatheter aortic valve implantation (TAVI): A 20-year odyssey," *Arch. Cardiovasc. Dis.*, vol. 105, no. 3, pp. 146–152, 2012.

[49] I. Ben-Dor *et al.*, "Complications and outcome of balloon aortic valvuloplasty in high-risk or inoperable patients," *JACC Cardiovasc. Interv.*, vol. 3, no. 11, pp. 1150–1156, 2010.

[50] W. Wrap-up and E. Mabry, "Molding Processes Get a Two-Shot Extruded Tubing Designed for Balloon Production," no. September, 2008.

[51] S. E. Benzley, E. Perry, K. Merkley, B. Clark, and G. Sjaardema, "A Comparison of All-Hexahedral and All-Tetrahedral Finite Element Meshes for Elastic and Elasto-Plastic Analysis," *4th Int. Meshing Roundtable, Sandia Natl. Lab.*, pp. 179–191, 1995.

[52] P. Blanke *et al.*, "Conformational pulsatile changes of the aortic annulus: Impact on prosthesis sizing by computed tomography for transcatheter aortic valve replacement," *JACC Cardiovasc. Interv.*, vol. 5, no. 9, pp. 984–994, 2012.

[53] A. Papachristidis *et al.*, "Three-Dimensional Measurement of Aortic Annulus Dimensions Using Area or Circumference for Transcatheter Aortic Valve Replacement Valve Sizing: Does It Make a Difference?," *J. Am. Soc. Echocardiogr.*, vol. 30, no. 9, pp. 871–878, 2017.

[54] MSC, "Experimental Elastomer Analysis," *Msc*, p. 308, 2010.

[55] Y. Maeno *et al.*, "Transcatheter Aortic Valve Replacement With Different Valve Types in Elliptic Aortic Annuli," *Circ. J.*, vol. 81, no. 7, pp. 1036–1042, 2017.